Epitaxial chalcogenide Ge-Sb-Te thin films and superlattices by pulsed laser deposition

Der Fakultät für Physik und Geowissenschaften
der Universität Leipzig

eingereichte
DISSERTATION
zur Erlangung des akademischen Grades

Doctor Rerum Naturalium
Dr. rer. rat.

vorgelegt
von Isom Hilmi
geboren am 02.08.1985 in Jepara, Indonesien
Leipzig, den 03.07.2018

Gutachter: Prof. Dr. Dr. h.c. Bernd Rauschenbach
Prof. Dr. Robert E. Simpson

Tag der Verleihung: 17.12.2018

Bibliographische Beschreibung

Review:

This thesis deals with the deposition of epitaxial chalcogenide ($Ge_2Sb_2Te_5$ (GST225), GeTe and Sb_2Te_3) thin films and superlattice (SL) arrangement based on GeTe-Sb_2Te_3 using pulsed laser deposition (PLD) technique on (111)-oriented Si substrates. The thin films are characterized using *in-situ* RHEED, XRD, SEM, AFM and TEM.

The epitaxial trigonal GST225 films with *out-of-plane* c-plane orientation were grown in 2D growth mode. For the first group of the films (substrate-target distance (d_{ts}) of ~7.5 cm), the epitaxial window was observed from 200 °C to 300 °C. By varying laser frequency, deposition rate as high as 42 nm/ min can be achieved. The deposition with a slight reduction of d_{ts} to ~6 cm (second group) at moderate T_s of 220 °C results in the epitaxial films with heterogeneous vacancy structures (coexisting metastable phases. i.e. with random and ordered vacancies, and stable trigonal phase). Thermal annealing (at 220 °C) leads to a phase transformation towards a pure trigonal phase.

The epitaxial Sb_2Te_3 films with out-of-plane (0001) oriented trigonal structure were grown at T_s from 140 to 280 °C in 2D growth mode. The optimum T_s in terms of deposition rate and film quality was determined to be 240 °C. The epitaxial growth of Sb_2Te_3 thin films is initiated by the self-organized formation of a Sb/Te single-atomic passivation layer on the Si surface.

The growth of GeTe was initialized by the formation of an ultra-thin amorphous layer. The films were predominantly grown in the mix of 2D and 3D growth modes. The deposited films possesses trigonal structure *out-of-plane* (0001)-orientated on Si(111). By employing a 2D-bonded Sb_2Te_3 as a seeding layer on Si(111), the epitaxial window of GeTe can be extended especially towards the lower temperature regime, up to 145 °C. Additionally, the surface topography can be significantly improved, indicating that the films are grown in 2D growth mode on the buffered substrate.

The epitaxial SLs can be grown starting at T_s = 140 °C. Each layer of the SLs, i.e. Sb_2Te_3 and GeTe layer, was grown in 2D growth mode. An intermixing of GeTe and Sb_2Te_3 layers occurred at a higher temperature deposition. Studies on local structure of 140 °C-deposited SL showed that the SL consists of Ge-rich $Ge_{(x+y)}Sb_{(2-y)}Te_z$ and Sb_2Te_3 units intercalated by Van der Waals gaps with the inhomogeneity of layer thickness across the SL.

The obtained results demonstrate the feasibility of PLD for deposition of good quality epitaxial chalcogenide thin films and SL structure on Si(111).

Table of Contents

Chapter I
Introduction

1.1. Preface

The ongoing advancement in Internet and multimedia applications has pervaded our lifestyles and become one of the important factors for a further progress in today's fast and mobile society. The development mutually leads to continuously increasing demands for better-performing electronics, specifically ones which are mobile and compact. It inseparably also implies on the need for a more superior data storage or memory device as an inextricable part. A highly-performing mobile electronics requires a superior data storage and computation units, e.g. greater in capacities, faster in programming speeds, efficient in energy consumption, but still low in price.

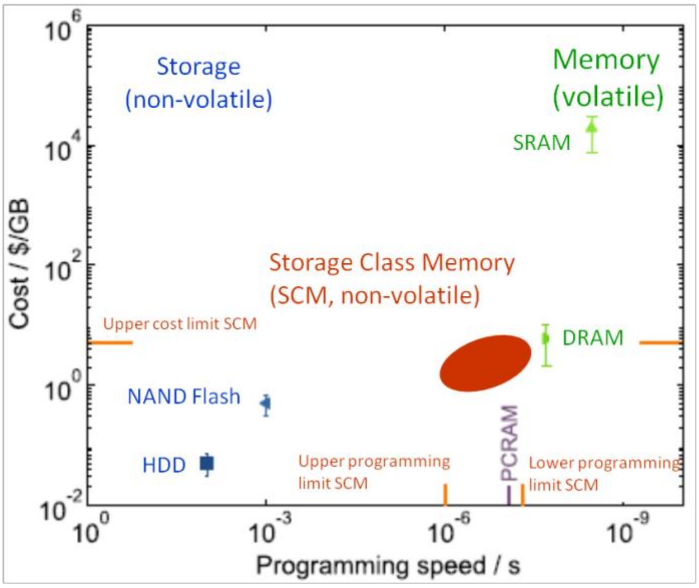

Fig.1.1. The map of the data storage and memory platforms showing the strategic location of the emerging Storage Class Memory (SCM). The SCM is aiming at bridging the cost/performances gap between non-volatile Flash or HDD and volatile DRAM/SRAM. Adapted from [7].

Today, however, the common data storage and memory technologies are facing real struggles for the further developments, i.e., to maintain the steady improvement, more specifically in terms of data processing speed and storage capacity. The Moore's law more or less stating the doubling of the number of transistors per chip on an silicon-based integrated circuits in roughly every 18 months [3, 4], which successfully persists during the last decades is started being questioned for its continuous realization in the near future, as was presented in the International Technology Roadmap for Semiconductor [4, 5]. Another arising issue is in terms of further enhancement in computer's performances, e.g. to cope with the von-Neumann bottleneck, a limitation in computer's speed due to a latent problem in data flow between its processor and memory [6].

To be more concise, a summary of today's memory features is presented in Fig.1, showing a map of some established data storage and memory platforms drawn by comparing their performance (programming speed) and cost per capacity-unit (GB) [7]. Special attentions are put on silicon-transistor-based platforms which are omnipresent in today's computer: e.g. a dynamic random access memory (DRAM) and Flash memory [8]. The working principle of both memory classes are in general based on deploying electric charges for processing and storing data in the form of binary number ("0" and "1").

Flash memory is presently the most appreciated data storage platform. Flash memory cell is basically constructed out of a MOSFET with a floating gate (FG) integrated between its control gate and its channel. The FG is isolated all around typically by oxide layers, so that electric charges can be stored within it, rendering it non-volatile. The non-volatility refers to the ability to retain data even when all the powers connected to it are turned-off. It can be divided into two variants: NOR and NAND wherein the cells are arranged in parallel and in series, respectively. However, a Flash memory has some potential drawbacks. First, it is comparably very slow in programming speed, in milliseconds regime [9] (see Fig. 1). Also of concern is its further scalability. In general, the rate of miniaturization in transistor-silicon-based technology is related to Dennard scaling rule. Presently, in the microelectronic industry the 14 nm node technology is achieved. In the case of Flash memory, further scaling down in size implies specifically on the thinning of this oxide layer which would lead to inevitable problems such as a higher possibility for occurring of leakage current since the electrons must be stored in a shrinking cell [10]. Hence, it faces a problem in further miniaturization. Additionally, this type of memory is prone to suffer from failure due to excessive data-writing/erasing cycles which could deteriorate the oxide layer [11, 12]. The fact that the relatively high bias voltage is needed in order to flow electric currents into FG, e.g. when reading or writing data process takes place, makes Flash is less energy-efficient.

On the other side, DRAM is the common platform for temporary data for computational task. A DRAM cell commonly consists out of a transistor and a capacitor to control the electric current and store the charge, respectively. DRAM is way faster in programming speed than Flash memory (see Fig. 1). However, in its operational mode cyclic charge refreshments are necessary within DRAM cell [13] render DRAM volatile, i.e. the power must be continuously connected to preserve the data. It implies on energy intensive *per se*. This cyclic charge refreshment is overcome by static random access memory (SRAM) cell design a flip-flop mechanism is implemented using four (or six) transistors in a cell instead of transistor-and-capacitor-based design as implemented in DRAM. This makes that SRAM is even faster and usually applied as cache memory (see Fig. 1). However, the fact that it is complex in cell architecture requires relatively bigger geometrical space hence makes it expensive. Another physical phenomenon is demonstrated in e.g. a magnetic storage media, e.g. hard-disk drive (HDD) [11], utilizing magnetic dipoles switching of materials. This type of storage shares the same problems in terms of slow programming speed and scalability [10]. Hence, HDD cannot also serve as a principal memory, see Fig. 1.

Some principles based on different physical phenomena are sought in order to invent a new platform to replace and/or outperform the present memory device's performance, in particular to bridge the gap between Flash and DRAM. Special examples are given in ferroelectric RAM (FRAM) [14], magneto-resistive RAM (MRAM) [15], resistive oxide memory (RRAM) [16] and phase change RAM (PCRAM) [17]. The technologies have vouched its applicability as a memory device owing to their impressive features such as fast programming speeds, energy consumptions and cyclability, with also of course their persisting downsides, such as the miniaturization issue on FRAM and MRAM [6] as well as an issue on device controllability in RRAM [18]. Other working principles are found in emerging concepts such as quantum memory [19], carbon nanotube RAM [20] and spin-torque transfer RAM [21] —all of which are struggling with the lack in data density, with which PCM technology can predictably cope with. Among all, the technology that is presently considered the most mature technology falls on phase change technology.

The concept based on exploiting sharp contrasts of physical characteristics between amorphous and crystalline phases of so-called *phase change materials* (PCMs) has been developed, widely implemented and commercialized in the last years, particularly as an optical storage device such as compact disc (CD), digital versatile disk (DVD) or Blu-ray disk (BD) and high-definition digital versatile disks (HD-DVD) [22-25]. Yet, the concept of PCMs has been rejuvenated and today it is not anymore magniloquent to state that phase change technology becomes a particularly promising approach for a quest of the next generation memory media or universal memory device [17, 26-28]. As mentioned, the continuous research on memory technology is at the moment in the frame of inventing an alternative memory media which bridges the gap between two prominent storage and memory device, namely a non-volatility as found in Flash memory and HDD with good programming speed and endurance as found in DRAM [8, 17, 29-31], with of course a big potential for its scalability into small size cells. The combination of two features is most desirable for its implementation especially in mobile devices. Phase change random access memory (PCRAM) emerged as a concept of memory media employing a switching of the states of the small material volume within a memory cell using Joule signal. It is commonly termed under trade name of Storage Class Memory (SCM), see Fig. 1. Hence, PCM is considered most prospective platform to single-handedly tackle both issues, i.e. in further scalability and in von-Neumann bottleneck, which can be feasible through co-location of both processor and memory units. Basic arithmetic computational tasks have been done as a prototype for the applicability of phase change-based technology within this context, showing a fast speed with a good energy-efficiency [32-34].

As mentioned, the ultimate goal within this frame of research is to produce a memory device with all properties approaching the all aforementioned ideal requirements. Tremendous efforts have been dedicated from which two approaches can be differentiated: (i) device's improvement *via* memory cell geometry and (ii) the quest of new materials and on basic optimizations *via* **materials tailoring**. The former deals mainly on finding the optimum memory cell designs and architecture. The later approach deals mainly with finding an optimum material composition as well as engineering the materials structures [35, 36]. The both approaches are mutual-complementary as the device functionality, scalability and reliability are governed by the PCRAM cell's design and material's characteristics being used as an active area in the cell at the same time. In other words, the specific set of materials properties is necessary for certain cell design, and *vice versa*.

1.2. Scope and organization of this thesis

This thesis mainly deals with the second approach as elaborated previously, i.e. in material engineering standpoint. The work mostly focuses on the *deposition of epitaxial chalcogenide thin films and superlattices (SLs) arrangements* of the technologically important alloys within GeTe-Sb_2Te_3. Specifically, the scope of the work is restricted by dealing only with the most technologically-important alloys residing in the two end-points of the pseudo-binary line: GeTe and Sb_2Te_3, and the prototypical alloy $Ge_2Sb_2Te_5$ (henceforth called GST225). The (111)-oriented Si substrate is chosen as the main substrate used for the growth of epitaxial films and SLs due to its technological relevance.

This thesis is presented in seven chapters. Chapter I of this thesis gives the background of the research. The overview of the current technologies in data storage and memory are briefly given in order to collate and locate the current state of development in phase change technology. In the following parts, the technologically-relevant reasons of why the specific materials and methodology is chosen for investigation would be described in Chapter II. The several concepts of data storage and memory device based on PCM will be firstly presented comprehensively. The state-of-the-art issues including the proposed switching concepts and novel material engineering, i.e. concept of epitaxial thin film and SLs, would also be discussed, from which, the possible routes for device improvements based on those newly-introduced concepts could be prospected. At the end of the chapter, the aims of this work could be drawn based on the previously described rationale and hence the novelties of the work would be also presented. Since this work mainly focuses on structural properties of chalcogenides, the discussion on physical and structural properties of chalcogenide alloys is presented in following section (Chapter III). The three main chalcogenides materials, GeTe, Sb_2Te_3 and GST225, are to be elaborated. In Chapter IV, some experimental methods are explained. The sections presenting the results and discussions that would be divided into two parts. The first part (Chapter V) presents some results and discussions on epitaxial growth of GeTe, Sb_2Te_3 and GST225 thin films and the second part (Chapter VI) deals with fabrications of GeTe-Sb_2Te_3 superlattice (SL) structures. The final part (Chapter VII) contains the conclusion of the work which includes also some potential outlooks.

Chapter II
Phase change technology: descriptions and current issues

2.1. History, general concept and current technology

Today, the PCM has become the leading technology for the next-generation memory devices and reconfigurable electronics. The concept of PCM for data storage media was introduced by Ovshinsky [37] in the late 60s, wherein the possibility to switch the material states has been demonstrated, i.e. between the low- and high-conductive states, using electric signal by observing a today-so-called 'threshold switching' phenomena. It is a reversible change (significant increase) of conductivity when voltage applied to chalcogenide thin film reached a certain value, V_{th}. Within the region around the V_{th}, the V-I characteristic is not Ohmic anymore, and in turn, current can be varied without significantly changing the voltage. It has been proposed that this phenomenon is a new concept which could be developed to be more feasible for an application in data storage device when a material could be reversibly-switched structurally in order to preserve the high conductivity state. However, the materials used were mainly $Ge_{15}Te_{85}$ doped[1] typically with sulfur or antimony, which show rather slow crystallizations [38-42].

Although the first proposal for the use of phase change concept in memory technology was mainly under principle of electronic switching, however, the phase change technology first came to its success in consumer market for its optical devices. Following the findings of compounds with faster crystallization speed, e.g. GeTe [43] and $Ge_{11}Te_{60}Sn_4Au_{25}$ [44], Yamada, et al. [25, 45, 46] started the investigation on materials within the pseudo-binary line of GeTe-Sb_2Te_3 and turned the PCM's application to be feasible for optical data storage media. It then led to the vast commercial market of these ubiquitous optical memories such as CD, DVD and most recently Blu-ray disks and HD-DVD. The more attentions are garnered especially on $Ge_{40}Sb_{20}Te_{40}$ and $Ge_{22}Sb_{22}Te_{55}$ which were discovered exhibiting low switching speed <50 nm [47].

---

[1] The term doping in the field of phase change technology refers to a *large amount* of dopants concentration (could be >15 at.%), which is different than that in many other classes of semiconductor materials, commonly referring to very small concentration of dopants

[2] PCR refers to phase change regenerator

[3] DVD RW refers to DVD re-writeable

[4] DVD RAM refers to DVD random access memory

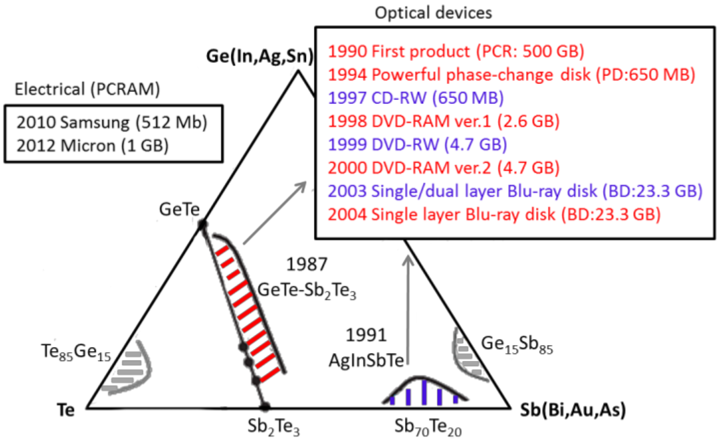

Fig. 2.1. Ternary phase diagram of Ge, Sb, and Te, which is adapted from [28]. In the inset, some commercial optical data storage products are presented with their years of release. The on-line colors correspond to the material classes within the tri-phase diagram marked by color-shaded areas. The electrical phase change random access memory (PCRAM) devices also started to be introduced into the consumer market [48, 49].

A comprehensive list of materials featuring phase change properties has been nicely compiled by Wuttig, *et al*. [28], as seen in Fig. 2.1. The most important compounds to be used as data storage are the ones residing in the two regions shaded with red and blue colors. The alloys residing in the ternary phase diagram of germanium (Ge), antimony (Sb) and tellurium (Te) satisfy the required attributes to implement as a phase change material for data storage or memory media. Some improvements in properties for these materials have also been sought for a better device performance and applied in many commercial products, for instance by alloying with new elements, such as GeBiTe [50], BiGeSbTe [51], SnGeSbTe [52], *etc*., and by elemental doping, e.g. by Ag, In or N, O, or Ti [53-56]. A good example is Ag-In-doped alloy $Ag_5In_5Sb_{60}Te_{30}$ (AIST) which is commonly employed in commercial DVD-RW [57]. As explained, more particularly main attentions fall into the last family consists of alloys residing on the pseudo-binary line of GeTe-Sb_2Te_3 and its vicinity, as depicted by the region shaded by red. Some important alloys are GeTe, $Ge_1Sb_2Te_4$, $Ge_2Sb_2Te_5$, or $Ge_3Sb_2Te_6$ and Sb_2Te_3. The alloys lying on the binary line GeTe-Sb_2Te_3 is still up to now considered as one of the best alloys to employ as a memory device [17, 28, 58]. Hence this work focuses only on the alloys within GeTe-Sb_2Te_3 which are often so-called GeSbTe (or simply GST).

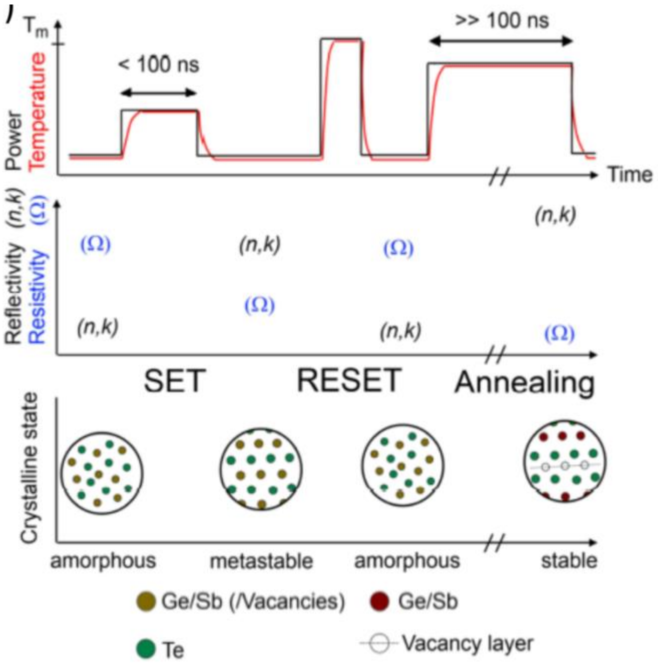

Fig.2.2. General switching protocol in GeSbTe phase change material used for data storage media. The image is taken from [59] as adapted from [60]. Despite the use of optical and electrical pulses, phase change can also be attained by annealing process, usually resulting in a transition to a stable phase.

The general work concept of the data storage devices can pictorially be seen Fig. 2.2. It is based on exploiting the pronounced contrasts in its optical properties, referring to its optical constants of n and k in term of reflectivity, and in its electrical properties, referring to its dynamic resistivity, Ω, between two or more well-defined states of the material, the amorphous phase and the crystalline phases. The large ratio in optical reflectivity is around 20%, while that in electrical resistivity is in four or five order of magnitude [61]. The reversible material's phase change is possible between these phases occurs in a few nanoseconds, which can be attained by an exposure on the material to an optical (laser beam) or electrical (Joule heating) pulse. In a data storage device, a small volume of highly resistive and lowly reflective amorphous material (RESET or "0" state) in a crystalline matrix is crystallized by heating up the material well above its glass transition temperature, T_g, using a relatively long-duration, low-intensity pulse, to render the material low-resistive but high-reflective crystalline (SET or "1" state). As explained, the power can be in the form of a pulsed laser beam (optical device) or pulsed electric current (electrical device). The typical laser length is less than 100 ns, to ensure a good programming speed of a device. Counter-intuitively, the crystalline phase can be switched back to amorphous phase by applying an intense pulse to increase the temperature above melting temperature T_m to melt the spot, which is subsequently quenched to freeze the disorder, rendering the volume amorphous. It is required that the cooling process, occurring after the power is off, must be faster than its critical cooling rate (R_z), i.e.

typically approximately $10^9 - 10^{11}$ K/s [28], to avoid it from a re-crystallization. The states of the material after switching, i.e. either SET or RESET state can be read out by measuring reflectivity $(n,\ k)$ using a low intensity laser (optical) or by measuring the resistivity value, Ω, using a low current through the small volume (electrical). The use of a low reading power is intended to avoid any possible phase transition due to heating.

The great expectation on PCM is based on its several criteria when it comes to its prospective application as an active material for a memory cell: (i) its non-volatility, (ii) its significant electrical (or optical) contrast between two polymorphic states, (iii) its ultrafast programmable speed to ensure the high speed of memory device (PCRAM was shown having the programmable speed in the order of four, faster than Flash (see Fig. 1) [9]). More recently, Bruns, *et al.*, have shown a GeTe-based electrical device showing a switching speed in nanosecond timescale [31], which was followed by Loke, *et al.* [62] demonstrating GeSbTe-based device with sub-nanosecond switching behavior. This evidenced that PCM-based memory device is commensurate with DRAM technology in term of programming speed. (iv) Its scalability, i.e. recent PCRAM cells are lithographed to sub-10 nm [13, 63]. Additionally, the PCRAM device with only 3-nm thick doped GeSb film was fabricated and shown switchable [64]. In fact, there is a close correlation of programmable speed and scalability in PCRAM device, wherein the reducing PCRAM size implies on a significantly faster crystallization/amorphization time [65]. (v) Moreover, it is necessary to have a long-time retention, which is the ability to store a great amount of data in a small space in a long time span (typically 10 years) at operating temperature, typically from 85 °C (as in embedded memory) to 150 °C (in automotive application) [66]. The measure of phase stability is often determined using Arrhenius extrapolation [67]. (vi) PCM also must be good in endurance without losing its switching speed. The metric of it is the ability of the materials to be switched between two states in high number of switching cycles. The memory cell enduring approximately $10^9 - 10^{12}$ switching cycles without bit loss has been reported [28, 68, 69] in order to compete with Flash ($10^6 - 10^8$ cycles) or go towards that of embedded memory (10^{12}) or DRAM ($10^{15} - 10^{17}$) [66]. (vii) The last but not least is its low energy consumption, which is prerequisite mostly for mobile devices. (viii) Nonetheless, a commercial device must be kept nominally low in price.

2.1.1. Realization of multi-level storage device

Despite its success in the consumer market as optical data storage, another route of its application is through the electrical properties switching by means of electric signal. This concept was actually been initialized since the beginning of PCM invention [37], yet it is only recently that the first PCRAM products entered the market. [48, 49]. One of two main designs used for realizing a PCRAM device is so-called Ovonic Unified Memory (OUM) [70-72]. Another most prominent cell's design, e.g. ‘line cell’, has been fabricated as an alternative to the commonly used OUM cell [9, 73, 74], mainly to cope with the issue on minimizing energy loss due to surrounding contacts of the active area, resulting in a lower programming power. The comparison between both designs can be found in ref. [60]. However, OUM is the more common design mainly due to its smaller geometrical size.

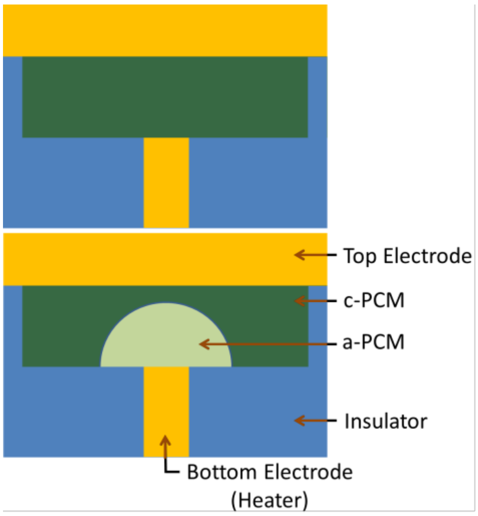

Fig. 2.3. OUM (or mushroom) cell. The crystalline active area (*c*-PCM) is changed to amorphous (*a*-PCM) in the form of cap.

Fig. 2.3 shows the simplified OUM cell. The cell basically consists of active PCM contacted by two electrodes at both sides. The upper electrode covers the surface, while the other electrode is cylindrical. The other region is occupied by insulator (e.g. SiO_2) material. At first, the active volume is totally crystalline, as depicted in Fig. 2.3a. In the case of GST as an active material, in contrast to optical devices where the stable structural phase is supposedly not present, in PCRAM both crystalline phases, the metastable and stable phases can be present since the final-heating-process of the fabrication line includes the crystallization of the active volume is attained by heating processes, e.g. for 400 °C for 30 min [66], by annealing in the oven or by Joule heating in the cell, resulting in *polycrystalline* material with grain sizes ranging from 8 to 20 nm [75].

The switching process to amorphous phase volume is done by Joule heating of the lower cylindrical electrode, as was explained in Fig. 2.2. As a sharp pulse is applied (RESET operation), the active material is heated above melting temperature T_m which then is quenched into disordered amorphous phase (see Fig. 2.2 for further explanation) close to the bottom electrode. The newly-formed cap-like amorphous volume geometrically resembles the form of a mushroom, see Fig. 2.3, from which OUM cell is popularly termed *mushroom cell*. The reverse switching is done by applying moderate longer pulse above T_c. The reading process is done by measuring the electrical properties by flowing low intensity current. In the frame of this memory cell design, multi-level cell (MLC) has been successfully realized [76]. It exploits the distinctly different degree of amorphization which can be read out into 2^n distinct states associated to logical numbers, with *n* refers to the number of bits. For *n*=2 a single cell can produce four different states ("00", "01", "10" and "11"), which implies on tremendous increase of device's data density. The device with *n*=2 and *n*=4 has been demonstrated by Nirschl *et al.* [76]. This issue on quenching speed and also energy consumption becomes more important particularly in PCRAM cell since it is dependent on the cell's geometry [70, 73, 77].

2.2. Recent advances in phase change technology

Scientific interests on GeSbTe materials especially for its application in memory devices have been drastically increasing within the last 15 years. This is probably due to the fact that phase change technology is the most mature candidate for memory application [10] besides the other contenders. Some main issues have been tackled and other technologically relevant concepts are proposed in the field of PCM.

2.2.1. Switching mechanisms in chalcogenide PCM

Despite the fact that the PCM technologies have gained its great success within the last decade, yet a complete paradigm to understand the underlying switching mechanism in PCM has not been completely built. It has led to a discussion about the underlying phase transformation kinetics down to atomic scale, which was assumed to be simple, due to the fact of ultra-fast transformations between amorphous and crystalline states and the stability of the both states, as the primary features of PCM [28].

One of the most successful ideologies is in this part of thesis explained. One of the earliest and commonly believed mechanism responsible for this phenomenon is called *'umbrella-flip'* transformation [78]. Fig. 2.4 depicts the artistic representation of the switching model [78]. The image shows a small fraction within local structure of cubic GST around Ge atom. The Ge and Te atoms are pictured as green and orange balls, respectively. Within this mechanism, the Ge atom is shifted along $\langle 111 \rangle$ direction while transforming from octahedrally-bonded configuration in crystalline state (Fig. 2.4a) to a tetrahedral-bond (or can also occupy a three-fold site) [79, 80] in amorphous phase (Fig. 2.4b). The transformation can be done reversibly from amorphous to crystalline states by coordination number reconfiguration from tetrahedral to octahedral. To note, the transformation also involves the breaking of the weaker inter-block Ge-Te bonds in crystalline state, depicted by thinner line in Fig. 2.4, and preserving the stronger covalent bonds in amorphous state, represented by thicker line. In amorphous phase, the atoms are covalently bonded, hence obeying $8 - N$ rule [81]. This switching model is indeed satisfactory for explaining ultra-fast transformation occurring within PCM, since it simply relies on the movement of single atom Ge in the scale of atomic distances within fraction of the local structure.

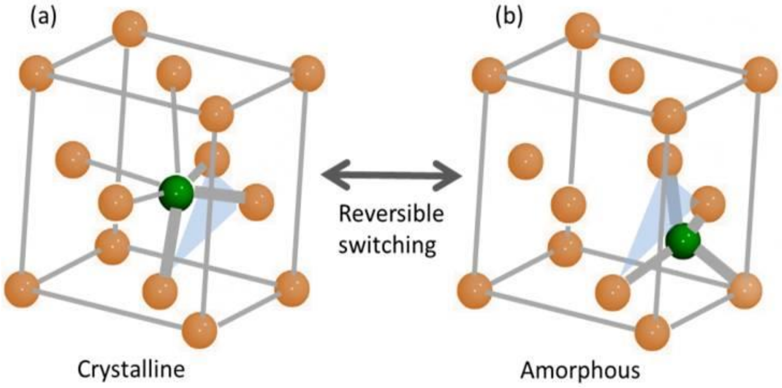

Fig. 2.4. ‘Umbrella-flip’ mechanism within GST225 local structure proves a simple atomic Ge switching during reversible switch from (a) crystalline to (b) amorphous states. The green and orange colored balls represent Ge and Te atoms, respectively. The thicker lines connecting atoms represent strong covalent bonds, while the thinner lines interblock bonding. The model explains the fast transformation and phases stabilities (adapted from [78]).

However, the simple atomic movement within ‘umbrella-flip’ model itself is not enough to explain another phenomenon found in PCMs, namely the large optical contrast between crystalline and amorphous states. Sphortko, *et al*. [82] determined the optical parameters, by employing Fourier transformed infra-red spectroscopy (FTIR), which include Born effective charge (Z^*) and optical dielectric constant (ε_∞) of the phase change alloys, i.e. $Ge_1Sb_2Te_4$ and non-phase change alloy, i.e., $AgInTe_2$ thin film. They observed that PCM possess the remarkable contrasts of Born effective charge (Z^*) and optical dielectric constant (ε_∞) on crystallization from amorphous to crystalline phase. There must be more fundamental reason, i.e. a change in bonding characteristic within the material during transformation.

In many tetrahedrally-bonded semiconductors such as Si, Ge, GaN or GaAs, the average number of *s*- and *p*-electrons per atom is four, whereby the bonding in crystalline state is characterized by sp3-hybridization *via* two-center two-electron bonding characteristic, i.e. referring to two electrons being shared by two atoms, configuring the atoms into diamond-like structure. In means, a pair of electron is shared by two atoms employing a covalent bond. Instead, phase change alloys such as GeTe, $Ge_2Sb_2Te_5$ and Sb_2Te_3 possess an excess number of *s*- and *p*-electrons, i.e. slightly above four electrons per atom. It means that when sp3-hybridization is to be compelled to happen, the sp3-hybridization antibonding states must therefore be occupied. This situation is of course energetically unfavorable. Therefore, that leads to a conclusion that only *p*-electrons are going to take a role for bonding in PCMs. This means that octahedral configuration, instead of tetrahedral, is preferred.

Another problem then emerges. The average number of *p*-electrons per atom in many PCMs like GeTe and Sb are three. However, the first calculation of the number of nearest neighbors is six. It means that there is a lack of electrons for a formation of saturated bond, i.e. three *p*-electrons per atom are not enough for an occurring of two-center two-electron bonding. Instead, the alloy would prefer to configure themselves forming so-called three-centers-two-electrons bonding, in which two electrons are shared by more than two atoms. This kind of bond is also so called *resonant bonding* [81, 82]. This implies on the presence of Peierls distortion [83] within the crystals, and concomitantly bonding energy hierarchy within the crystals of PCM. Consequently, instead of forming ideal octahedral bonding configuration, it features three shorter covalent bonds and three longer resonant bonds within the crystal. The change in Ge atom coordination along with the resonant bonding can explain the optical contrast of the alloy. The distortions in crystals altogether with the presence of vacancies render the fast crystallization. Unlike in the metallic bonds, the electrons within the resonant bonds are still somewhat localized. Kolobov, *et al.* [84] shows the electron charge density along these bonds, together with other materials with different type of bonds, i.e. covalent bonds in Si, ionic bonds in NaCl and metallic bonds in Cu, as seen Fig. 2.4, showing the electron charge density within crystals with various bonding types.

Furthermore, the concept of resonant bonding in crystalline chalcogenide PCM is convenient to explain a recently-observed interesting phenomena, namely so-called picosecond optical switch in PCM through a *non-thermal switching* route [84, 85], in which the role of the bonding hierarchy is mainly involved within the switching and the switching only involves crystalline phase without melting-quenching process which require the most significant amount of power. This paves a new route in research of PCM towards an advanced optical memory device with significant efficiency in energy consumptions.

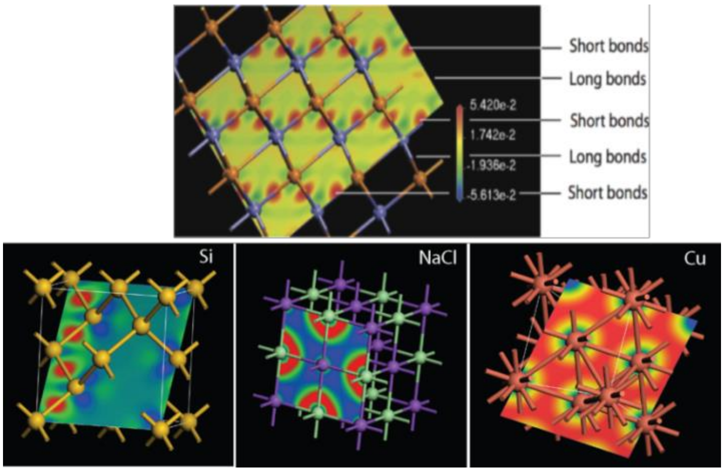

Fig.2.5. Electron charge density with the presence of bonding energy hierarchy in GeTe crystal in comparison to other bonding types, adapted from [2].

Other switching processes are proposed in superlattice (SL) structure of chalcogenide PCM where selected atoms are unidirectionally mobilized from bulk layer into the layer interfaces [36] that will further explained as follows.

2.2.2. Novel concept of chalcogenide superlattice (CSL)

As mentioned, two distinguishable approaches are paved in order to improve a performance of memory device, in terms of switching speed, switching endurances and efficiency in energy consumption, the properties mostly crucial for its application in portable and mobile device. Besides an approach in device cell's architecture, another approach is in its 'material tailoring' standpoint. In this frame of concept, a new concept recently emerged as a promising route in obtaining significantly better material performances for its application in PCRAM cell by tailoring chalcogenide GeSbTe superlattice (SL) structures.

In 2006, Chong, *et al.* [87] pioneered the work within this path of material research in chalcogenides, more specifically alloys residing in GeTe-Sb_2Te_3 pseudo-binary line, by fabricating a chalcogenide multilayer structure (so-called superlattice-like or SLL). Two alloys were chosen. GeTe with slower crystallization speed but greater crystallization temperature, T_c, and melting point, T_m, and Sb_2Te_3 with relatively better crystallization speed but poor stability. It is worth to note that by considering the set of properties belong to each alloy, each individual alloy is not suitable to implement as an active material for PCRAM device. By the use of the multilayer structure of the both different alloys, they showed the reduced SET and RESET programing currents and shorter switching pulse, higher over-writing cycles and good stability, compared to its counterpart, i.e. the single alloy $Ge_2Sb_2Te_5$. The SET and RESET operations happen between (partly) amorphous to polycrystalline phases. They suggested that the decrease of thermal conductivity of this multilayer structure bears the main responsibility for the improved switching performances.

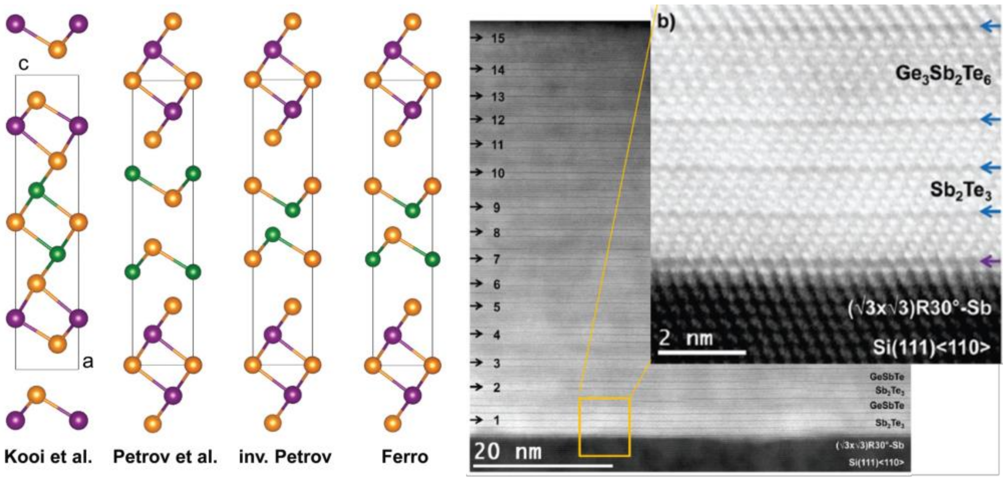

Fig. 2.6. (a)The crystalline models of nominal $(GeTe)_2(Sb_2Te_3)$ superlattice structure involved in the proposed switching models. The Petrov, inverse-Petrov and Ferro states are constructed out of distinct stacking of GeTe and Sb_2Te_3 crystalline layers. (b) The real structure of chalcogenide superlattice consists of intermixed GeTe and Sb_2Te_3 building blocks, resulting in GeSbTe layers [88].

The work was followed by Simpson and colleagues [36] by fabricating so-called interfacial phase change memory (iPCM). The memory cell is constructed out of chalcogenide superlattice (CSL) structure of GeTe and Sb_2Te_3. In contrast to previously reported by Chong, *et al.* [87, 89], here the layer thickness of GeTe are scaled down, i.e. $\leq 1nm$ (~2 bilayers GeTe), and the GeTe and Sb_2Te_3 layers are epitaxially stacked to each other alternately in *c*-axis direction. The device was demonstrated outperform its contender, single alloy $Ge_2Sb_2Te_5$, in terms of faster switching speed, lower switching energy and improved stability and endurance [36]. Another physical phenomenon was suggested responsible for the improved switching characteristic, in which the switching was proposed based on the one-dimensional movement of Ge atom in the interfaces. Hence, an entropic lose is avoided and the complete transformation between crystalline-amorphous states is not necessary to occur. Instead, the structure remains crystalline in the whole switching process, as confirmed by transmission electron microscopy (TEM).

However, despite its remarkable improvements in performance shown by CSL, the switching mechanism within the CSL structure is still unclear. Some scenarios were proposed to explain the switching mechanisms in CSLs. Fig. 2.5 resumes the proposed structural models of the CSL showing crystal structures of nominal $(GeTe)_2(Sb_2Te_3)$ stacked along c-axis. The crystal configurations are involved within the switching process in the CSL. Two mainly-believed switching mechanisms exist. First one is by Tominaga, *et al.* [90, 91] in which a scenario of so-called 'single umbrella-flip' switching was proposed occurring between inverse Petrov (high-resistance state) and the Ferro (low-resistance state), see Fig. 2.5. Another mechanism was suggested by Ohyanagi, *et al.* [92] is the 'double umbrella-flip' switch involving the Petrov (low-resistance) state and inverse Petrov (high-resistance). Another model structure is based on *ab initio* calculation of the structure of stable $Ge_2Sb_2Te_5$ at 0 K, as proposed by Kooi *et al.* [93], depicted in Fig. 2.5a. This structure is proven to be unfavorable when the temperature increases to around 180 °C [90, 91, 94]. Furthermore, Kalikka, *et al.* shows interesting way to manipulate Ge- and Te-atomic diffusivities within the CSL by tuning the strains between the two different layers [207].

All of the aforementioned switching proposals within crystalline structure of CSL are based on the assumptions that the stacking sequence in the CSL and distinct interfaces between GeTe and Sb_2Te_3 thin layers are ordered. However, the recent observation by Momand, *et al.*, using TEM [88] proved that the real structure actually consists of layer intermixing at GeTe and Sb_2Te_3 interfaces, forming GeSbTe building blocks. This finding of course suggested a revised underlying physics in switching process in CSLs by taking into account the layers intermixing which occurs during the typical higher temperature process, i.e. around 220 °C [88, 95], the temperature regime which is commonly used to grow the chalcogenide PCM in epitaxial/highly-oriented polycrystalline by means of physical deposition techniques, hence the intermixing is considered inevitable to occur. Hence, it can finally be concluded that despite the vast commercialization of phase-change devices, the underlying mechanism especially in switching events is still up to now not completely clear.

2.3. Aims of the thesis

From the holistic overview about the state-of-the-art issues in the field of PCM, it could be concluded that the improved switching characteristics were shown by a more ordered GeSbTe material, particularly in the form of CSL [36, 87, 96], which is one of the most desirable features for current devices. Despite its advancements, the working concept of the materials especially when talking about switching principle in the alloys and superlattice is not yet completely clear. Hence, depositions of thin films with better crystalline order as well as chalcogenide superlattices are of importance in scientific point of view. This will expectedly provide a platform for a better understanding the underlying physical phenomenon, of which the investigation of structural kinetics in critical events, e.g. in switching process, becomes a formidable task due to pre-existing grain boundaries typically present in polycrystalline samples. Those hindrances could be suppressed by the fabrication of the thin films with crystalline quality towards single crystalline. An effort for fabrication thin films towards a single crystalline chalcogenide and their CSLs is indispensable in the industrial point of view as well, since energy consumption, switching speed and device stability is one of the main issues in this topic as previously elaborated [36, 96].

The thesis has two main goals, namely (1) depositions of epitaxial chalcogenide thin films of the alloys residing within the pseudo-binary line of GeTe-Sb_2Te_3, and (2) fabrications of chalcogenide superlattice (CSL) structures using pulsed laser deposition (PLD). The technologically important alloys, i.e. GeTe, $Ge_2Sb_2Te_5$, and Sb_2Te_3 are investigated. Some reports were published for the fabrications of the epitaxial chalcogenide thin films and the CSL structures thereof. The common methods for fabrications are sputtering technique and molecular beam epitaxy (MBE). By sputtering, the resulting thin films are predominantly oriented polycrystalline, while by MBE the epitaxial thin films and superlattices can be produced. Within this frame, PLD potentially offers a good platform to fabricate epitaxial GST [97]. The different characteristic of PLD than other techniques is interesting to explore with the hope to cope with some limitations commonly found in other techniques. The detail about PLD could be found in Chapter IV. However, to the author knowledge, only very few reports of fabrications of epitaxial chalcogenides film [98] and there is not yet reports on a fabrication of its CSL structure using PLD.

The silicon substrate is chosen as a substrate for the growths of epitaxial GeSbTe films and CSL structure due to its great technological relevance. Si substrate is expected to be compatible with the common interface found in today's electronics hence expectedly provides a 'hybrid' technology between current transistor-based technology and the phase change memory technology. More specifically, the (111)-

oriented Si substrate is mainly used in this set of work. The growth GST thin film is more influenced by substrate orientation than substrate material, where (111)-oriented GeSbTe films are preferred disregards the orientation of the substrate being used [99]. This will also be confirmed by depositing $Ge_2Sb_2Te_5$ (GST225) on Si(100) using PLD (see Chapter 3).

2.4. Scientific novelties in this thesis

As mentioned, the ultimate goal of the thesis is to synthesize chalcogenide superlattice (CSL) structures with a good crystalline order on Si(111) using PLD. Fabrications of thin film alloys as the constituting materials are essential to understand the growth behaviors of each alloy by means of PLD. Hence, some novelties of the thesis can be extracted out from this set of work on depositions of epitaxial chalcogenide thin films and superlattices by PLD, as follows:

1. To demonstrate a fabrication of good quality epitaxial GST225 by means of PLD on Si(111) substrate. PLD offers of many degrees of freedom to fabricate epitaxial GST on Si substrate with various crystalline structures with a relatively high deposition rate. By employing the right process parameters, the epitaxial GST film possesses metastable rock-salt structure with randomly-occupying vacancies (phase I) and metastable structure with ordered (phase II) vacancies, as well as stable trigonal phase can be fabricated. This provides a platform to investigate the real atomic arrangements of the crystals by means of HR-STEM.
2. The overview of growth mode of epitaxial GST on Si(111) by means of PLD by presenting the *in-situ* observation during the growth process by means of RHEED system. A broad overview of completed crystalline phases evidenced by systematic experimental data, i.e. XRD and HR-STEM, from metastable rock-salt (phase I and phase II) to stable trigonal phase of GST. This shed a complete insight of crystalline structures of GST material. The presented results of multi-phases in crystalline structure of GST also show the future application of chalcogenide PCM as a multi-level data storage media.
3. A good quality exclusively trigonal-GST phase thin film with micro-sized grains are realized.
4. By varying the process parameters, i.e. laser frequency and fluence, epitaxial GST thin films can be deposited on Si(111) with high deposition rate up to 42 nm/min.
5. The deposition of epitaxial Sb_2Te_3 thin films on Si(111) through a van der Waals (vdW) epitaxy. The growth mode as well as crystalline structure and local structures of the films are also investigated.
6. The deposition of GeTe thin films on Si(111) by PLD. The growth mode as well as crystalline structure and local structures of the films are also

investigated. To improve the epitaxial nature of GeTe, the vdW-bonded material Sb_2Te_3 is employed as a seeding layer. The epitaxial window can substantially be extended especially towards lower temperature regimes up to 145 °C. Additionally, the surface quality is significantly improved.

7. The depositions of chalcogenide superlattice structures by means of PLD are for the first time demonstrated. The deposition of CSL using PLD has higher degree of freedom, in which low temperature regime can be used to control the degree of intermixing between layers. The process parameters determine the degree of intermixing commonly found in CSLs.

Chapter III

Chalcogenide phase change materials: physical and structural properties

As mentioned, one of the most interesting features of the binary line Sb_2Te_3-GeTe is the characteristics of crystalline structures spanning from Sb_2Te_3 to GeTe [100-102]. In this chapter, the physical and structural properties of the main alloys within the binary line is discussed, which includes GeTe, Sb_2Te_3 and $Ge_2Sb_2Te_5$ (from now on so called GST225).

3.1. Crystal structure of GeSbTe

Despite their vast commercialization, the discussion on the crystal structures of both metastable and stable GST crystals are actually still not fully finished, especially in terms of the occupations of Ge/Sb atoms and vacancy orderings. As explained, depending on its chemical composition of specific GST alloys, each alloy features a significant amount of vacancies. However, since the introduction of chalcogenide phase change alloys within the quasi-binary GeTe-Sb_2Te_3 by Yamada, *et al* [44], among them is GST225 which has been attracting great interests for its applicability as an active layer for a commercial data storage device [52, 103]. Owing to its optimum properties in terms of speed, stability and optical/electrical contrasts between two phases, the compound is regarded as prototypical alloy of the binary line GeTe-Sb_2Te_3. Hence the structural information of GST225 can be representable when discussing over crystalline structures of GST alloys.

From an initial amorphous phase, the alloy crystallizes into its metastable phase at ~150 °C [104]. Studies based on X-ray diffraction (XRD) [100-102], extended X-ray absorption fine structure (EXAFS) [78, 105], transmission electron microscopy (TEM) [93, 106] as well as first principle calculations [107-109] suggested that the metastable GST225 phase, analogously to the metastable GeTe phase, possess a distorted rocksalt-type (so termed c-GST225) [78]. For practical reason, the distorted structure of the metastable phase is simply regarded as a rocksalt structure, as presented in Fig. 3.1, showing the existing polymorphs of the crystalline GST225. The structure possesses the lattice parameter of ~0.603 nm [110, 111]. The calculated lattice mismatch to that of Si, according to GST225(111) ‖ Si(111) and GST225$[1\bar{1}0]$ ‖ Si$[1\bar{1}0]$ relationships, is ~10.7%.

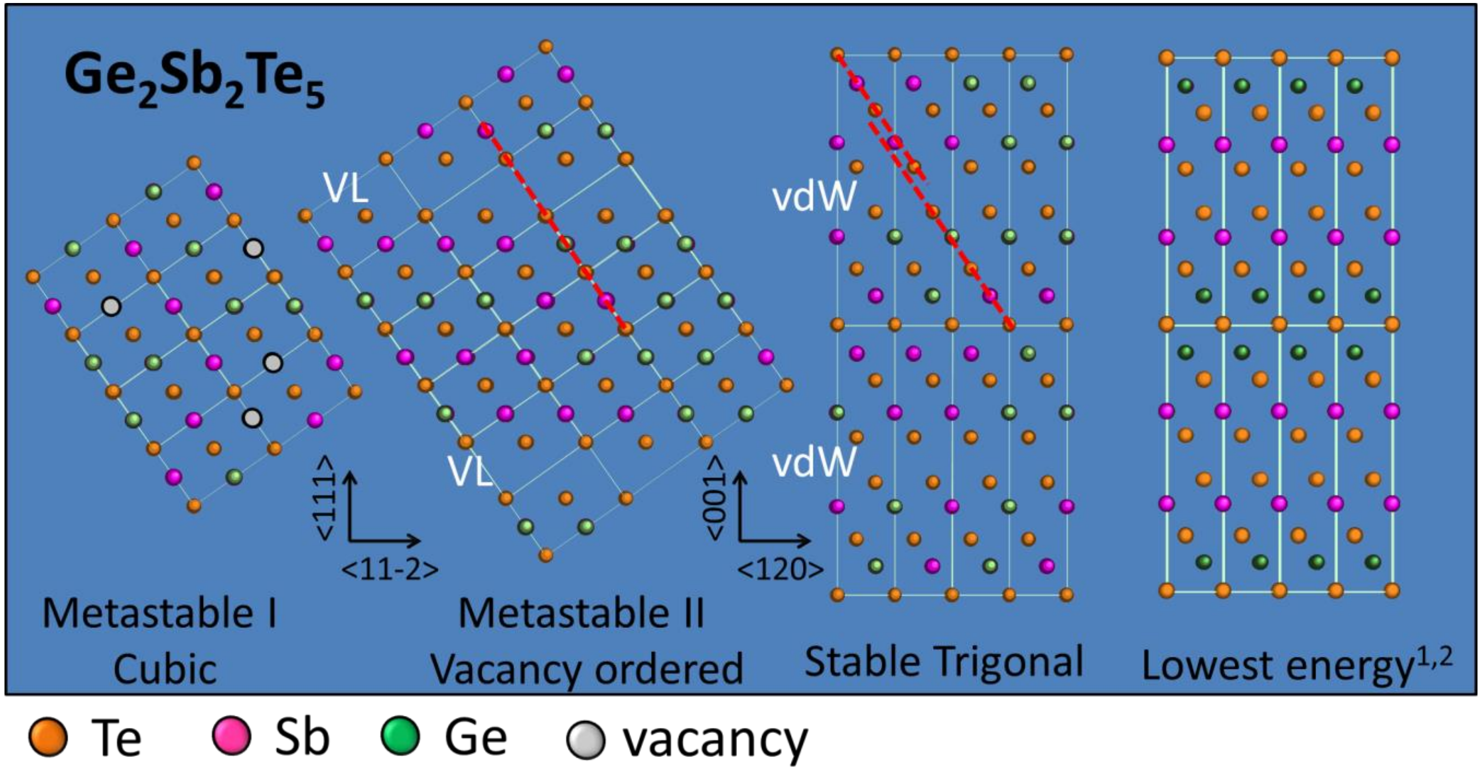

Fig. 3.1. The crystalline polymorphs of $Ge_2Sb_2Te_5$ are pictorially depicted. The GST crystal obeys Oswald's step rule [1] where the material would firstly crystallize in the least stable phase (metastable phase type I) in distorted rock-salt structure with large amount of vacancies randomly occupying the cation sites. The gradual transition is marked by the movements of vacancies into a specific {111} planes, e.g. upon annealing, forming the second metastable (type II) with ordered vacancies. Further transition can occur by vertical and horizontal movements of lattice planes of metastable type II forming a stable with atomic columns are no longer continuously parallel to each other across the resulting gap as marked by dashed red lines. The number of atomic planes can be 7, 9, or 11, corresponding to chemical compositions.of $Ge_1Sb_2Te_4$, $Ge_2Sb_2Te_5$ and $Ge_3Sb_2Te_6$, respectively.

For the c-GST225 phase, some studies proposed that Ge, Sb atoms and a high concentration of intrinsic vacancies ($\sim 20\%$) randomly occupy the cation sites within the rocksalt type structure [106, 109, 112]. This phase is referred to as c-GST225 phase I. Upon heating, the phase I can transform into another metastable structure [101, 108, 112, 113], in which the vacancies are concentrated in a specific individual $\{111\}$ plane along the c-axis forming so-termed vacancy layers. That latter phase is referred to as c-GST225 phase II.

A further the temperature increase, e.g. by annealing at ~300 °C [104], the metastable phase transforms into more stable phase which can be represented in a trigonal symmetry with space group of $P\overline{3}m1$ (no. 156). The lattice parameters, in hexagonal symmetry, are $a = \sim 0.4224$ nm and $c = \sim 1.724$ nm [93, 100, 114]. The structure of the trigonal GST225 (t-GST225) is strongly correlated to that of low-pressure Sb_2Te_3 structure. The overall structure of t-GST225 consists of rocksalt-type building blocks with alternating cation (Ge/Sb) and anion (Te) layers along the c-axis. Several different structure models were proposed for the t-GST225 phase [93, 100, 114]. Matsunaga et al. [100] and Urban et al. [114] proved that Ge and Sb atoms randomly occupy sites in a specific cation stacking plane for the stable phase (with the stacking sequence Te-Ge/Sb-Te-Ge/Sb-Te-Te-Ge/Sb-Te-Ge/Sb), while Kooi and De Hosson [93], argued that there is no intermixing of Ge and Sb atoms in a certain stacking plane parallel to the c-plane (Te-Ge-Te-Sb-Te-Te-Sb-Te-Ge-), referred as the low-energy structure. Recent high resolution transmission electron microscopy (HRSTEM) investigations confirmed the pulsed laser deposited t-GST225 structure with intermixed cation sites [115]. The complete (powder) Bragg x-ray diffraction profiles of GST are shown in Fig. 3.2, showing the calculated XRD peaks of (random-vacancy) cubic and trigonal phase, respectively. From the figure, the simplest way to distinguish both phases is by checking the existences of reflections of the hexagonal basal planes in the trigonal phase at diffraction angles of $2\theta < 25°$.

From the applications point of view, only transformations between two phases, i.e. amorphous and metastable c-GST and vice versa are believed to play a role in the ultrafast reversible phase switching in many data storage devices. However, the recent discussion of three phases coexistent in GST offers possibilities of another route of multi-level phase change data storage [113]. A study of the local structure as well as of the particular role of vacancies in the transformation between the crystalline phases is of paramount importance in order to understand the switching mechanism of PCMs. The disorder-based (Anderson localization) metal-insulator transition associated with the metastable-stable phase transition is of advantage for the reproducible resistance switching characteristics of GST [85, 116]. The origin of the vacancy was explained using quantum chemical calculation, in which the annihilation of antibonding coupling between Ge-Te and Ge-Sb bonds bring about the vacancy formations. This vacancy formation, together with the formation of Peierls distortion [83], is needed in order to stabilize the crystalline structure [117, 118]. Vacancy ordering is one of foremost important issues since it is believed to play a key role in the ultrafast non-volatile PCM switching characteristics [113].

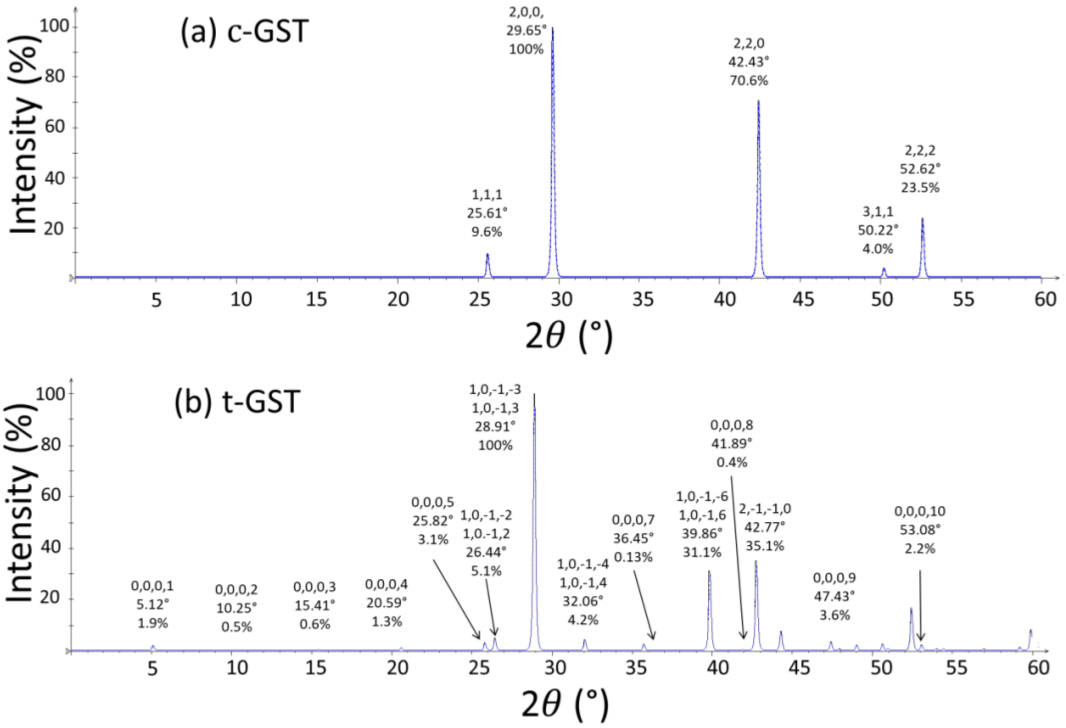

Fig. 3.2. Calculated x-ray diffraction profiles of (a) cubic GST and (b) trigonal GST phases. Each annotation shows Miller indices, Bragg angle and relative intensity [100].

3.2. Crystal structure of Sb_2Te_3

Residing in another end-point of the binary line is Sb_2Te_3. This narrow band-gap semiconductor alloy has been known as a thermoelectric material [119]. As any layered Ge-Sb-Te crystal structures [115], Sb_2Te_3 crystallizes in a rhombohedral phase which could be correlated to a trigonal crystal system with the space group $R\bar{3}mH$ or D_{3d} see Fig. 3.3a. It consists of stacked quintuple layer (QL) building blocks along the c-axis, intercalated by a weak quasi Van der Waals (VdW) gap. Hence, Sb_2Te_3 is considered as two-dimensionally (2D)-bonded material. The atomic sequence along *c*-axis is then VdW-Te-Sb-Te-Sb-Te-. The calculated (powder) Bragg XRD profile is shown by Fig. 3.4a [121].

The hexagonal cell consists of three QLs with lattice constants of $a = 0.4264$ nm and $c = 3.0455$ nm [121]. The lattice mismatch to Si is calculated to be ~11%, according to relationship of $Sb_2Te_3(001) \parallel Si(111)$ and $Sb_2Te_3[\bar{2}10] \parallel Si[2\bar{2}0]$. This feature gains much attention especially for its application as a three-dimensional topological insulator. Also, thanks to this 2D-bonding nature, by which the growth mechanism is dictated where a VdW epitaxy [122] is characterized, implying on a layer-by-layer growth mode of the material by pulsed laser deposition (PLD) even on a highly mismatched substrate Si(111) [123]. It is also potential to use as an ‘ingredient’ of Van der Waals hetero-structure [124], commensurate to other chalcogenide 2D-materials, e.g. Bi_2Se_3, Bi_2Te_3 [125]. Upon an increase of pressure the structure transforms into monoclinic phase (*C2/m*) in which vdW gap is absent, and further into disordered body center cubic with disordered Sb and Te atomic arrays ($Im\bar{3}m$) [126].

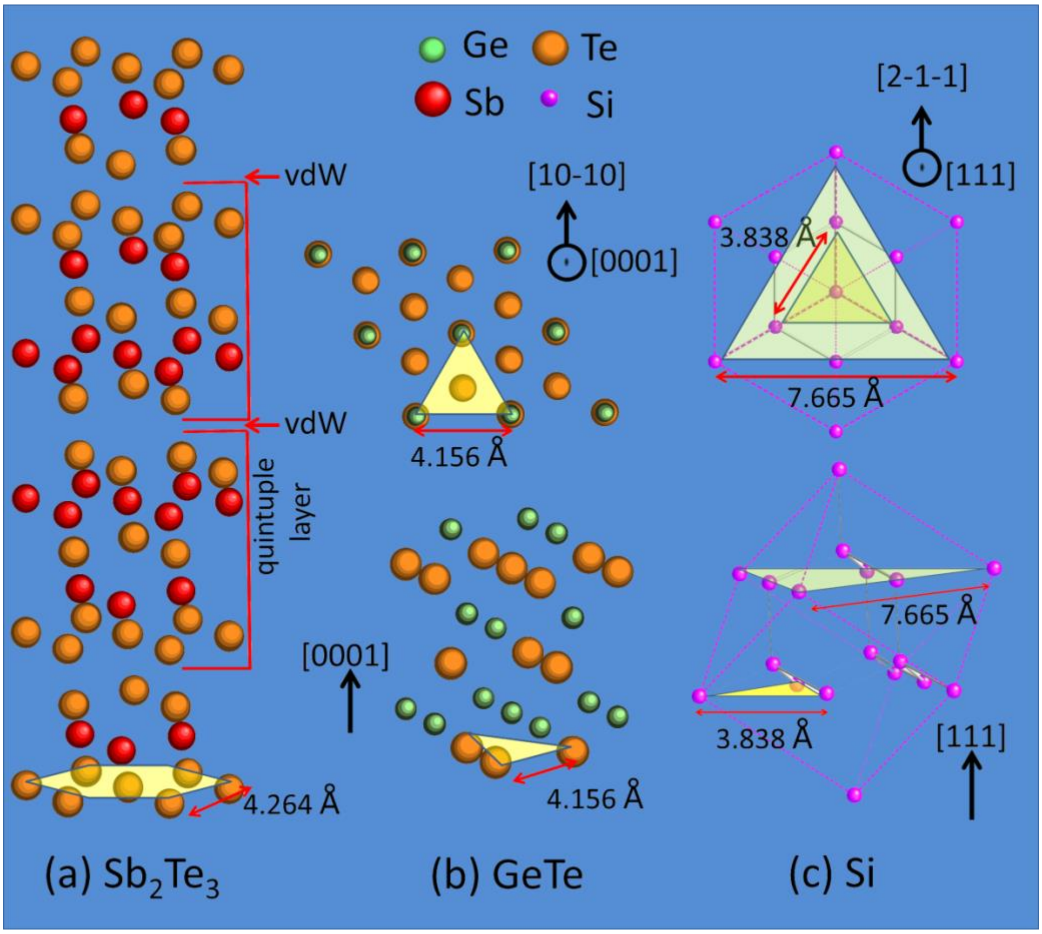

Fig 3.3. (a) Crystal structure of Sb_2Te_3 and (b) low temperature GeTe crystal in hexagonal cell configurations. In (c) diamond structure of Si is also shown. The transparent colored (yellow and green) hexagon and triangles mark the lattice constants of each corresponding crystal.

3.3. Crystal structure of GeTe

One of the two end-points of the binary line is GeTe alloy. GeTe crystallizes in trigonal structure (space group *R3mH*) [127-129], with hexagonal unit cell parameters of a = 0.4156 nm and c = 1.066 nm [127], see Fig. 3.3b. The structure of GeTe can also be depicted as rhombohedral unit cell with a = 0.4281 nm and, α = *58.36°* (space group *R3mR*) [101, 130]. The cation and anion sites are occupied by Ge and Te, respectively [101, 107, 127, 128, 130]. Ge and Te are six-fold coordinated to each other and anion or cation layers are stacked along [0001] according to *ABC* stacking, see Fig. 3.3b. The lattice mismatch to Si(111) substrate according to the epitaxial relationship of GeTe$[1\bar{1}0]\|$Si$[1\bar{1}0]$ is hence calculated to be ~8.38 %. The Bragg reflection profile of GeTe can be seen in Fig. 3.4b [127]. The hexagonal crystal setting is used, in which the prominent reflections of e.g. (0003) and $(10\bar{1}2)$ planes are equivalent to (111) and (110) planes, respectively, in cubic crystal setting.

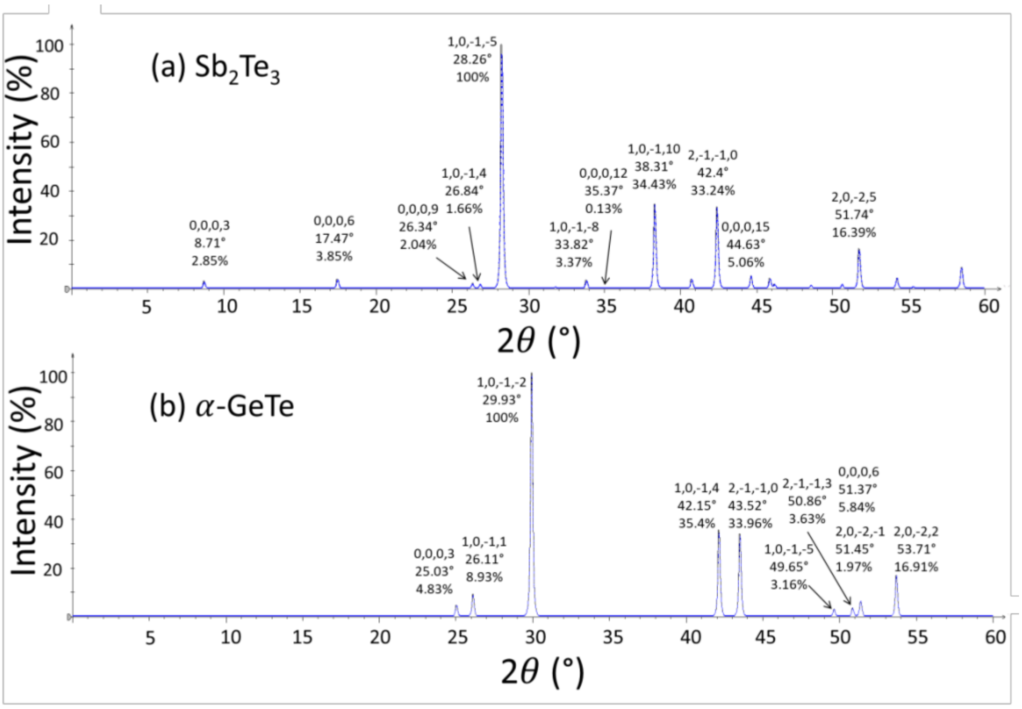

Fig. 3.4. Calculated x-ray diffraction profiles for (a) trigonal Sb_2Te_3 [121] and (b) low-temperature GeTe phase [127], both are represented in hexagonal lattice. Each annotation shows Miller indices, Bragg angle and relative intensity.

The origin of the lattice distortion in the low-temperature structure of GeTe (α-GeTe) has been discussed in the past [132], corresponding to Peierls instabilities [83] which concomitantly implies on the existence of two bonding subsets, three shorter covalent bonds (0.283 nm) and other three longer resonant bonds (0.315 nm) [117]. Upon temperature increase, the transformation into rock-salt structure occurs. It was long believed that the transition from distorted (ferroelectric) phase to undistorted (paraelectric) phase occurs by a *displacive* disappearance of Peierls distortion around Curie temperature, T_c (705 K), wherein the rhombohedral structure transforms towards a rock-salt structure, see Fig.3.3a. This result was based on the work by Chattopadhyay et al., [129] in which the bond lengths calculated from lattice cell measured mainly by neutron diffraction experiments. The displacive transition nature is confirmed by Raman scattering [133] measurement on the GeTe thin film, whose T_c is ~150K lower than that of bulk sample.

Comparing to bonding nature of stable crystalline phases of many other alloys within the quasi-binary line like Sb_2Te_3 or stable trigonal GST225 crystal, GeTe can be considered as three-dimensionally (3D) bonded material. This implies on an epitaxial growth mechanism, in which a conventional ‘lattice-match epitaxy’ occurs, where the incoming adatoms are bonded to the dangling bonds of the substrate. Therefore, the epitaxial quality profoundly depends on the degree of the lattice mismatch between film and substrate. It brings about some restrictions and issues which are encountered when growing epitaxial GeTe films on highly-mismatched substrate like Si, as discussed later in Section 5.3. It includes a relatively narrow epitaxial window and also a predominantly three-dimensional growth mode, implying on a high surface roughness of thin film [99, 138]. However, the use of Sb_2Te_3 as a seeding layer can improve the growth and resulting GeTe films quality (demonstrated in Section 5.3).

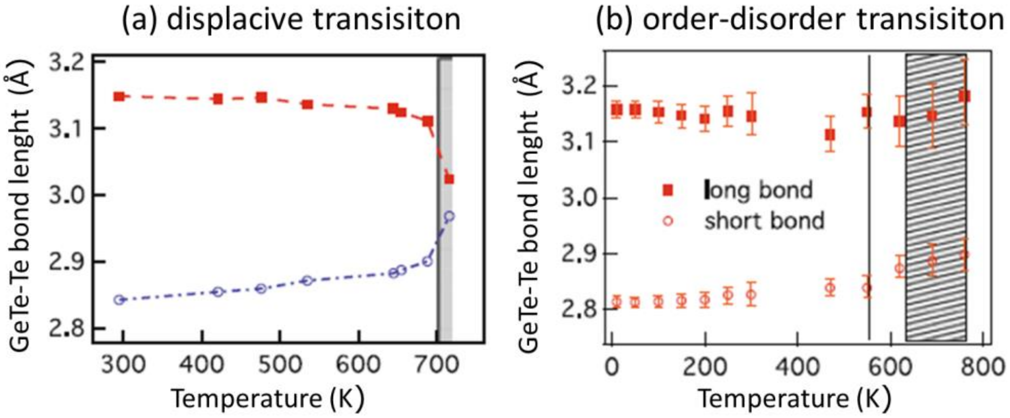

Fig. 3.5. (a) the Ge−Te bond lengths calculated from the neutron diffraction data, showing a convergence of two bond lengths near Curie temperature, T_c, suggesting the displacive nature of ferroelectric-to-paraelectric transition in bulk sample [117]. In (b) EXAFS measurement [134] is presented, showing that the local distortions are still present, except that it is stochastically randomized rendering the macroscopic ferroelectric-to-paraelectric transformation. The dashed area and the vertical line represent the Curie temperatures of bulk and thin film material [139], respectively(adapted from [117]).

Chapter IV
Experimental and theoretical details

4. 1. Thin film deposition process

Pulsed laser deposition (PLD) is the physical vapor deposition technique employed in the present work for a thin film formation. In PLD, a high-energy pulsed laser beam is employed. The beam with sufficient energy density is focused onto a surface of a material target of desired composition to ablate a small volume creating a plasma plume. The ablated material can absorb the laser energy forming highly energetic plasma. The plume consists of molecules, atoms, ions, electrons, clusters and particulates with relatively high kinetic energies in which the velocity (in vacuum) depends on target materials and laser properties being used.

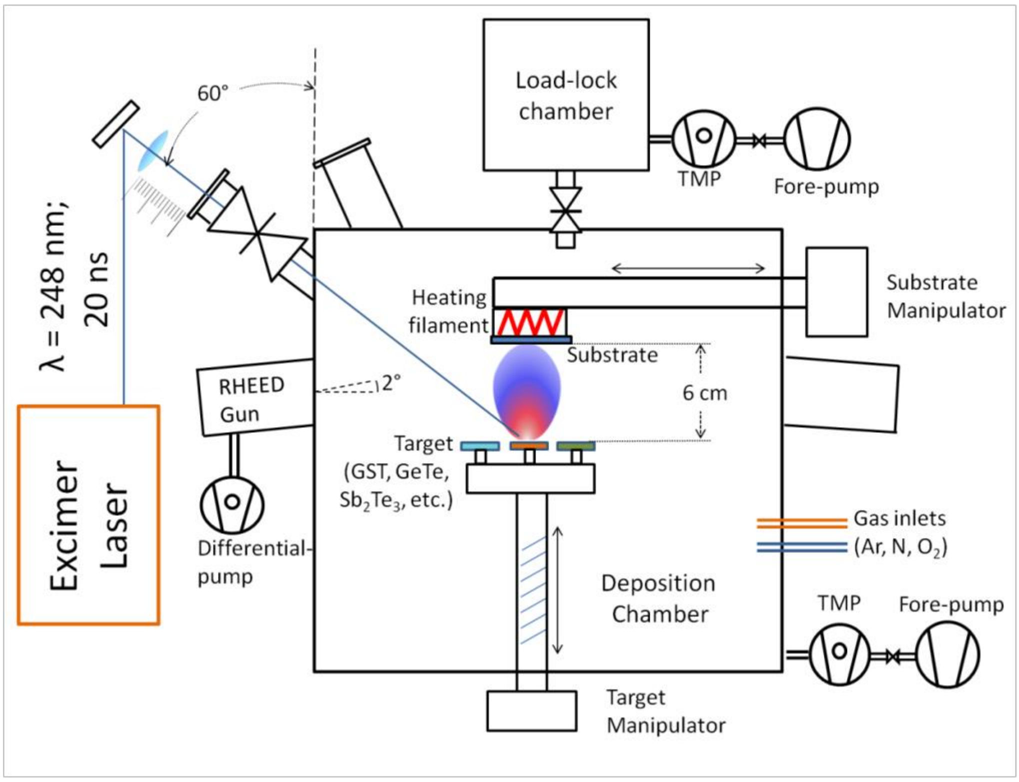

Fig. 4.1. Schematic of the PLD system routinely employed for depositions of GeTe-Sb_2Te_3 thin films and superlattices. The system consists of a load-lock and a deposition chamber. The blue line represents the laser (beam) line impinging on the target. Reflection high energy electron diffraction (RHEED) system is installed on the chamber. The vacuum is maintained using the turbomolecular pump (TMP).

The distribution of the number of material ablated from the target surface is symmetrically-peaked along the normal axis of the surface and falls-off as $(\cos\theta)^q$, where θ is an angle diverged from the normal axis and q usually ranges between $\sim 4-30$, [140, 141]. The fact that a plume with high energetic particles is yielded is a unique feature of PLD compared to other common deposition techniques like, e.g., molecular beam epitaxy (MBE). The plasma plume can be used to grow an epitaxial layer where the presence of energetic species is desirable in order to find its optimum configuration at the surface of the growing film typically required to form a high-quality crystalline (i.e. epitaxial) film. More important, PLD has proven particularly effective at producing epitaxial films of multi-component inorganic materials [141].

Fig. 4.1 shows a simplified schematic of the PLD system routinely employed in the present work. The system consists of two chambers. The load-lock chamber where loading and unloading of substrates take place, and the deposition chamber in which three ablation targets are mounted on a carousel-like manipulator. In this chamber, a low base pressure of $\sim 2 \times 10^{-8}$ mbar (ultra-high vacuum, UHV) is typically maintained.

One advantage of PLD is that the power (i.e. laser) source is situated outside the deposition chamber. This renders the deposition process relatively clean. Additionally, the process can occur either in UHV or in presence of a background gas, such as Ar, N_2, or O_2. In this work, for the deposition of chalcogenide epitaxial films and superlattices, a $\sim 5 \times 10^{-5}$ mbar Ar partial pressure is employed by introducing Ar gas. The use of this Ar background serves the purpose to moderate the kinetic energy of particles in the plasma plume. This is also a distinguishing feature of PLD compared to e.g. MBE of GST where a base pressure $<10^{-9}$ mbar is typically prerequisite [142]. PLD allows to deposit two or more materials successively, e.g. in deposition of superlattice structures, with or without changing the deposition conditions and without breaking the vacuum in between two successive depositions. For the ablation process, the laser beam is focused using a plano-convex lens (focal length of 800 mm) through a quartz window to irradiate the target material located inside the deposition chamber.

The KrF excimer laser (LPX Pro 240, Coherent) with a wavelength of 248 nm and a pulse duration of 20 ns is employed. The use of this short-pulsed laser duration is to lower down the thermal diffusion length of the material which is proportional to the root of laser pulse duration. This making sure a congruent ablation to occur hence allowing stoichiometry preservation during PLD [143]. Additionally, the number of laser pulses (N) and the laser repetition rate (f) being used for a deposition can be easily set, implying that the use of a pulsed laser beam also allows to precisely control deposition rate and layer thickness. The typical value of f being used for thin film and layer deposition in this work is 2 Hz, otherwise being mentioned. The use of 2 Hz is considered as optimum laser rate where high quality film can be produced without significantly extending the deposition rate.

The basic equation characterizing the electromagnetic field interaction with matter is described by

$$E = (2\Phi / c\varepsilon_0 n)^{1/2}, \tag{4.1}$$

where E is the electric field intensity inside the material (V/cm), Φ is the power density (W/cm^2), $\varepsilon_0 = 8.854 \times 10^{-12}\ \mathrm{F/m}$ and n is the refractive index. By taking, for example, n to be 1.5 and Φ to be $5 \times 10^8\,\mathrm{W/cm^2}$, it results in electric field intensity to be no less than $5 \times 10^5\,\mathrm{V/cm}$, which is sufficient for a dielectric breakdown as long as the power is above a threshold power density. Generally speaking, almost all kind of material classes can be employed as material target for PLD, from a broad range of oxides [144-148] and nitrides [149-151], biocompatible minerals [152, 153], polymers [154], to chalcogenides and dichalcogenides [155, 156].

In this work, the target materials were arc-melted $Ge_2Sb_2Te_5$, GeTe and Sb_2Te_3 targets. The chemical composition of each alloy was confirmed by means of energy dispersive x-ray (EDX) spectroscopy. Typically the alloys possess a relatively high absorption coefficient in ultra-violet (UV) region, e.g., that of $Ge_2Sb_2Te_5$ is in the order of $\sim 10^6\ \mathrm{cm^{-1}}$ [157], facilitating the stoichiometric transfer during ablation. Depositions of amorphous [158], poly-crystalline and epitaxial [98, 159] GST alloys have been recently performed by PLD.

The ablation from the target surface is arranged such that the incident laser impinges on the target at 60° with regard to the substrate normal and the ablated material is deposited on the substrate surface situated in the plasma plume. The material condenses on the substrate surface and forms a film. Substrate and ablation target are rotated during the process, in order to ensure a high homogeneity of the deposited film and to hinder damage of the target surface due to the laser irradiation, respectively. A resistive heater filament is employed to heat the substrate, see Fig. 4.1, which is located inside the substrate holder (directly behind the substrate). The maximum heating temperature is up to 1100 °C. A thermocouple of type C is used to monitor the actual substrate temperature, which was calibrated by another thermocouple (type C) attached to the substrate resulting in a temperature precision of $T_s \pm 30°$, where T_s is the nominal substrate temperature. For analytical means, a reflection high energy electron diffraction (RHEED) system is installed, see Fig. 4.1. RHEED allows to *in-situ* monitor the surface crystallinity and smoothness of layers during deposition. For further information about PLD, the reader is referred to standard textbooks, e.g. [141, 143].

Furthermore, the use of a composite target material also implies on the different physical deposition mechanism than that of any other deposition techniques, e.g. MBE. The investigation of this point in particular for PLD of GeSbTe materials, to the author knowledge, has not been done yet. However, other studies have been conducted, for example, by Houška *et al.*, [160] using laser desorption ionization time-of-flight mass spectrometry (LDI-TOF MS). In the experiments, a nitrogen laser ($\lambda = 337$ nm) was used for ablation. They identified the composition of clusters in the plasma plumes formed during laser desorption of some technologically important chalcogenide alloys, including GeTe, $Ge_2Sb_2Te_5$ and Sb_2Te_3. For LDI of GeTe alloy, it was found that the plasma contains Ge^+, Ge_2^+, $GeTe^+$, $GeTe_2^+$, $GeTeH^+$, Ge_2Te^+, $Ge_3H_{18}^+$ (or $Ge_3H_{17}^+$), $(GeTe)_2^+$, $GeTe_3^+$, $Ge_3Te_3Te_4^+$, a signal overlapping of $Ge_2Ge_5Te_5^+$ with $Ge_{14}Te^+$ and $Ge_9Te_4^+$ with $Ge_2Te_8^+$. For the ablation of $Ge_2Sb_2Te_5$, mass spectrometry revealed that the plasma plume consists of Ge^+, Ge_2^+, GeTe, Te_2^+, $GeTe_2^+$, overlapping of clusters ($SbTe_2$, Sb_2Te and Te_3), $GeSbTe_2^+$, and Sb_3Te^+, and low intensity $GeSbTe_3^+$ and $Sb_2Te_3^+$. For the ablation of Sb_2Te_3, the identified clusters are $TeSb^+$, $TeSb_2^+$ and $TeSb_3^+$. Singly and positively and/or negatively charged clusters, Sb_mH_n (e.g. Sb_2H_4, Sb_2H_6, Sb_2H_8, and Sb_4H_7) were also identified, together with low intensity Te_n (n =1–2) and Sb_n^+ (n = 1–3).

4.1.1. Thin film specimens

As mentioned in this thesis, three different alloys are used as the PLD targets (i.e. the compositions close to GST225, GeTe, Sb_2Te_3), from which the epitaxial thin films were deposited. The first material to deposit is GST225. For this alloy, two different groups of epitaxial films were prepared. In both groups, identical deposition parameters were used, i.e. the laser fluence (F) ~0.7 J/cm^2, the number of pulses (N) of 7200 and the repetition rate (f) of 2 Hz. However, in the depositions of the thin films of group 1, the target-substrate distance (d_{ts}) was larger (~7.5 cm) than that of group 2 (~6.0 cm). Each thin film in group 1 was deposited at different substrate temperature T_s, ranging from RT to 300 °C. All the thin films in group 2 were deposited at T_s = 220 °C. Just after each deposition of a film in group 2, the *ex-situ* annealing process was done by keeping the heater on at 220 °C. The annealing duration varies from 0 h to 7 h.

The second alloy is Sb_2Te_3 where the process parameters being used for the depositions of epitaxial films are d_{ts} = 6 cm, F = 0.8 J/cm^2, N = 7200 and f = 2 Hz. For both alloys, i.e. GST225 and Sb_2Te_3, the substrate temperature T_s is varied for each deposition, varying between RT and 320 °C.

The third material to deposit is GeTe. Two groups of thin film specimens were deposited. To the first group belong epitaxial GeTe films on Si(111) in which the deposition parameters being used are d_{ts} = 6 cm, F = ~1.1 J/cm^2, N = 4000 and f = 2 Hz. T_s was varied between RT and 300 °C. The second group consists of GeTe films deposited on a Sb_2Te_3-seeding layer formed on a Si(111) substrate. Deposition of the Sb_2Te_3-seeding layer was done at 240°C with the number of pulses of 500 and with identical other PLD process parameters as aforementioned, resulting in a ~4 nm-thick van der Waals epitaxy layer of trigonal Sb_2Te_3 [123]. The substrate with the seeding layer was then cooled down to T_s (230, 210, 150 and 145 °C) for the subsequent GeTe depositions. The process parameters for the GeTe deposition were all identical to those of films deposited directly on Si(111), i.e. the first group.

For the deposition of GeTe-Sb_2Te_3 superlattices (SLs), Sb_2Te_3 was first deposited at 240 °C with N = 400. The deposition of Sb_2Te_3 as the first layer serves as a seeding layer. Subsequently, the temperature was reduced to the deposition temperature T_s. T_s varied for each deposition of SL structure from 120 °C to 220 °C. After the temperature reached the deposition temperature, T_s, and being stable, the depositions of alternating GeTe (N = 400) and Sb_2Te_3 (N = 400) were done. In all

Sb_2Te_3 and GeTe depositions, F = 0.8 J/cm^2 and f = of 2 Hz were used. The total number of layers to be deposited constructing the SL structure are 14 layers, consisting of alternating (seven) GeTe and (seven) Sb_2Te_3 layers. In other words, each superlattice structure consists of seven repetitions of Sb_2Te_3-GeTe unit layers. Additionally, another thin film with only one Sb_2Te_3-GeTe repetition unit was prepared. The thin film was prepared by deposition of Sb_2Te_3 on Si(111) followed by the deposition of GeTe. Both Sb_2Te_3 and GeTe depositions were done using parameters of N = 1000; f = 2 Hz; F = 0.8 J/cm^2.

For all of the abovementioned specimens (thin films and SLs), after the final deposition finished, the substrate cooled down naturally to RT. Then, a capping layer of amorphous $LaAlO_x$ (~8-10 nm thick) was deposited onto each film and superlattice structure in order to minimize any possible chemical contamination and oxidation during storage in ambient conditions.

4.1.2. Substrate preparation

As stated in Section 2.3, the substrates for the depositions of thin films and superlattices are (111)-oriented Si. All the Si substrates (diced to 1×1 cm^2 pieces) used for epitaxial thin film growth must be cleaned from impurities in order to promote epitaxial growth to occur. Hence several steps of cleaning process were done. Firstly, each Si substrate has undergone a Radio Corporation of America (RCA) standard cleaning set [161]. The substrate was first cleaned from organic impurities and also particles using base-peroxide solution: ammonium hydroxide (NH_4OH), hydrogen peroxide (H_2O_2), and H_2O in the mixture ratio of 1:1:5. Subsequently, the second cleaning step was done using a solution of 1 part HCl, 1 part H_2O_2 and 6 parts H_2O. This step is done to remove any ionic contaminants which can be left after the first step cleaning process is done. Also, this step is to passivate Si surface from any further contaminations during storage in ambient environment. Each first and second cleaning step was done in ultrasonic cleaner for 20-30 min (~60 °C). Just before being used for epitaxial growth, the substrate was etched using hydrofluoric acid (7:1 vol. ratio of 40% NH4F in H_2O and 49% HF in H_2O) for 30 s. This etching step is essential to remove the thin native oxide layer on top of the substrate. After etching, the substrate was rinsed in deionized water and stored in the water before loading it into the deposition chamber for deposition.

4. 2. Thin film characterization techniques

In this subsection, some techniques routinely used for thin characterizations are discussed. The techniques include x-ray diffraction (XRD), reflection high energy electron diffraction (RHEED), scanning transmission electron microcopy (STEM), atomic force microscopy (AFM) and scanning electron microscopy (SEM).

4.2.1. X-ray diffraction (XRD)

The main thin-film-characterization methods being utilized in the present work are based on the diffraction of x-rays or electrons. The x-rays are generated in an x-ray tube by 40 keV electron irradiation of a metallic anode. Energetic electrons generated by the high voltage directly move toward and then collide with the target anode material, of which copper is used here. Two kinds of spectra are generated. (i) a continuous spectrum originating from the deceleration of the moving charged electron, so-termed *Bremsstrahlung* and (ii) the characteristic spectrum, the spectrum typically used in diffractometer for crystal structure characterization. This spectrum sharply peaks at very specific wavelength, i.e. the peaks are typically 0.0001 nm wide [162]. The Cu K_α line lies at ~0.15418 nm while Cu K_β lies at ~0.13922 nm. The Cu K_α line is typically used for x-ray structural crystal analysis, mainly due to its pronounced intensity at a specific wavelength and the existence of corresponding optics.

W.H. Bragg and L. Bragg were the first to express the diffraction condition to a two-dimensional crystal grating, so-termed Bragg's law $n\lambda = 2d_{hkl}\sin\theta$, or simply

$$\lambda = 2d\sin\theta, \qquad (4.2)$$

where d_{hkl} is the corresponding plane spacing of the crystal and θ is the angle between the incident ray and the surface, $n = 1, 2, 3$, etc. is the order of diffraction and $d = d_{hkl}/n$. The diffraction only occurs whenever the Bragg's condition is fulfilled. Only particular values of θ, of which the two or more diffracted rays are in phase, i.e., the phase difference ϕ is 0 or $n2\pi$, hence reinforce to each other producing a diffracted intensity by constructive interference. For the incidence directions on which Bragg's law is not satisfied, there is no diffraction observed since the scattered rays eliminate one another. For an observable diffraction, θ must geometrically be $<$ 90°, so that $\sin\theta < 1$ resulting in $\lambda < 2d$. By considering that a crystal has typically atomic spacing distance d in the order of ~0.3 nm, the wavelength cannot exceed a specific value (~0.6 nm) noting the versatility of x-ray as well as of accelerated electrons in transmission electron microscopy (TEM, 100 keV or 0.0037 nm or lower), rather than larger wavelengths like with UV light.

The diffraction condition can be more easily visualized by a construction of the so-termed *Ewald sphere* in reciprocal space (RS). First, the reciprocal lattice of the crystal of interest must be built. The vectors of incoming ray $\mathbf{S_0}$ and scattered ray $\mathbf{S}$ both with the magnitude of $2\pi/\lambda$ points out the origin of the reciprocal lattice and the scattering vector $\mathbf{q}$ is $\mathbf{S}-\mathbf{S_0}$. An Ewald sphere can be constructed with the center of the origin of the vector and the vector to be the sphere's radius. Diffraction can occur (i.e. Bragg's condition is fulfilled) when the sphere intersects a reciprocal lattice point. It means that vector $\mathbf{q}$ agrees with a reciprocal lattice vector, $\mathbf{g}_{hkl}$, corresponding to lattice plane (hkl) and Bragg's formula becomes $\mathbf{S} - \mathbf{S_0} = \mathbf{g}_{hkl}$. By rotating the Ewald sphere around the origin, one can find any other possible diffraction for a given wavelength. In other words, the constructed Ewald sphere represents all the possible diffraction of the wavelength λ and particular lattice form and size. The specific λ used in an x-ray diffractometer fixes the radius of Ewald sphere to a constant value. For x-rays, the radius is $\sim 10\ \mathrm{nm}^{-1}$ compared to reciprocal lattice spacing of crystal in the order of $\sim 5\ \mathrm{nm}^{-1}$. For a moving electron, the de Broglie wavelength (λ_e; in Å) is given by

$$\lambda_e = \sqrt{\frac{150.4}{E_e}} \quad , \tag{4.3}$$

where E_e is the kinetic energy of the electron (in eV). Accordingly, the Ewald radius of the accelerated electrons in TEM of $\sim 1690\ \mathrm{nm}^{-1}$ $(E_e = 100\ \mathrm{keV})$ or that in RHEED of $\sim 880\ \mathrm{nm}^{-1}$ $(E_e = 30\ \mathrm{keV})$. This means that, in the case of electron diffractions e.g. in TEM, the Ewald sphere becomes a surface of a sphere cutting through points in RS.

4.2.2. X-ray diffraction techniques

One of the main advantages of XRD analysis is that the measurement is typically done by averaging over a large area/volume of the specimen, i.e. with irradiation areas of diamaters ϕ ranging from 10 μm up to 50 mm [163]. Hence, the crystallinity and film properties, e.g. epitaxial relationship between film and substrate or film thickness, can be assessed as an average. In this work, a Rikagu Ultima IV Type 3 diffractometer with parallel beam geometry was routinely used for XRD and x-ray reflectivity (XRR) experiments. An incident beam which is monochromatized (i.e. for the characteristic CuK_α line) and well-collimated is very crucial especially for structural investigation on epitaxial or single crystalline films including in-plane measurements and pole figures. For doing so, x-ray optics are employed. A graded parabolic multilayer mirror (PMM) is attached adjacent to the x-ray source, taking a role as a collimator of the divergent beam coming from the tube; hence, the parallel beam geometry is utilized, see Fig. 4.2.2, adapted from [164, 165]. It results in a parallel beam with a vertical divergence of ~0.05°. Adjacent to the PMM is the Soller slit consisting of long metal plates arranged parallel to the diffractometer circle in order to parallelize the beam horizontally. The use of the Solar slit with a smaller value of divergence angle provides a higher resolution yet at the expense of intensity loss. The optimum values of both are sought for each specific routine. The height-limiting incident slit defines how large the irradiated sample surface area is according to $W = W_{slit}/\sin\omega$, where W is the projected length on the sample surface W_{slit} is the slit opening and ω is the angle of the incident beam with respect to the surface. In addition to the use of the PMM, the presence of CuK_β is further suppressed by the use of additional means. In this work a graphite monochromator attached in the diffracted beam line are used. Another advantage of using the secondary monochromator in the diffracted beam is to minimize background radiation from the specimen being measured.

In addition to the conventional four goniometer axes (three for rotating sample: ω, χ and ϕ and one for rotating detector: 2θ) the diffractometer is featured with an *in-plane arm* which provides an additional 5th goniometer axis, i.e. in-plane $2\theta_\chi$ axis, see Fig. 4.2. This feature provides more flexibility especially in measuring x-ray diffraction of vertical planes (planes normal to the film surface) as well as inclined planes. Utilizing this feature, then the thin film sample can be placed horizontally for the whole measurement eliminating the risk of sample position shifts due to problems with sample clamping or heating during measurements.

The diffraction condition is the basis for all x-ray diffraction experiments: once Bragg's condition is fulfilled, geometrical position of sample and/or x-ray source−detector could be altered to perform different types of measurements in order to obtain various kinds of information about the crystalline structure. Some measurements procedures which are routinely performed in this work include:

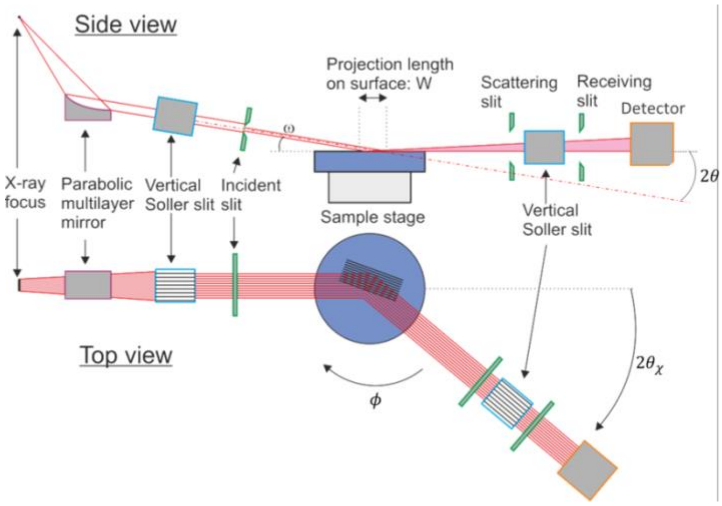

Fig. 4.2. The optics used in the diffractometer. In-plane axis featured by the diffractometer giving a flexibily for performing especially in-plane diffraction measurements.

1. The symmetrical $2\theta - \omega$ scan to qualitatively and quantitatively assess the crystal structure. The measurement is done by symmetrically varying the incident angle ω and at the same time the 2θ angle. The value of 2θ is kept twice as large as ω in the whole measurement. It is equal to changing the length of scattering vector $\mathbf{q}$ while maintaining the direction fixed. This measurement is done to provide information on the crystal orientation and out-of-plane inter-planar spacing for planes parallel to the film's surface.

2. To assess the out-of-plane tilt distribution of crystallites, a *rocking curve* (or ω scan) is performed. By keeping the positions of incident beam (ω) and detector (2θ) fixed (keeping the length of scattering vector $\mathbf{q}$ constant) in the expected Bragg's angle of planes of interest (in this case, planes parallel to the surface of the film) and then rocking the film around the Bragg angle. The full-width at half-maximum (FWHM) of the acquired peak is a measure of the mosaic crystallite distribution.

3. *Pole figure* measurements were performed for a texture analysis of oriented polycrystalline and epitaxial films. From such measurements the, e.g., epitaxial relationships between layer and substrate, i.e. the arrangement of the

crystallite lattice with respect to the lattice of the single crystalline substrate can be determined. The term *in-plane pole figure* is often used since the in-plane detector arm is employed in the diffractometer for the pole figure measurement.

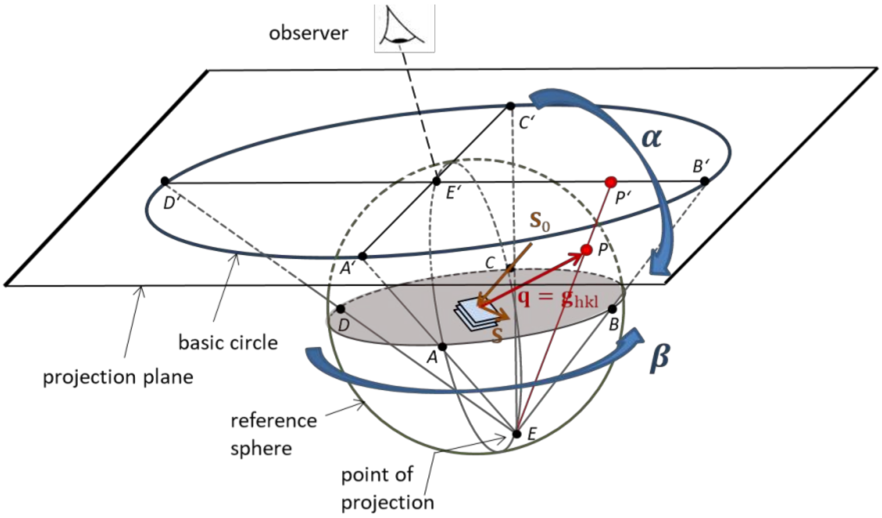

Fig. 4.3. Schematic of pole figure measurement. The reference sphere is coincident with the trajectory of the end of scattering vector. The $\mathbf{S}_0$, $\mathbf{S}$ and $\mathbf{q}$ vectors are coplanar. Only the set of (hkl) planes of interest is shown which is titled to the sample surface parallel to circle ABCD, and with the pole P on reference sphere. P is projected onto the pole density maximum *P’* on the pole figure in the projection plane (adapted from [162]).

The schematic of the measurement is specifically depicted by Fig. 4.3. The reference sphere is defined with a radius of the fixed-length scattering vector $\mathbf{q}$. First, the source and detector are kept in Bragg’s angle of a plane of interest, $2\theta_B$, while placing the scattering plane (a plane containing $\mathbf{S}_0$, $\mathbf{S}$, and $\mathbf{q}$) coincident with the plane perpendicular to the film surface, e.g. the circular plane AECE’. This scattering vector point iteratively tracks a polar angle α from 0° (corresponding to a pole on E’) to 90° (a pole in the equator, i.e. circle ABCD). For each α-step, β-scan (azimuthal count ϕ-rotation from 0° to 360°) is performed. In this present work, the α-step is typically set to be 1° and β-scan is done with step of 0.5°. The primary and secondary Soller slits are set to be 0.5°. The resulting pole on the reference sphere is then projected onto the projected plane which is tangent to the reference sphere and parallel to the thin film surface. The result of the projection is so-termed a pole figure. The diffracted intensity is plotted as a function of α and β corresponding to its stereographic projection imaged on the projection plane. Hence, the polar angles α and β are considered as functions of the four axes $2\theta_\chi, \phi, 2\theta$ and ω. The obtained pole figure data is angularly conserved but areally distorted.

4. To determine the film thickness, an x-ray reflectivity (XRR) measurement is performed. In XRR, the $\theta/2\theta$ operation mode is used with a small incident angle (ω) around the critical angle, θ_c (i.e. typically is ~0.3°). Below θ_c total external reflection occurs. The density of the film can be

determined using the abrupt decrease of the reflected intensity just above θ_c. At incident angle above θ_c the beam penetrates into the specimen and the presence of surface and interface of materials (e.g. film and substrate) with different reflective indices (i.e. difference in electron densities) gives rise to reflections from surface and interfaces forming interference fringes on the reflected rays. This interference is angle (ω)-dependent. The period of the fringes can be used to determine the film thickness using the relation

$$\begin{aligned} d &\approx \frac{\lambda}{2} \frac{1}{\sqrt{\theta_{m+1}^2 - \theta_c^2} - \sqrt{\theta_m^2 - \theta_c^2}} \\ &\approx \frac{\lambda}{2} \frac{1}{\theta_{m+1} - \theta_m}, \qquad \text{for } \theta_m \gg \theta_c \end{aligned} \tag{4.4}$$

where θ_m and θ_{m+1} are angular positions of m^{th} and $(m+1)^{\text{th}}$ intensity maxima, respectively. The amplitude is used to assess the surface or interface roughness and electron density difference between materials. The data analysis is done using RayfleX software [166].

4.2.3. Reflection high energy electron diffraction (RHEED)

Reflection high energy electron diffraction (RHEED) is an essential technique to *in-situ* monitor the surface crystallinity, orientation, reconstruction and smoothness of the growing thin film. A schematic of the RHEED technique is shown in Fig. 4.4. The electron beam is incident at a glancing angle to the surface of the film. Then, the diffracted beam is detected by the fluorescence screen on the other side of the chamber across the sample. A glancing incident angle is used in order to make sure that only the surface with a few atomic layers beneath the surface of the grown layer contribute to the diffraction of the accelerated electrons.

Thus, using a glancing incident angle leads to small penetration depth and therefore to a small information depth. The sampled volume can be regarded as a two-dimensional (2D) crystal grating. In this case, the reciprocal lattice points become elongated forming infinitely-long reciprocal lattice rods, i.e. so-termed crystal truncation rods, which are perpendicular to the surface being investigated. The fact that the accelerated electron beam in RHEED has a relatively small wavelength leads to a construction of an Ewald sphere with a comparably large radius, see Sec. 4.1.

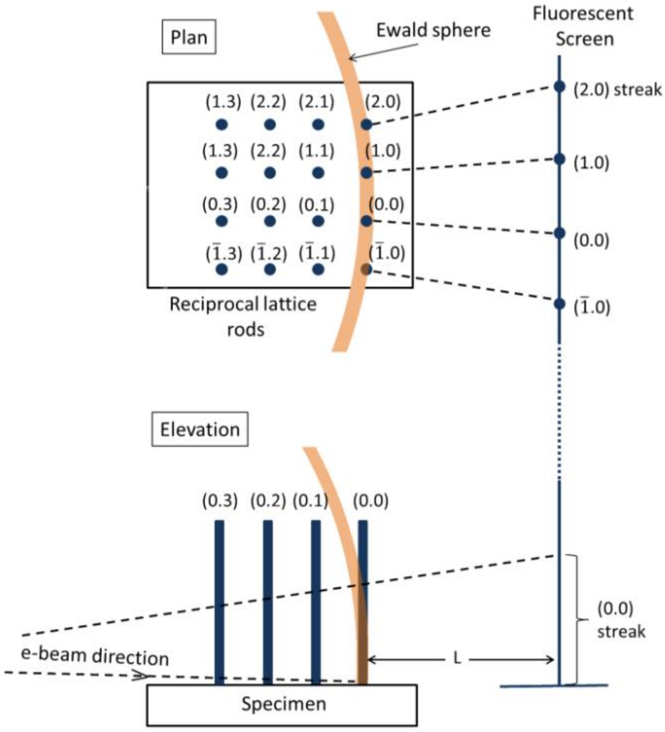

Fig. 4.4. Schematic of RHEED using Ewald sphere construction. The sampled volume can be regarded as 2D atomic grating, bring about reciprocal lattice rods. These rods intercept with relatively-large-radius Ewald sphere, creating streaky intensity on the screen. The upper image depicts the formation of RHEED streaky patterns in plan and elevation point of views. Adapted from [167].

In the ideal case that a single electron wavelength is used incident on a perfectly smooth single crystal, the Ewald sphere cuts the rods in specific points which is visible on the screen where the intensity spots are located on a circle, the so-termed Laue circle. However, the divergence in energy and direction of a real electron beam, accompanied by an imperfect surface of a real surface imply that the Ewald sphere coincides with sections of the rods forming streaky patterns on the fluorescent screen. Kikuchi lines can be present indicating a well oriented crystalline structure. When the film is morphologically rough, the usual streaky diffraction pattern becomes a point (or transmission)-like pattern since the reciprocal lattice rods are then replaced by reciprocal lattice points itself of the rough crystalline surface. These *in-situ* RHEED measurements were, in this work, performed at an electron acceleration voltage of 20 to 30 kV and at a small electron beam incidence angle of about 2° with respect to the sample surface. The azimuthal electron beam incidence was along the surface of Si substrate in Si$\langle 1\bar{1}0\rangle$ directions. More detailed information about RHEED can be found in standard text books, e.g. [168].

4.2.4. Transmission electron microscopy (TEM)

Electron beams can be transmitted through a thin specimen (lamella) in order to image the nanostructure of the material [169]. In a conventional transmission electron microscope (TEM) system, the vertical acceleration and the focusing geometry of the electron probe are modulated by means of electro-magnetic fields as the optical lens. The lenses located in front of the specimen are the condenser lenses, mainly to modulate the focus of electron beam probing onto the specimen; whereas the lenses located after the specimen are the imaging lenses, as seen in Fig. 4.5, showing thin-lens ray diagram of a simplified imaging system with incident electron beams parallel to the optical axis.

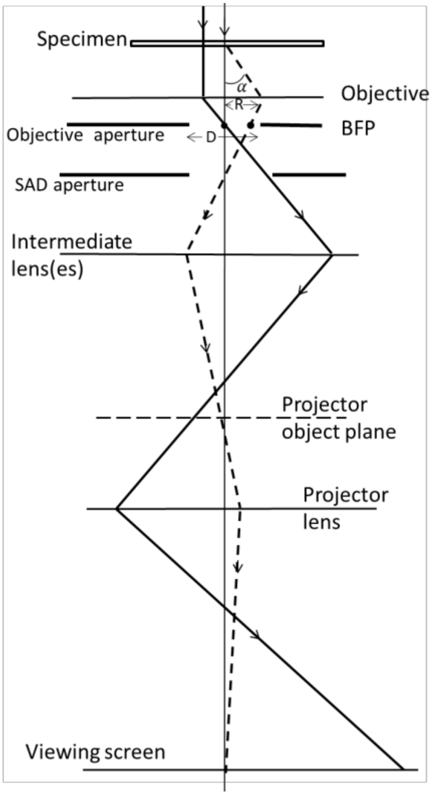

Fig. 4.5. Simplified imaging system of TEM schemed with thin lens-ray diagram. Two different rays are pictured: deflected (dashed line) and un-deflected (solid) rays by the specimen, both forming the diffraction contrast in TEM image.

The beam transmitted through the specimen without deflection (solid line) is deflected by the objective and crosses the axis at the back-focal plane (BFP) with the distance of focal length, f, of the objective. The deflected beam (dashed line) tracks different route. The deflections are mainly due to coherent elastic (Coulomb) interactions of the electron with atomic nucleus in the specimen. The electron deflected by the atom(s) in the specimen with a deflection angle more than semi-angle α would be absorbed by the diaphragm at the BFP. Setting α to be small, most of the electrons diffracted by the specimen are absorbed by the diaphragm and do not contribute to the final image (the region appears dark), resulting in a *diffraction contrast* in the bright-field (BF) image. Contrariwise, a dark-field (DF) image is produced by selecting the diffracted beam by horizontally displacing the objective aperture off the axis, resulting in the image with opposite contrast to that of bright-field image.

In scanning TEM (STEM), the electron is focused to probe the specimen with a beam diameter can be as small as ~0.2 nm, while scanning the probe in a raster mode to make an image with single-atom resolution producible. The annular dark-field (ADF) detector is employed in STEM and located just behind the specimen. It collects the scattered electrons at a certain angular range ($\theta_{\text{min}} - \theta_{\text{max}}$). The advantage is that the resulting image is more directly-interpretable in terms of atomic mass, due to its scattering contrast feature insensitivity to objective-lens focus. The intensity of elastic scattering of electrons, e.g. in STEM image contrast, is roughly proportional to Z^2, in which a high-angular signal is usually detected making STEM atomic number contrast.

As mentioned, a good quality thin specimen (lamella) with is prerequisite in order to produce a high quality TEM image. First, a Pt layer was deposited on top of the film in order to protect the film from high current Ga^+ and/or Ar^+ beams during FIB cutting and thinning process [170]. To prepare a lamella, the thin film sample is cut using Ga^+ ion beam at 30 kV [170]. The second preliminary thinning process was carried out using 5 kV at low angle of 0.5 – 1.5°. By repeating the step with the low current, a cross-section lamella with a thickness of ~100 μm could result. The final thinning process was done using Ar^+ ion beam with angle of 10° at the beam voltage of 900 eV and 500 eV, consecutively, for about 30 min at both sides of the lamella. As measured by electron energy loss spectroscopy (EELS), the final lamellae in this work typically possess thicknesses of around 40 nm.

In this thesis, high-resolution STEM investigations (HRSTEM) were carried out on a probe C_S-corrected Titan^3 G2 60-300 microscope operating at 300 kV accelerating voltage. The aberration correction allows the electron probes to be focused helping to improve the spatial resolution the system. A probe forming aperture of 25 mrad was used in the experiments. All STEM images were acquired with a high-angle annular dark-field (HAADF) detector using annular ranges of 64–200 mrad, thus fulfilling well the Z-contrast imaging mode. The super cells for diffraction and Bragg reflections simulations were built up with CrystalMakerX as well as CaRIne Crystallography [173] software.

4.2.5. Atomic force microscopy (AFM)

Detailed quantitative information on the surface topography of the deposited thin films was obtained by AFM measurement in intermittent contact mode (or Tapping Mode AFM [174]). The AFM system consists of several main elements: a small Si cantilever with a sharp tip (nominal tip radius of 7 nm), a laser beam and a position-sensitive photodiode detector, as well as a tip-z-position feedback controller system. The cantilever, hence the tip, is oscillated in z-direction by a driving external force at a resonance frequency (nominal 300 kHz). When the oscillating tip is brought to close proximity to the sample surface (see Fig. 4.6), the level of the damping in oscillation amplitude would be inversely proportional to the distance between both the tip and surface due to tip-surface interaction.

By varying the tip-surface distance and keeping the oscillation amplitude constant without changing the oscillation-driving force, the height information is collected by recording the force of tapping contacts to maintain the set amplitude (and frequency). The height profile of certain (x-y) positions on the sample is controlled by the help of a laser beam focused on and reflected by the upper side of the cantilever which then is recorded by the four-segment photodiode. The oscillation and height of the cantilever are controlled by the feedback system so that the sharp tip is *not* all the time touching the surface being observed (by which the surface can be damaged as in the contact mode), instead it is only "tapping" the sample surface. Therefore, the tapping mode provides the more pronounced tip-surface interaction and hence allows a better measurement in atmospheric pressure environment compared to that of the non-contact mode. The topographical image is recorded by (x-y) scanning (in raster pattern) of the oscillating cantilever tip. The roughness of the surface of the thin film is assessed by calculating the root mean squared roughness (RMS), which is done by averaging the measured z-values for all *n* measured (x-y)-points.

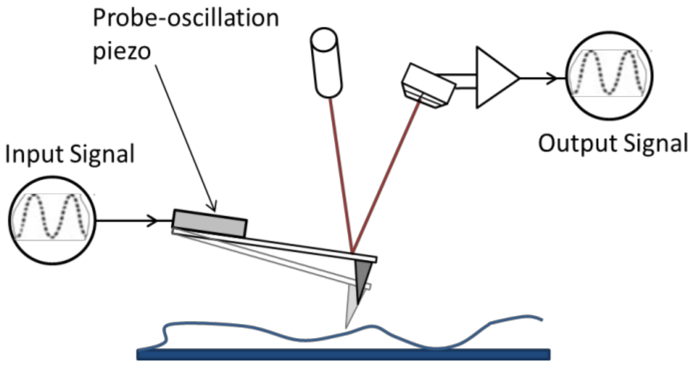

Fig. 4.6. Schematic of the oscillating AFM mode. The comparison between oscillation input and output gives the force acting on the probe, which is used to determine the height profile [175].

4.2.6. Scanning electron microscopy (SEM) and energy dispersive x-ray (EDX) spectroscopy

Complementary to AFM, the surface and cross-sections of the films were imaged by means of a scanning electron microscope (SEM). Provided that an accelerated electron beam is focused on the specimen surface, a SEM image can be generated by exploiting the electron beam−material interaction. A focused primary electron (PE) beam with certain kinetic energy, i.e. in this present work typically of 5 to 25 keV, probing to a specimen (typical probe diameter of 0.4 to 5 nm) would have various interactions with atoms in different depths from the surface, resulting in various signals each of which is collected by a dedicated detector. The signal commonly used for imaging is the low energy (starting from < 100 eV) secondary electron (SE) signal, i.e. atomic electrons of a region close to the surface which are emitted by *inelastic* excitations or collisions with PEs. In fact, the formation of SEs is by gaining only a small energy from collisions; those very close to the surface (*escape depth* of < 2 nm) [169] are released out from the surface and detected by the SE detector.

The SEM image of three-dimensional appearance results from different number of SE collected by the detector for each specific beam position. A different topological steepness of the surface is due to a different sampled volume for each angle of incidence with regard to each inclination of the surface. The more inclined a surface a larger escape SE region results, corresponding to brightness contrast in the image. In a deeper region, back-scattered electrons (BSEs) can be generated. BSE, possessing higher energy than that of SE, is a PE which is back-scattered (*elastically* scattered) by atomic nuclei. Characteristic x-rays can be generated in an even deeper region when the beam with enough energy (in this work 15 and 25 keV are usually used with aperture of 60 μm and sample titling angle of 45°) excite inner-shell electrons leaving vacancies which are subsequently occupied by outer-shell electrons by emitting x-rays.

The generated x-rays spectrum can be collected by an energy dispersive detector for an elemental analysis. They are characteristic for each atomic number, Z. This concept is employed in energy dispersive x-ray spectroscopy (EDX). Additionally, BSE can also be utilized for chemical analysis, since the BSE intensity is highly dependent on Z^2 of the sample material. In SEM, only focusing lenses, i.e. usually consisting of condenser lenses and an objective lens, are needed: there are no imaging lenses as in TEM. Instead, the magnification is a result of a ratio between the geometrical sizes of the raster scan on the specimen surface with that of the raster at the displaying screen: the smaller the raster size on the surface, the higher the resulting magnification.

Surface topographical and cross-sectional images, in this work, were obtained by a Carl Zeiss Ultra 55 field emission SEM equipped with a GEMINI electron column. The system features two available secondary electron detectors, i.e. an Everhart-Thornley detector and an in-lens detector. Quantax 400-EDX, Bruker Nano GmbH, is attached to the SEM system for chemical composition analysis. The EDX analysis is done using Bruker ESPRIT software.

Chapter V
Epitaxial chalcogenide thin films

As stated, the ultimate goal of the thesis is to fabricate epitaxial chalcogenide superlattice structures by means of PLD. The main 'material ingredients' of the structures would be three of the most stable alloys within the binary line GeTe-Sb_2Te_3, namely $Ge_2Sb_2Te_5$ (GST225), Sb_2Te_3 and GeTe. Therefore, a deep investigation on epitaxial growth of each alloy using PLD is pre-requisite in order to obtain a preliminary knowledge of each material growth characteristic. This chapter consists of three sections, each of which focuses on the depositions and characterizations of epitaxial GST225 (first material), Sb_2Te_3 (second material) and GeTe (third material) thin films, respectively (see Chap. 4.1.1).

5.1. $Ge_2Sb_2Te_5$ (GST225)

The first deposited material is GST225. Owing to its optimum properties, the alloy is considered as the prototypical phase change alloy for application in memory media. Hence, the investigation of the alloy is slightly more extensive than that of the other alloys (i.e. GeTe and Sb_2Te_3).

As explained in the experimental section (see Chapter 4, Section 4.1), two groups of thin GST films were prepared. There is no difference in all the process parameters being used for preparing thin film specimens in group 1 and 2, except that of different target-substrate distance being used. Thin films of Group 1 were prepared with target-substrate distance of ~7.5 cm while that of group 2 is ~6 cm (the detailed information about the deposition parameters see Section 4.1).

Accordingly, the present section is divided into two subsections. *The first part* (Subsection 5.1.1), hence dealing with the first set of thin films (group 1), discusses mainly about the epitaxial window of GST on Si(111) substrate and the influence of the process parameters on the thin film properties.

Secondly, as previously explained, one of the most interesting and technologically relevant features of GST alloys is its polymorphic phases. By means of XRD and STEM measurement, as will be seen in Subsection 5.1.2, the reduction of the target-substrate distance is confirmed to dramatically alter the resulting epitaxial film properties, especially in terms of crystal quality, crystalline phases constituting the epitaxial films as well as epitaxial relationships between the films and substrate. This allows one to more deeply explore the phase transformation by the *ex-situ* annealing process. Motivated by the importance for an investigation on pulsed laser deposited GST crystalline structures on Si substrate, the second set of thin films (Group 2) were prepared and are discussed in *the second part* (Subsection

5.1.2). Subsection 5.1.2 mainly deals with a deeper investigation on the growth mechanism of the film and the influence of annealing process on the film's properties.

5.1.1. Epitaxial window and influence of process parameter

5.1.1.1. Film thickness and crystallinity

The thickness value of the deposited GST films of group 1 as determined by XRR was constant (~130 nm) for the films deposited at RT to 100 °C. The thicknesses gradually decreased to around 10 nm for films deposited at 300 °C. Fig. 5.1 shows XRR data of two exemplary films deposited at 170 °C (black curve) and 250 °C (red curve), with the thicknesses of 64 and 24 nm, respectively. As characterized by Eq. 4.4, a thicker film (deposited at lower temperature, 170 °C) shows the interference fringes of XRR with a larger oscillation period compared to that of the thinner film (deposited at higher temperature, 250 °C). This thickness reduction was caused by thermal desorption of species during the laser ablation process. Hence, the upper end of the growth window suitable for crystalline growth of GST on Si(111) was determined to be near 300 °C.

As mentioned, the laser beam induced deposition of the GST films was carried out at substrate temperatures T_s between RT and 300 °C. The structure of the grown GST225 thin film was studied by XRD. The results are shown in Fig. 5.2. For substrate temperatures $T_s < 100$ °C, no Bragg peaks of GST are visible, i.e. only films with amorphous phase were obtained. Starting from T_s = 110 °C films grew crystallized in the trigonal GST phase and were (0001) oriented. This is an unexpected finding, since the lowest crystallization temperature in the $Ge_2Sb_2Te_5$ system is at least 30 K higher and the typical crystallization temperature of the stable trigonal GST structure is 247 °C [100]. A further increase of the substrate temperature resulted in more pronounced diffraction peaks of the $Ge_2Sb_2Te_5$ phase as marked by the P1 arrows in Fig. 5.2. The peaks situated at around 36° and 39° are weak intensity contributions from the Si substrate.

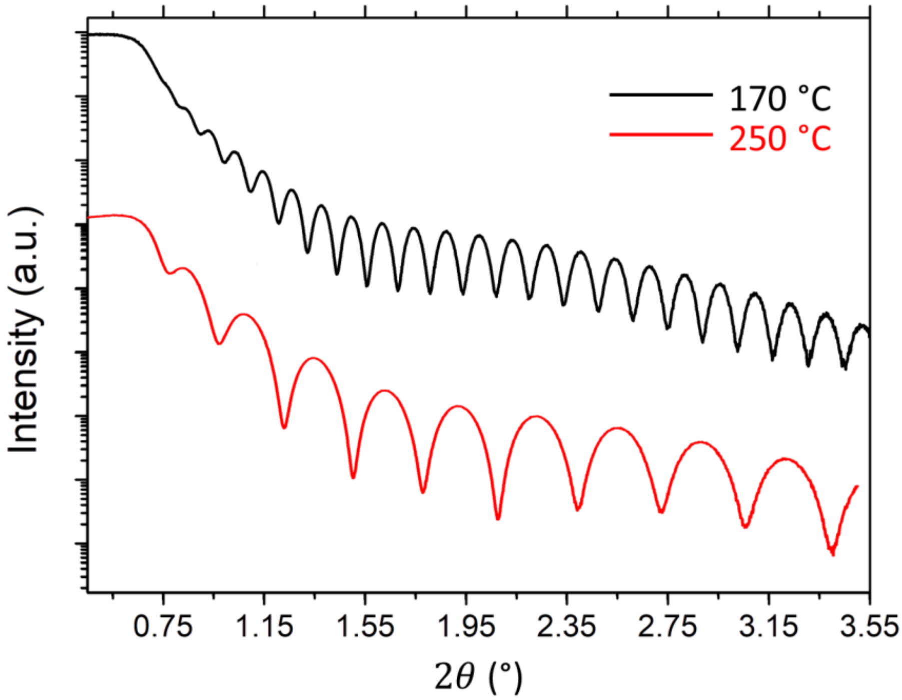

Fig. 5.1. X-ray reflectivity (XRR) measurements of GST thin films deposited at 170 °C (black) and 250 °C (red).

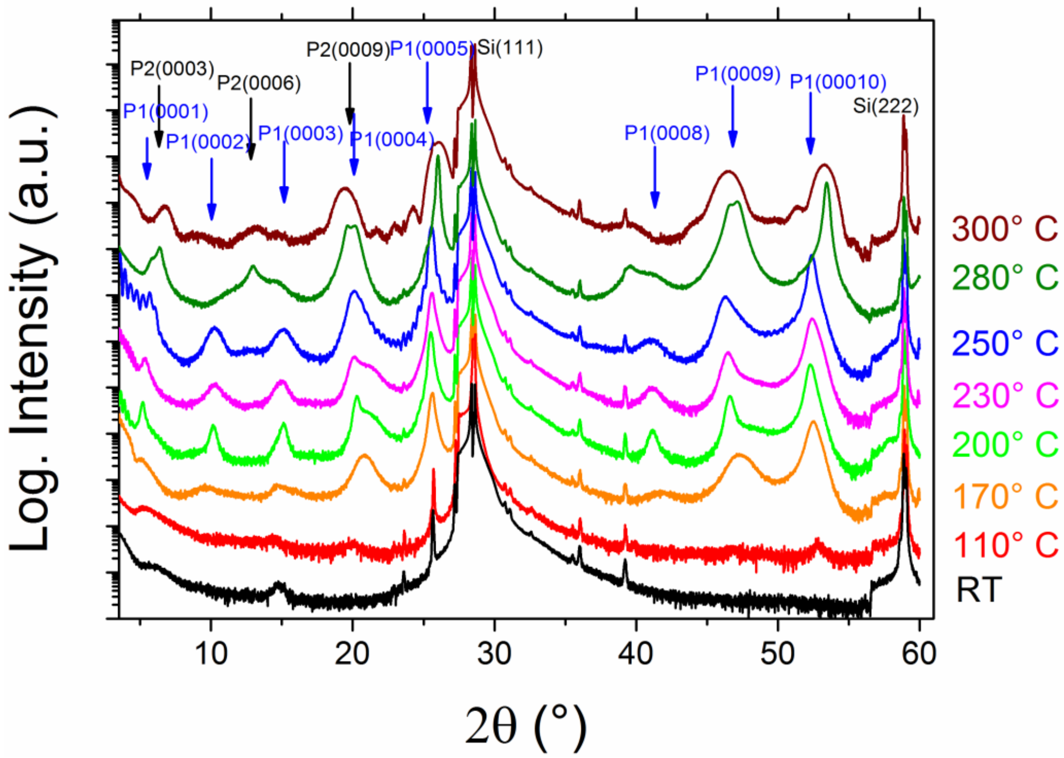

Fig. 5.2. $2\theta - \omega$ XRD scans of the films deposited at different substrate temperatures. All intensity data are plotted in logarithmic scale. The annotations P1 and P2 refer to trigonal phase of $Ge_2Sb_2Te_5$ and to $Ge_1Sb_2Te_4$ phase, respectively. The substrate peaks are marked with Si notation.

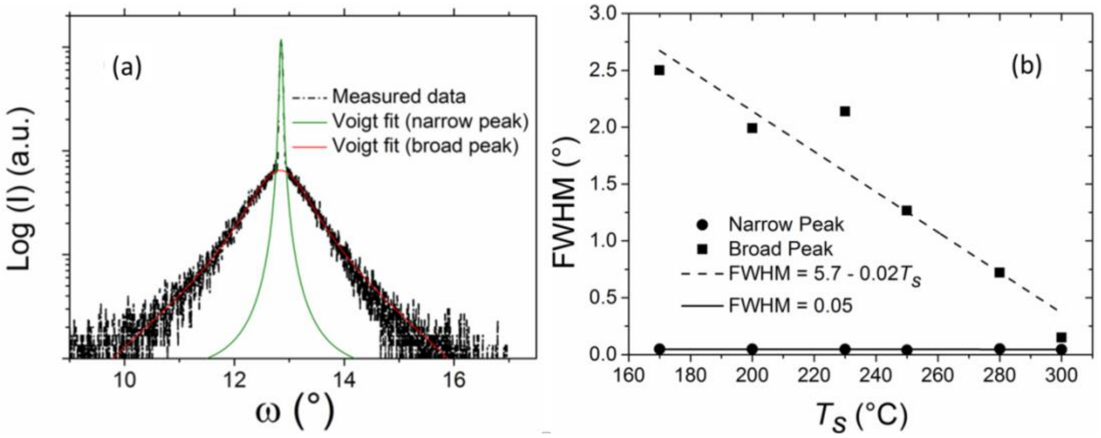

Fig. 5.3. XRD rocking curve of the GST(0005) reflection of the film deposited at T_s = 250 °C in a logarithmic scale. Corresponding GST(0005) rocking curve FWHM of the GST films deposited at different substrate temperatures.

Above 250 °C, some Bragg peaks corresponding to the second crystalline phase, the GST124 phase, can be discerned which are annotated by P2. A similar shift of the chemical composition has been observed by Thelander et al. [97] and is related to thermal desorption effects. Throughout the whole temperature range only (000l) peaks can be seen in Fig. 5.2. which means that the films grow according to GST(0001)||Si(111). At temperatures $T_s \geq 250$ °C Laue fringes are visible in a 2θ region between 22° and 27°, which are an indication of high crystalline quality and high thickness homogeneity of the films.

The tilt distribution of the crystallites within the films was investigated by XRD rocking curve (RC) measurements at the example using the GST(0005) reflection. To make it easier to discern these two different XRD RC contributions, the exemplary rocking curve (deposited at T_s = 250 °C) is plotted in logarithmic scale and shown in Fig. 5.3a. The rocking curve exhibits two different peaks, i.e. broad and narrow peaks, both peaks share the same center position. The measured data was fitted with pseudo-Voigt profile curves and the corresponding FWHM values are reported in Fig. 5.3b. The FWHM of the narrow peak is constant around 0.05° for all substrate temperatures within the measurement precision, while those of the broader peaks decrease linearly with the increase of substrate temperature from around 2.5° for T_s = 170 °C to 0.15° for T_s = 300 °C. The narrow peak is assumed to belong to the GST films. In other words, the contribution of the substrate can be excluded, since the Si(111) reflection is relatively far away (around 2.8° in 2θ) from the GST(0005) reflection. The probable explanation for the occurrence of these double rocking curve peaks is the growth of much more ordered layers adjacent to the substrate surface, while the outer layers tend to form crystallites with deviated orientations from the out of plane of the substrate. This is also supported by the FWHM value of the broad peak, which saturates to a value of 0.06° for films deposited at T_s = 300 °C, at which a not completely coalesced epitaxial layer of ~10 nm thickness was obtained.

Another possible explanation is associated with the difference of crystallite size among the films. The FWHM of the GST(0005) Bragg peak is measured to be 0.37° for the film deposited at 170 °C films, whereas it is only 0.18° for 280 °C film. Due to the smaller crystallites of the films deposited at lower temperature, the amount of grain boundaries is larger which leads to broadening and weakening of the rocking curve. The last possible explanation is the presence of mixed crystalline phases, i.e. rock-salt and trigonal phases.

According to the calculated x-ray diffraction profile [100], the trigonal GST(0005) reflection is situated at $2\theta = 25.85°$,which is close to the cubic GST(111) reflection ($2\theta = 25.59°$). Both planes, GST(0001) and GST(111), are known as equivalent planes in the GST25 crystal, and a transformation of cubic GST in (111) orientation into (0001) oriented trigonal GST phase was reported by Bragaglia *et al.* [176].

5.1.1.2. Film topography

The topographies of the GST films as well as of the Si substrates were recorded by AFM (Fig. 5.4). The bare Si(111) substrate after annealing at 250 °C for 1 h exhibits a surface with a root mean square (RMS) roughness of 0.32 nm (not shown here). The topographies of films grown at 200 °C and 250 °C are depicted in Fig. 5.4a and b, respectively. The surface remains comparably smooth (see Fig. 5.4a and b). A triangular shape of the GST crystallites can be identified (see Fig. 5.4b). At 300 °C (Fig. 5.4c), the film thickness is ~10 nm, showing crystallites with a triangular shape and additionally the beginning of film coalescence.

It has to be noted that the triangularly shaped crystallites are pointing out to different distinct directions, indicating an epitaxial relationship between film and substrate as well as the presence of rotation twins. The RMS roughness value of the film is 2.5 nm. Fig. 5.4d also shows a topography which is characterized by triangular features for the film deposited with a higher laser repetition frequency of 10 Hz at T_s of 250 °C. The films also exhibit the typical triangular feature of crystallites, however, the RMS roughness value is higher (RMS = 1.6 nm) than that of the films deposited at the same T_s but with lower laser frequency (2 Hz, Fig. 5.4b). In general, the surface roughness values of pulsed laser deposited epitaxial films are smaller than those of MBE deposited GST films on Si(111) [99], which are typically as high as 5.8 nm, because of large crystallites protruding out of the surface.

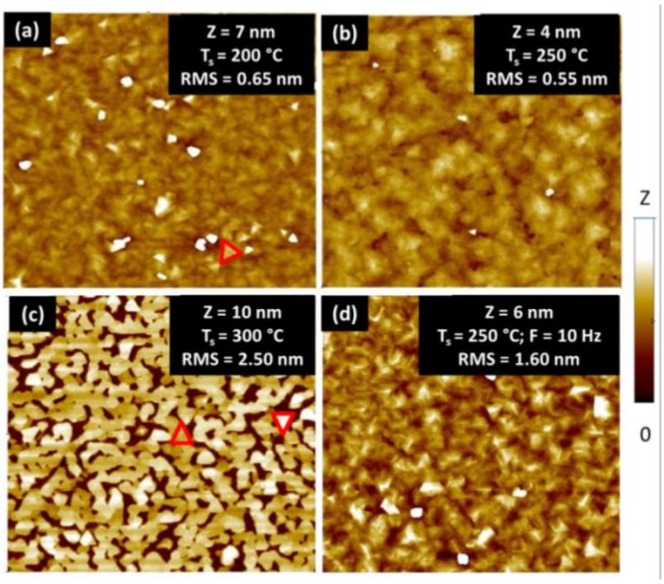

Fig. 5.4. AFM images of GST films grown with a pulse repetition (frequency) of 2 Hz at (a) T_s = 200 °C, (b) T_s = 250 °C, (c) T_s = 300 °C, and (d) with laser pulse repetition frequency of 10 Hz at T_s = 250 °C. All images have the same lateral scale of 2 × 2 μm^2.

5.1.1.3. Texture analysis

To prove the epitaxial growth as well as the presence of crystallites which are rotated with respect to each other in the films, in-plane pole figure measurements using the trigonal GST$\{10\bar{1}3\}$ reflection at 2θ = 28.91° were performed, as shown in Fig. 5.5. Between T_s = 110 °C and 170 °C, the GST films are polycrystalline with a preferred orientation parallel to the GST(0001) plane as depicted in Fig. 5.5a above. The film deposited at 170 °C, as shown in Fig. 5.5a, exhibits six pole density maxima at a polar angle $\alpha \approx 57°$, each separated azimuthally by 60°, which is superimposed by a low-intensity ring connecting every two pole density maxima, indicating a polycrystalline fiber texture contribution.

Pole density maxima at $\alpha \approx 70°$ originate from the Si(111) reflection with 2θ = 28.44°. Exemplarily, one of the pole density maxima of the substrate is marked by a red arrow, whereas the exemplarily pole density maximum pointed at by the green arrow shows a contribution from the sample holder. At higher substrate temperatures, starting from 200 °C (Fig. 5.5b), single crystal films could be grown. The six (i.e. two times three) maxima represent the presence of two stable orientations of the GST crystallites which are rotated by 180° with respect to each other around the c-axis (rotational domains). Such rotational domains were also demonstrated in a previous study [97], and found in MBE-grown epitaxial films [138]. At the lower temperatures, all six maxima have equal intensities, whereas at temperatures of 230 °C and higher (Fig. 5.5c and d), one crystal orientation starts to become more preferred than the other. The intensity ratio of 2:1 shows that the PLD process is suitable for a high quality epitaxial growth of GST films. The out-of-plane and in-plane epitaxial relationships are GST(0001)||Si(111) and GST$[2\bar{1}\bar{1}0]$||Si$[1\bar{1}0]$, respectively.

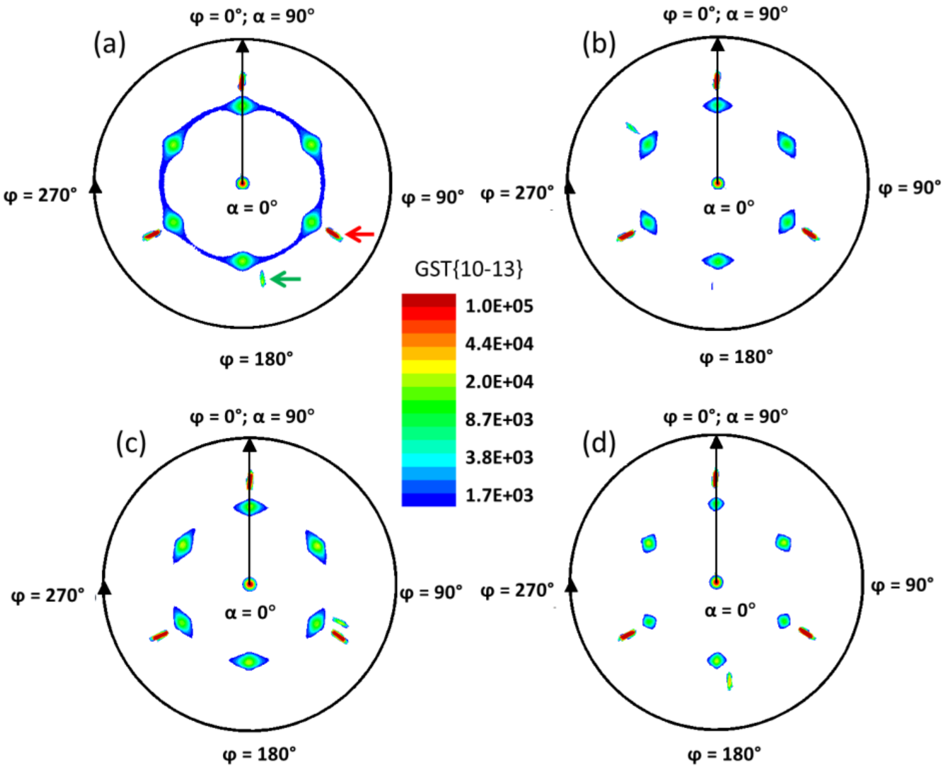

Fig. 5.5. In-plane GST{$10\bar{1}3$} pole figures of the films deposited at (a) T_s = 170 °C, (b) 200 °C, (c) 230 °C, and (d) 250 °C (α is the polar angle, φ is the azimuthal angle).

5.1.1.4. Influence of laser frequency

As mentioned above, PLD generally offers higher deposition rates without any complications in the process. In order to explore this opportunity, a set of GST films was prepared using different laser repetition frequencies ranging from 2 to 100 Hz, while the other deposition parameters were kept constant as explained in the experimental conditions section. All the films show the already described duality of the XRD RC peaks, too, i.e. a narrow (constant around 0.06°) and a broader peak.

The broad RC FWHM of each film is summarized in Fig. 5.6. The FWHM is almost constant around 1.2° until laser beam frequency of 50 Hz (deposition rate of 42nm/min), above it ascends steeply to around 5.5° for the film deposited with a laser frequency of 100 Hz. The epitaxial nature of these films was checked by in-plane pole figure measurements (not shown), in which the pole density maxima are relatively unchanged for laser frequencies of up to 50 Hz, whereas at 100 Hz the film was characterized as textured polycrystalline. These observations show that PLD can be used to grow epitaxial GST films with a relatively high deposition rate, while the epitaxial nature of the films can be maintained.

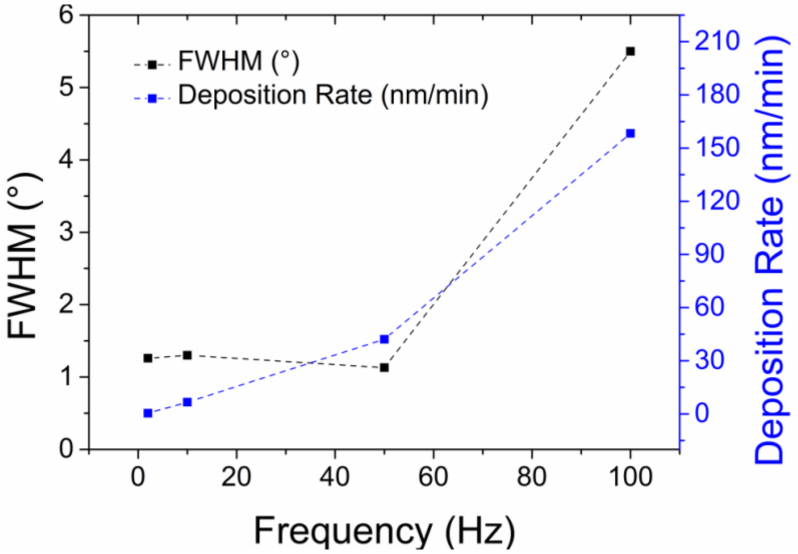

Fig. 5.6. XRD rocking curve FWHM of the GST(0005) reflection (black curve) and deposition rate (blue curve) of films deposited with different laser pulse repetition frequencies ranging from 2 to 100 Hz.

5.1.2. *In-situ* investigation on the growth of GST thin film, influence of annealing and inspection on local structures

In this subsection, the growth mechanism of GST on Si(111) will be discussed. As mentioned, the GST thin films were prepared with identical parameters as were in Subsection 5.1.1, except that the target-substrate distance has been reduced from ~7.5 cm to ~6 cm (group 2, see Chap. 4.1). By this reduction, RHEED system can be routinely employed for *in-situ* monitoring of surface crystallinity and smoothness. Subsequently, the general pictures about crystalline structures owing to GST are comprehensively explored especially by means of STEM.

5.1.2.1. *In-situ* investigation on thin film growth

As mentioned, RHEED is used for *in-situ* investigating the surface properties of the substrate and the grown layer. Fig. 5.7a shows a RHEED pattern of the initial non-reconstructed Si(111) surface with the incident electron beam oriented along the Si$\langle 1\bar{1}0 \rangle$ direction. Streaky reflections along with Kikuchi lines are visible, confirming the highly crystalline and smooth surface topography of the Si substrate. It is ideal for epitaxial growth of GST225 thin films. A smooth transition from Si to GST225 reflections can be discerned in Fig. 5.7b in which diffraction patterns of both the Si substrate and the initial GST225 layer are apparently merged together, surrounded by a diffuse intensity distribution. The image in Fig. 5.7b was taken 60 s after deposition was started, corresponding to a nominal film thickness of 2.5 nm. The GST225-related reflections are marked by red arrows.

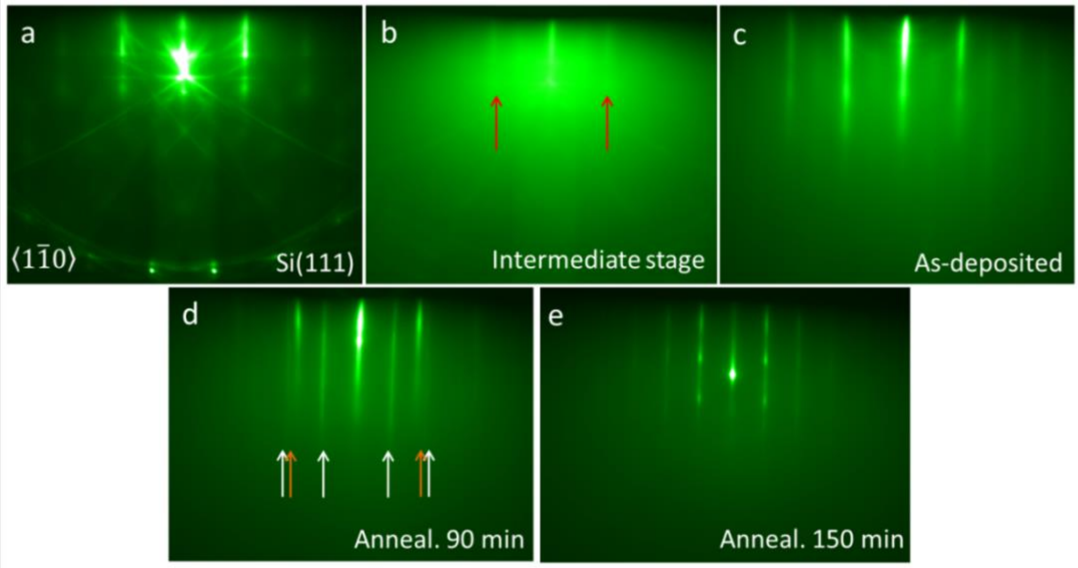

Fig. 5.7. RHEED patterns (electron beam was parallel to 110 direction of the Si(111) substrate) of (a) unreconstructed Si(111), and of an exemplary GST film, (b) at the beginning of GST growth, (c) right after deposition, and (d) after annealing for 90 min and (e) for 150 min. The GST film was grown and subsequently annealed at Ts = 220 °C.

The diffuse intensity points out that small (2D) crystallites nucleated at the beginning of the layer deposition. As the GST225 growth proceeded (around 7.5 nm nominal film thickness, 3 min), the diffuse intensity disappeared, while the streaky patterns became more pronounced. The pattern is identical to RHEED pattern of the final stage (as-grown) GST225 film, as presented in Fig. 5.7c. This indicates a high crystallinity of the as-deposited GST225 thin film with a smooth surface topography. Accordingly, it can be concluded that by means of PLD using the aforementioned deposition parameters the epitaxial GST225 grew on Si(111) according to the Frank–van der Merwe growth mode [177]. To our knowledge, there is not yet a report about this growth mode of epitaxial GST225 on Si(111) deposited by means of PLD. Upon the post-growth annealing process (Fig. 5.7d), additional streaky reflections (marked by white arrows) emerged in the RHEED patterns. This is an indication of either a surface reconstruction on the GST225 films caused by heat treatment or due to a phase transition during annealing. Interestingly, for the film annealed for longer time (150 min, Fig. 5.7e), the additional streaky reflections appearing in Fig. 1d are still present, while the second order reflections (marked by orange arrows in Fig. 5.7c), mainly present in the as-deposited film, disappeared. This is a hint that the film has undergone a crystal structure transformation after the longer annealing process. The patterns with streaky reflections found for the as-deposited films started to turn into transmission-like patterns with rather spot-like reflections, which might indicate surface roughening. The annealing process at T_s promotes surface reconstruction followed by a surface roughening.

5.1.2.2. Film topography

The GST225 film surface topography was characterized by ex-situ AFM. From the AFM image of the as-deposited GST225 thin film (Fig. 5.8a), it can be discerned that the film contains plate-like and elongated rod-like grains. The rod-like grains are rotated by 60° with respect to each other in such a way that they altogether construct triangular structures. The latter direct to three opposite crystal directions. Examples of these triangular structures are marked by red triangles in Fig. 5.8a. This grain arrangement indicates the presence of grain rotations within the film. The grain sizes roughly measured from the rods range from 150 to 300 nm in length and several tens of nanometers in diameter.

The root mean square (RMS) roughness of the whole AFM image is 1.3 nm. Upon the annealing process, a surface smoothening was induced to some extent, as seen in Fig. 5.8b, for the film which was annealed for 30 min. The RMS roughness of this film is 1 nm. This surface smoothing is due to surface atom desorption promoted by annealing. Triangularly and hexagonally formed holes started to form upon the further annealing process (annealed for 45 min, Fig. 5.8c). These holes have a typical depth ranging from 7 nm to 17 nm, which might be the manifestations of grain boundaries between two or more adjacent grains. Further film annealing, up to 7 h (Fig. 5.8d), results again in surface roughening with the RMS roughness being 1.3 nm.

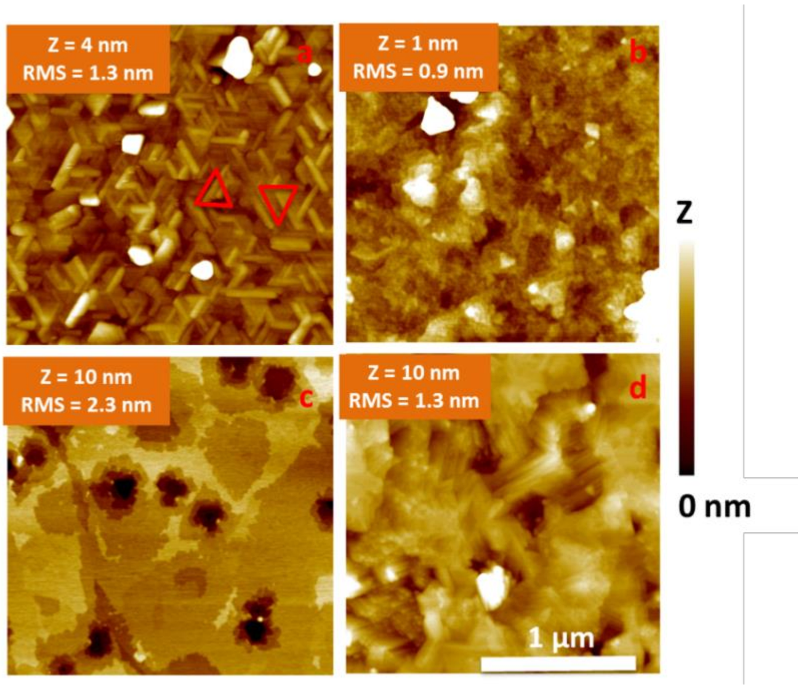

Fig. 5.8. AFM images of (a) an as-deposited GST film grown at substrate temperature T_s = 220 °C and the films annealed at T_s for (b) 30 min, (c) 45 min and (d) 7 h.

5.1.2.3. Crystalline structure and texture analysis

The crystal structure information of the GST225 thin films prepared by PLD was obtained by performing symmetrical $2\theta - \omega$ XRD scans in a wide angular region (Fig. 5.9). The black and blue annotations refer to t-GST225 and c-GST225 Bragg reflections, respectively, whereas Si(111) substrate contributions are denoted by red arrows. It can be derived from Fig. 5.9 that for both as-deposited and annealed GST225 thin films, the Bragg peaks coincide with the calculated (000l) reflections of the t-GST225 phase [100, 173]. This indicates that the GST225 films grew on the Si(111) substrate with t-GST225(000*l*) orientation. The latter is typical for epitaxial GST films deposited on Si(111) by PLD as previously reported [178]. In the as-deposited thin film, a closer inspection of the GST225(0005) reflection reveals that there are actually two contiguous peaks situated at 2θ = 25.65° and 25.92°. These angular positions of the two peaks coincide well with the calculated (111) reflection of c-GST225 (25.61°) and the (0005) reflection of t-GST225 (25.82°), respectively. It also applies to other higher order peaks, i.e. 2θ = 52.58° and 53.27°, which both are in good agreement with the calculated c-GST225(222) (52.62°) and the t-GST(00010) (53.08°) Bragg reflections, respectively [100, 173]. This specifies that both c-GST225 and t-GST225 coexist in the as-deposited film grown at T_s = 220 °C using PLD. The peaks corresponding to c-GST225(111) and (222) disappeared in the film annealed for 30 min, whereas only those corresponding to the t-GST225 phase are still present.

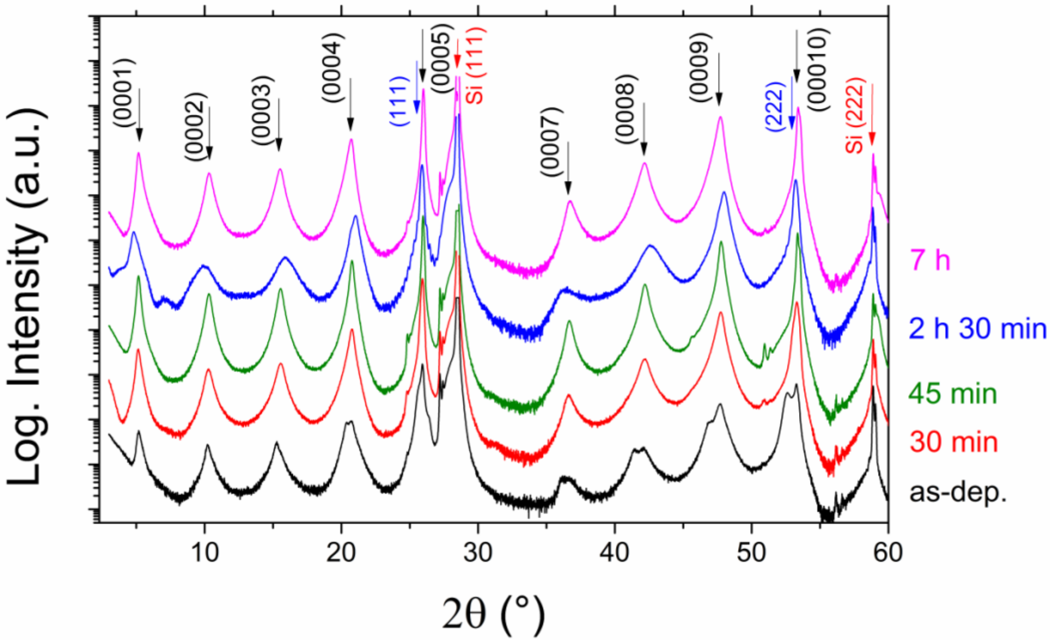

Fig. 5.9. 2θ-ω scans of the as-deposited film and of the films annealed at Ts = 220 °C for various time periods. Black and blue annotations refer to trigonal (0001)- and cubic (111)-oriented GST225 reflections, while the red ones denote Si substrate reflections.

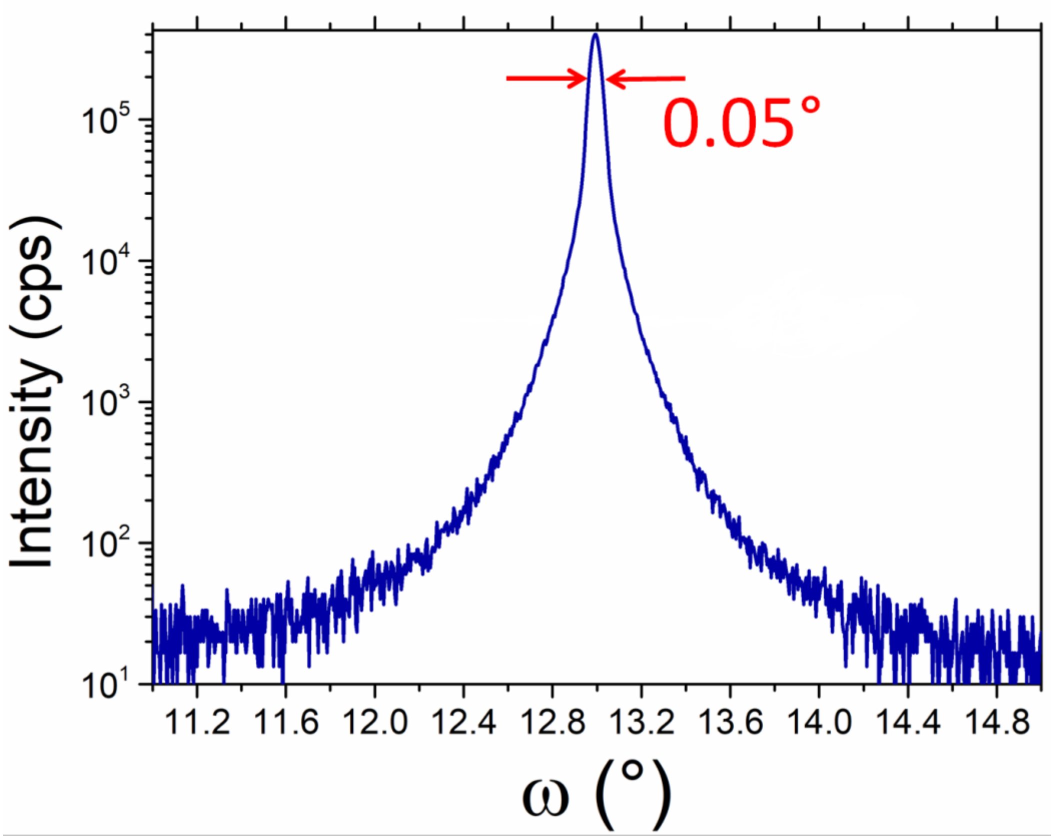

Fig. 5.10. Rocking curve of the GST(0005) reflection of the film (of Group 2) annealed for 45 min. The rocking curve consists of only a narrow peak with corresponding FWHM of ~0.05° confirming a good out-of-plane mosaicity.

The growth of c-GST225 in (111) orientation is due to the fact that the closed-packed c-GST225(111) planes are crystallographically equivalent to the t-GST225(0005) planes. In addition, other studies showed a favorable growth orientation in accordance with the six-fold symmetry substrate orientation from c-GST225(111) into t-GST225(0001) for annealed films that were deposited by MBE [176]. For the film annealed for 30 min, the GST225(0005) Bragg peak intensity increased significantly, i.e. it is one order of magnitude higher than for the as-deposited film. The annealed GST225 thin film (with a 142 nm thickness) possesses a comparable thickness to the as-deposited film (149 nm), as determined from XRR. This implies that a phase transformation from c-GST225 to t-GST225 took place during annealing of the films, so that the amount of t-GST225 phase in the thin films became much more pronounced.

The measurements of out-of-plane XRD rocking curves of as-deposited film using (0005) reflection results in the typical double peaks (as discussed in Section 5.1.1 and shown in Fig. 5.3) with the narrow peak's full width half maximum (FWHM) is ~0.06° and the broad peak is ~0.67° (not shown). The FWHM value of the broad peak is remarkably smaller than that of the film of group 1 as-deposited at even slightly higher temperature (230°), i.e. more than 2° (see Fig. 5.3). This concludes that the reduction of target-substrate distance improves the crystalline quality of the resulting film. The rocking curve of each annealed film consists of only narrow peak with FWHM of ~0.67°, as seen in Fig. 5.10, showing the rocking curve of the exemplary film annealed for 45 min. As was in Fig. 5.3, the logarithmic plot is used in order to confirm that there is no additional broad peak present.

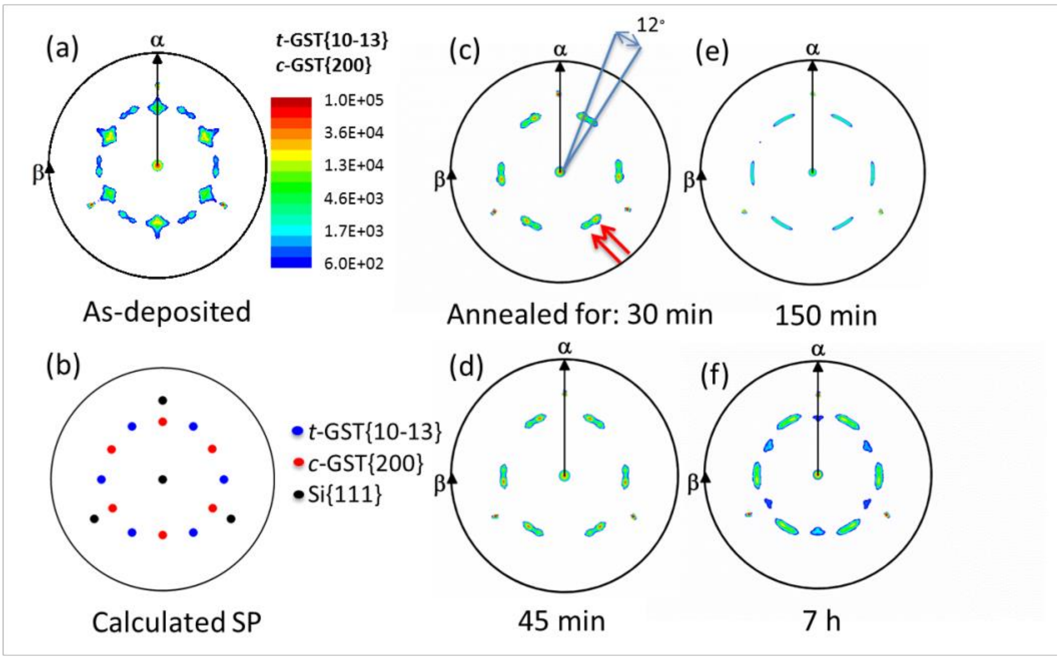

Fig. 5.11. In-plane pole figures of (a) an as-deposited GST225 film and (b) calculated stereographic projection of the model t-GST225$\{10\bar{1}3\}$ and c-GST225{200} [35], as well as Si [54] reflections. From (a) and (b) it is indicated that the as-deposited film consists of multiple phases, i.e. c-GST225 and t-GST225. (c–f) Epitaxial GST225 films annealed for different time periods at 220 °C. All films show only reflections from t-GST225, while c-GST225 reflections disappeared. The existence of two pole density maxima in every expected spot indicates that, in addition to a 180° rotation, the t-GST225 grains are also rotated by an angle around 12° to each other.

The epitaxial relationships of the produced GST225 thin films to the substrate were explored by measuring of in-plane XRD pole figures by using the t-GST225$\{10\bar{1}3\}$ reflection situated at 2θ =28.91°. Fig. 5.11a and b show the in-plane pole figure of the as-deposited film as well as the calculated stereographic projection from the structure model, respectively. The as-deposited film (Fig. 5.11a) exhibits three sets of pole density maxima. Each pole density maximum fits to the calculated stereographic projections (Fig. 5.11b) of Si(111), c-GST225(200) and t-GST225$(10\bar{1}3)$, which are respectively plotted with black, red and blue dots. Since in the 2θ-ω XRD scans, the Si(111), c-GST225(200) and t-GST225$(10\bar{1}3)$ Bragg peaks are contiguous, the presence of three sets of pole density maxima is inevitable. Accordingly, Fig. 5.11a points out that the as-deposited film contains both the c-GST225 and t-GST225 phases. For both crystalline phases, six, i.e. two times three, pole density maxima are observed. This means that in both c-GST225 and t-GST225, the crystallites are out-of-plane rotated by 180° with respect to each other. This indicates the presence of twin domains in the GST225 thin film. In the as-deposited c-GST225 thin film, one of the two crystallite orientations is dominating over the other one.

The intensity ratio of c-GST225 pole density maxima between these two maxima was calculated to be 3:1. In contrast, the pole density maxima intensities of the t-GST225 phase for all the films are evenly distributed between the two twin crystallite orientations. Upon the annealing process, the pole density maxima for the c-GST225 phase preferably disappeared, while the t-GST225 pole density maxima are still present as depicted in Fig. 5.11c–f. This shows that the films have undergone a phase transformation from cubic to trigonal phase during the annealing process, as was also noticed from the disappearance of the c-GST225 Bragg peaks in the $2\theta - \omega$ XRD scans of the annealed samples (Fig. 5.9). Peculiarly, the reflections of c-GST225 are again present in Fig. 5.11f (annealing of 7 h). The epitaxial relationships between the t-GST225 and c-GST225 phases and the Si(111) substrate can be determined directly from the pole figures. The epitaxial relationships of t-GST225 are

$$\text{t-GST225}(0001) \parallel \text{Si}(111),\ \text{t-GST225}[0\bar{1}10] \parallel \text{Si}[11\bar{2}], \qquad (5.1)$$

respectively, while those of c-GST225 are

$$\text{c-GST225}(111) \parallel \text{Si}(111),\ \text{c-GST225}[11\bar{2}] \parallel \text{Si}[11\bar{2}], \qquad (5.2)$$

In the following section, the focus is put on the as-grown t-GST225 thin film. A closer view of each t-GST225 pole density maximum in the measured pole figure of the as-grown film reveals that there are actually two pole density maxima for every expected single pole density maximum present in the calculated stereographic projection (Fig. 5.11b) [100, 173]. These two measured pole density maxima are rotated azimuthally by +6° and−6° around the expected azimuthal angular position, i.e. by 12° with respect to each other. This means that in addition to a rotation of 180°, t-GST225 crystallites are also rotated by ±6° from the model-expected azimuthal orientation. For the as-deposited thin film and the films annealed for up to 45 min, point-like pole density maxima of t-GST225 can be discerned, while for films annealed for a longer time, i.e. for 150 min or longer, tend to exhibit line-like t-GST225 pole maxima extending over the model-expected angular position.

This indicates that the annealing process promotes these t-GST225 crystallite orientation distributions more prevailed in those azimuthal regions around the expected pole density maxima position. The intensity ratio between these two ±6° rotated pole density maxima is 5:1 for the as-deposited film and systematically decreases for the films annealed for longer times, until the ratio reaches 2:1 for the film annealed for 7 h.

5.1.2.4. Microstructure of epitaxial GST225 thin films

The cross-sectional annular dark-field STEM (ADF-STEM) micrographs in Fig. 5.12a and b give an overview of the as-deposited GST225 thin film. The images show that the as-deposited GST225 film consists of crystallites with elongated and plate-like shapes, confirming the results of AFM investigations. The representative selected area diffraction (SAED) pattern (Fig. 5.12c) of this film is rather complicated, indicating the presence of multiple phases and planar defects in the thin film. The HAADF-HRSTEM micrographs in Fig. 5.12d–f depict the GST225/Si(111) interface region, marked by white arrows. The images show that the as-deposited GST225 film is aligned according to the hexagonal basis vector of the substrate surface plane. The bright dots in Fig. 5.12d–f above the Si(111) substrate are Sb/Te atomic columns, indicating that the GST225 layer growth was initialized by a Si surface passivation with a Sb/Te layer, followed by a VdW type bonding to the first Te stacking plane of the GST225 building block. Such quasi-VdW epitaxy was also demonstrated in Refs. [88, 113, 178].

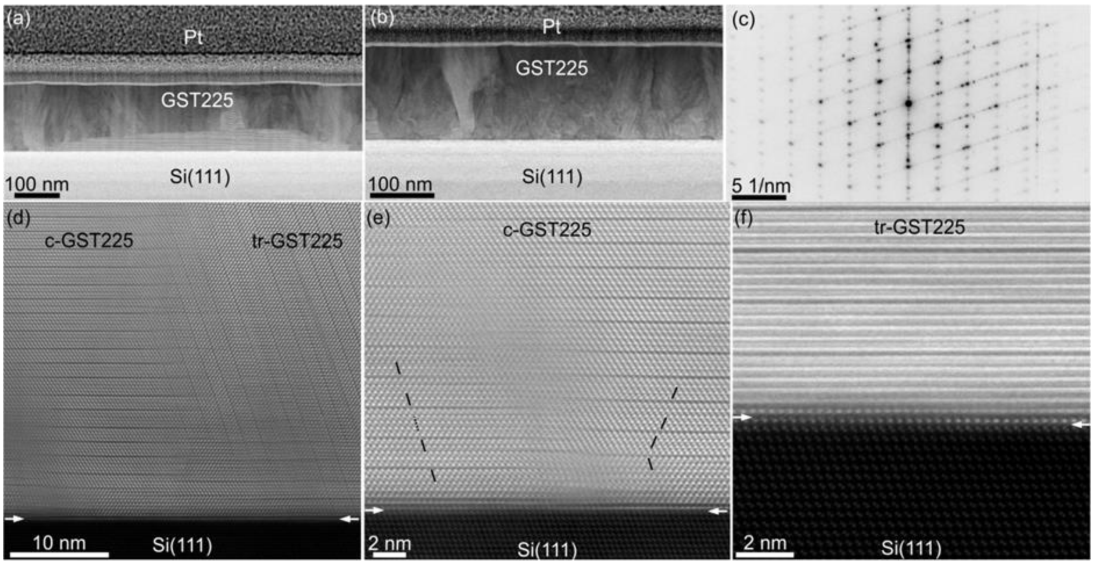

Fig. 5.12. (a)–(b) Overview ADF-STEM images of an as-grown GST225 thin film. Crystallites with different shapes and sizes are seen in the images. (c) Representative SAED pattern is shown. (d)–(f) HAADF-HRSTEM micrographs of the Si(111)/GST225 interface regions. The c-GST225 phase II with highly-ordered vacancy layers is seen in (d) and (e). Antiphase-boundaries (between black and dotted black lines) and twins are also identified in image (e). The black lines mark the Te layers, whereas the dotted black line marks the GeSb layer. The Si(111)/GST225 interface is marked by white arrows. A small out-of-plane rotation of t-GST225 is identified in (f). The bright dots above the Si(111) are Sb/Te atomic columns. The Pt layer on top of the GST thin film is due to the FIB specimen preparation. Viewing direction is c-GST225$[1\bar{1}0]$ ǁ t-GST225 $[11\bar{2}0]$ ǁ Si $[1\bar{1}0]$. The t-GST225(0001) planes and the c-GST225(111) planes are parallel to the Si(111) planes.

As already derived from the XRD measurements, the as-grown film consists of two phases, i.e. c-GST225 and t-GST225, which can be discerned in the HAADF-HRSTEM image in Fig. 5.12d. Both c-GST225 phase (primarily phase II) and t-GST225 phase grow on the Si(111) substrate surface. It should be noted that the c-GST225 phase II cannot be identified in $2\theta - \omega$ XRD scan. Contrary to the t-GST225 structure, there is no sliding between the building blocks in the c-GST phase II. Interestingly, in some of the crystallites the vacancy stacking layers are not only oriented parallel to the surface of the Si substrate, but with a distinct inclination angle to the substrate surface. This inclination angle is preferably governed by the set of the Si{111} planes, as depicted in Fig. 5.12d. From the figure it can be seen that the vacancy layers are tilted by 70.5° with respect to the horizontal film/substrate interface line. This is in good agreement with the angle between two sets of {111} planes in the fcc GST225 crystal structure (70.53°). The presence of twins and also antiphase-boundaries (APB) in the c-GST225 phase II can also be discerned from Fig. 5.12e. The formation of APBs in the c-GST225 phase II can be associated with the initialization of t-GST225 phase formation with sliding Te layers between two adjacent building blocks.

The presence of a domain rotation of around ±6° as observed in the in-plane pole figure measurements (see Fig. 5.11) is also confirmed by Fig. 5.12f. The imaged t-GST225 domain is out-of-plane rotated by approximately 6°with respect to the expected calculated azimuthal orientation (see Fig. 5.12f). In the micrograph only lattice planes corresponding to the (0001) family are visible. This comparably small angle twisted domain was also observed in other epitaxial PCMs [138]. One possible explanation is due to domain-matched epitaxy of large lattice-mismatched thin film [179, 180]. It involves matching of lattice planes between which have similar crystal symmetry, and the misfit is accommodated by the integral multiple of lattice planes across the interface. By assuming domain rotation angle of 60°, the rotation angle of each pole density maximum around its high symmetry position, according to the theoretical calculation [179], is approximately ±7.9°. It is 2° larger than experimental data (±6°). This discrepancy might be due to nucleation of both cubic and trigonal GST225 grains.

Such concurrent nucleation of two phases implicates rather complex processes that involve the nucleation and growth of different crystallites. This means, there are perpetual conformations of crystalline parameters between two phases during the process, such that an optimum configuration is achieved by a formation of domain twisting. These twisted domains are maintained through phase transformation to the trigonal phase, as observed in Fig. 5.11c and d with two pole density maxima around each model-expected position of pole density maxima. By annealing for a longer time, the trigonal crystallites start to reconfigure, resulting in a more prevailed intensity around the model-expected pole density maxima position (see Fig. 5.11e and f). Another possibility could be the presence of remains of the amorphous native oxide on the substrate surface that might be not perfectly removed during the cleaning and etching process. This oxide could deteriorate the orientation distribution of crystallites. Fig. 5.13 shows that to some extent there are inclined GST225(0001) planes present with regard to the substrate surface.

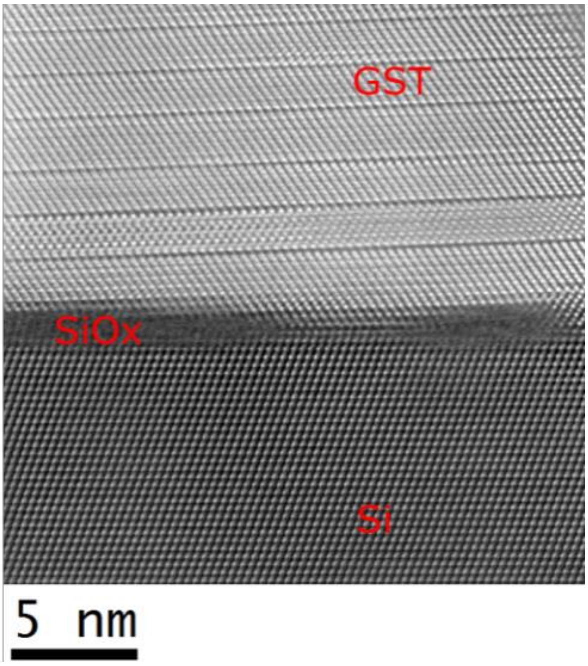

Fig 5.13. HRSTEM image of an as-deposited GST film annealed for 4 h. Regions of native oxide, SiO_x, are present on the Si substrate surface. As a consequence, inclined (0001) planes with regard to the Si surface are present.

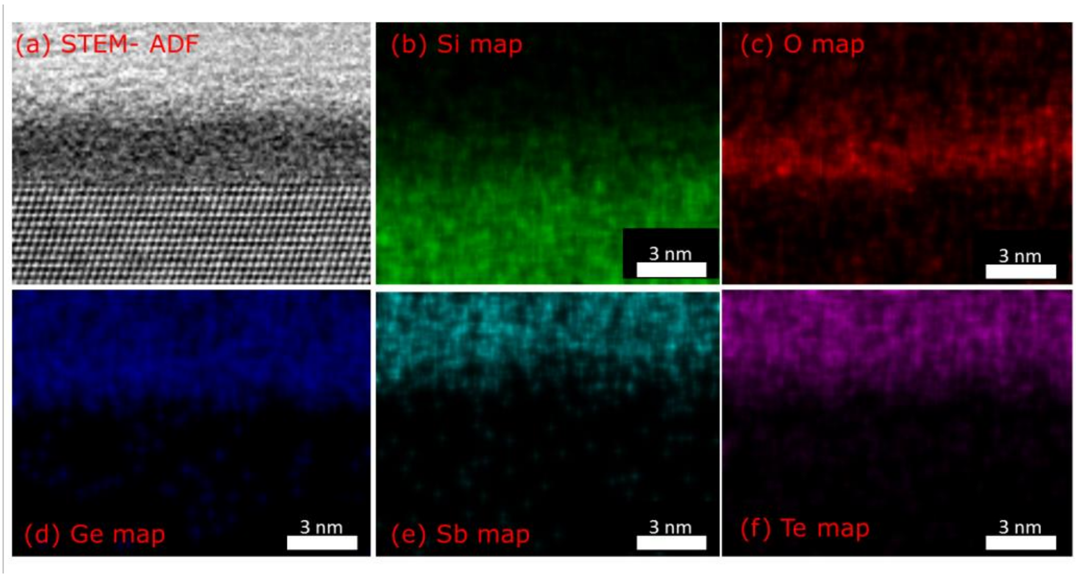

Fig. 5.14. (a) ADF-HRSTEM image and (b)-(f) EDX elemental maps of GST film annealed for 4 h. The elemental maps show that there exists a region of native oxide on the Si surface

Fig. 5.13 and 5.14 show the presence of SiO_x at the substrate-layer interface, observed by HR-STEM and HRTEM-EDX, respectively. From Fig. 5.13, it can be pointed out that there exists a distinct small angle inclination of GST(0001) planes with regard to the substrate surface, obviously due to the presence of SiO_x. This might be precisely due to a configuration between layers growth on SiO_2-covered and uncovered (etched) surface. Unlike on the clean Si substrate, on the SiO_2-covered substrate there is no Sb/Te passivation layer formation at the beginning of the GST growth. Such laterally-alternating substrate surface conditions can create a disturbed GST growth process, resulting in the observed inclined crystallites configuration. Formations of the GST124, GSt225, and GST326 phases, as well as the presence of crystal twins are also discerned. The inclined crystallites are assumed to form due to the configuration of the crystallites that are grown on a Si surface partly covered by native oxide. In addition, unlike the epitaxial GST225 crystallites on clean Si, the crystallites which are grown on SiO_x/Si are not bonded by a Sb/Te passivation layer. A previous study [178] have shown also that there is no evidence of Sb/Te layer formation in epitaxial GST225 on Si substrates partially covered with amorphous SiO_x.

In order to perform a deeper investigation on the local crystal structure of the identified c-GST225 crystal lattices, HRSTEM was applied. Fig. 5.15a shows the presence of both c-GST225 and t-GST225 phases. Interestingly, the distinct formation of two kinds of c-GST225 phases can be observed in Fig. 15b. One is the c-GST225 phase I with random distribution of GeSb/vacancies (GeSb/V). This disordered crystalline c-GST225 phase I was also reported of by Matsunaga et al. by XRD [100] and modeled by Eom et al. [108]. A similar local crystal structure was also reported for laser-irradiated GST225 samples [112]. The other part found in Fig. 5.15b is identified as c-GST225 phase II in which the vacancies are accumulated in layers parallel to {111} planes.

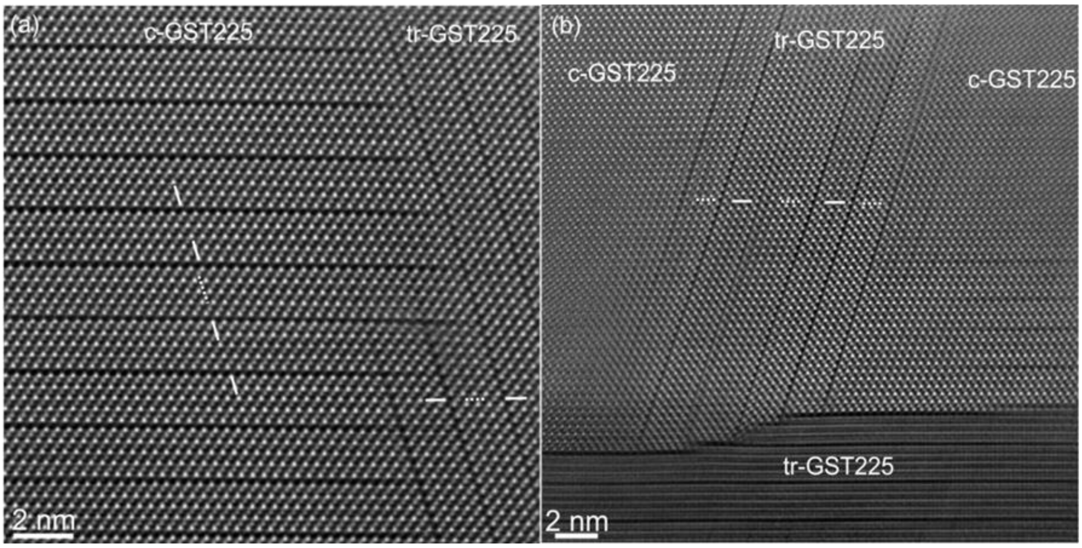

Fig. 5.15. (a)–(b) HAADF-HRSTEM images of c-GST225 phase II and t-GST225 grains formed in an as-deposited GST225 thin film. The c-GST225 phase II with highly-ordered vacancy layers is visible in Fig. 5.15a, whereas the c-GST225 phase I with randomly distributed vacancies is imaged in Fig. 5.15b. The white lines mark Te layers, whereas the

dotted white lines mark GeSb layers. Antiphase boundaries exist in c-GST225 between white line and dotted white lines in Fig. 5.15a. Viewing direction is c-GST225[110] ‖ t-GST225 $[11\bar{2}0]$.

Such a vacancy aggregation into an individual plane parallel to the c-plane is attributed to lowering the energy of the system. The structure of c-GST225 phase II with layered vacancies possesses lower energy compared to one with randomly distributed vacancies [125], so that vacancy layer formation is energetically favorable. Since the local structure and lattice distortions are similar to the t-GST225 phase, the formation of the c-GST225 phase II can also be considered as a transient structure during transformation from cubic to trigonal phase. Recent results on the transformation from crystalline to amorphous phase showed a formation of transition structure without resonant bonding in c-GST225 before amorphization [135]. Thus, the GST225 phase II can also be considered as a transient phase during transformation from the crystalline to an amorphous phase [116].

By annealing as-deposited films at the same temperature as T_s, the pure t-GST225 films with micron-sized grains can be produced as observed in Fig. 5.16a. Fig. 5.16b presents an SAED pattern of a t-GST225 film. Only Si{111} reflections are visible in the pattern which indicate the presence of a small out-of-plane rotation of the Si substrate with regard to the film. The four spots which are located in between the zero reflection and GST225(0005) point out that the film consists mainly of GST225 building blocks. As shown by the HAADF-HRSTEM image of Fig. 5.16, for the film annealed for 45 min predominantly the typical 5 Te lattice plane stacking for each crystal building block intercalated by VLs is observed. This local stacking sequence correlates well with the t-GST225 phase. However, in addition to 5 Te lattice plane stacked building blocks, 4 and 6 Te layer stacked building blocks are observed, too, which correspond to trigonal $Ge_1Sb_2Te_4$ (t-GST124) and $Ge_3Sb_2Te_6$ (t-GST326) phases, respectively. The formation of the GST326 phase is believed to be due to a mechanism to compensate the GST124 phase formation in order to preserve the overall system chemical composition of the GST225 phase [93].

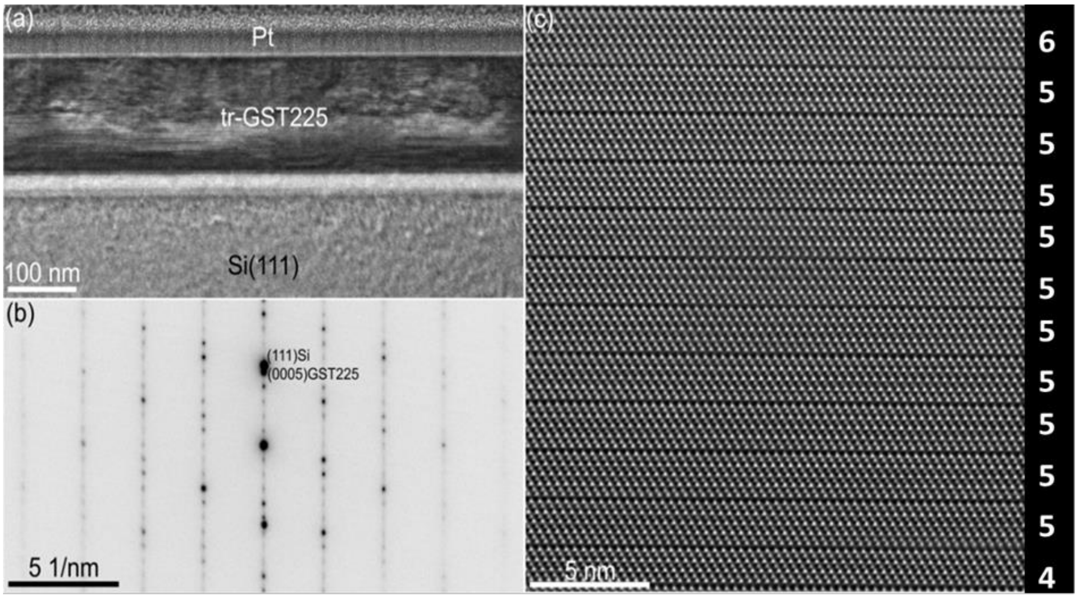

Fig. 5.16. (a) Bright-field TEM image of a t-GST225 thin film obtained by annealing of an as-deposited GST225 thin film at 220 °C for 45 min. (b) SAED pattern of the t-GST225 film. Si(111) spots are present in the pattern showing a small out-of-plane rotation of the Si(111) substrate. Four spots are located between the zero reflection and GST225(0005) in the pattern pointing out that the thin film consists mainly of GST225 building blocks. (c) HAADF-HRSTEM image of t-GST225 showing the presence of GST225, GST124 and GST236 building blocks. The Pt layer in (a) is due to the FIB specimen preparation, whereas the bright contrast at the Si substrate surface in (a) is from a local thickness gradient remaining after the low-energy Argon ion milling.

Table 5.1. The film chemical compositions measured by EDX-TEM. All the films show compositions close to that of the GST225 target, while the film annealed for longer time, 7h, exhibits a Ge-deficient composition.

Element, at %	as-grown	annealed for: 30 min	45 min	7 h
Ge	21.6	22.0	22.2	19.1
Sb	23.3	24.0	23.7	26.2
Te	55.1	54.0	54.1	54.7

EDX-STEM measurements of the GST225 films show that all the investigated films possess a chemical composition very close to $Ge_2Sb_2Te_5$, as seen in Table 5.1, showing the chemical compositions of the GST films as measured by EDX-TEM. However, a Ge deficiency is observed in the film annealed for 7 h. This Ge-deficiency of the film results in the formation of t-GST124 and t-GST225 building blocks (see Fig. 5.17). The Sb/Te vdW monolayer is bonded with the adjacent six-fold Te building block, which is then followed by random sequences of four or five-Te layered building blocks. The four-, five- or six-fold stacking corresponds to t-

GST124, t-GST225, or t-GST326, respectively. The Sb/Te vdW monolayer is still intact although the film was annealed for a comparably long duration of time (7 h), which shows that the Sb/Te vdW monolayer is thermally stable at the used temperature range.

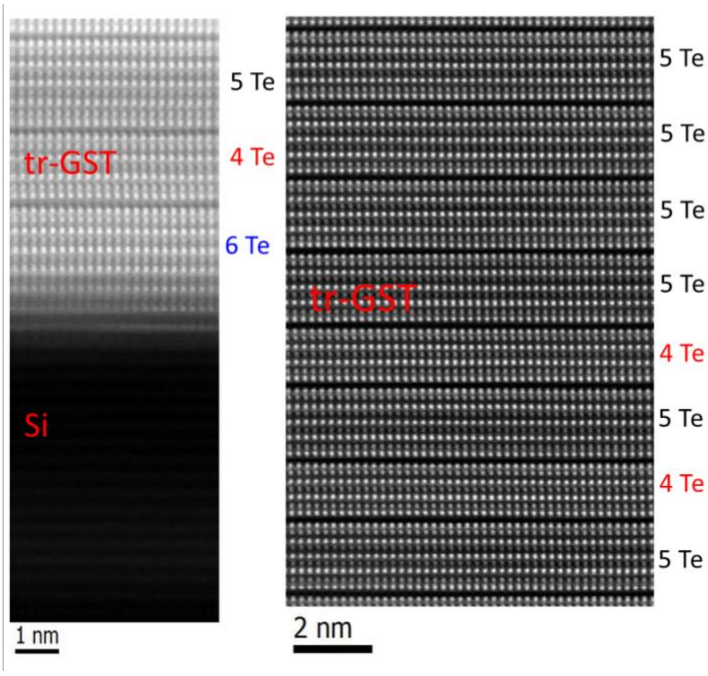

Fig.5.17. HAADF-HRSTEM image of a t-GST225 film annealed for 7 h showing local stacking sequences of GST225, GST124 and GST236 building blocks. The Sb/Te passivation layer is still present.

The co-existence of various crystalline structures of a GST225 alloy is interesting from the technological point of view. Due to differences in the electrical resistance of crystalline GST structures [116, 183], a realization of multi-level memory cells could be possible. Particularly, the structural transitions within the cubic GST225 lattices can be a promising approach for data storage applications with high switching speed and reduced energy consumption which is similar to interfacial PCMs (iPCMs) or chalcogenide superlattices based memory [184]. Moreover, the multilevel storage devices based on solely crystalline structures will benefit from much more stable resistance states over time which is still an issue in multi-level data storage utilizing amorphous-crystalline state transitions [9].

5.2. Sb_2Te_3

The second alloy to be investigated is two-dimensionally bonded Sb_2Te_3. As stated, lattice mismatch of Sb_2Te_3 to that of Si is relatively large, i.e. ~11%. As was in the investigation on GST films, the discussion will start from the *in-situ* growth observation and followed by the investigation on topographical surface of the films as well as crystallinity and local structures which would uncover the growth mechanism of this alloy on such large-mismatched substrate, i.e. Si(111).

5.2.1. Film growth

The crystalline quality of the surface was *in-situ* monitored by means of RHEED during the deposition of each film at different T_s. The clean unreconstructed Si substrates exhibit a streaky RHEED pattern with Kikuchi lines, as seen in Fig. 5.18a. The image reveals the high crystalline quality of the Si surfaces. Also, the chemical cleaning and etching processes of Si provide an oxide-free and smooth surface, which is desirable for the growth of an epitaxial thin film. For the films deposited at T_s ranging from RT to 100 °C, only diffuse RHEED patterns are observed (not shown). This demonstrates that within this temperature range, T_s is too low to promote a nucleation of crystallites. At T_s = 140 °C, a streaky pattern with low intensity started to appear for the as-deposited film (not shown). This indicates that this substrate temperature is sufficient to initiate the nucleation of crystalline regions.

Furthermore, for all the films deposited at $T_s \geq 160$ °C, the RHEED patterns are nearly identical, typically represented by Figs. 5.18b and c, showing the RHEED patterns of the selected films deposited at 220 °C. The transition from the reflection of the substrate to that of the first layer of the film can be observed, as depicted by Fig. 5.18b. The snapshot was taken 60 s after the deposition started, associated to ~1.3 nm of film thickness. In the figure, a sharp streaky intensity is observed, pointing out that the films are epitaxially grown with high crystallinity and a smooth surface topography. A typical RHEED pattern of the as-deposited film can be seen in Fig. 5.18c. The fact that a streaky pattern can be observed indicates that the as-grown films are smooth and have excellent surface crystallinity. Fig. 5.18c shows a diffraction pattern, which is identical to the one in Fig. 5.18b, except that the intensity maxima are more pronounced.

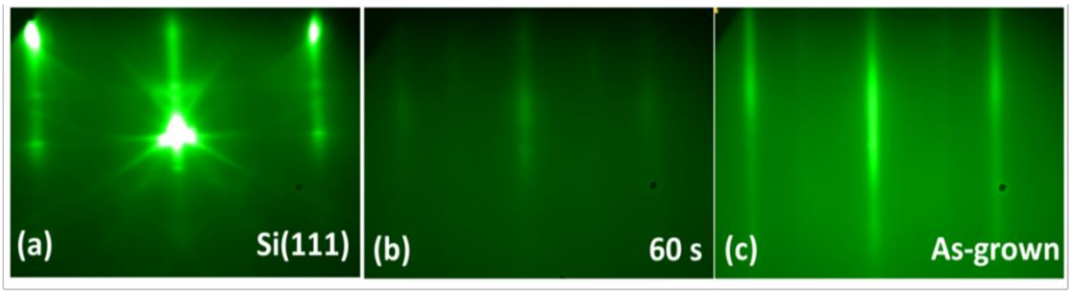

Fig. 5.18. RHEED patterns of (a) wet-chemically cleaned Si(111), (b) Sb_2Te_3 layers taken 60 s after deposition started, and (c) as-grown Sb_2Te_3 thin film deposited at 220 °C. The electron beam was parallel to $\langle 1\bar{1}0 \rangle$ direction of the Si(111) substrate.

5.2.2. Film thickness and topography

As confirmed by XRR and SEM, the deposition rate was approximately constant (~1.3 nm/min) up to T_s = 230 °C (the film thickness of around 80 nm).

However, the rate dropped dramatically for the film deposited at $T_s \geq 240$ °C (the thicknesses are ~18 nm and ~12 nm for the films deposited at 240 and 260 °C, respectively). Fig. 5.19 shows the XRR measurements of the two exemplary films deposited at 210° C (~83 nm) and 240 °C (~18 nm).

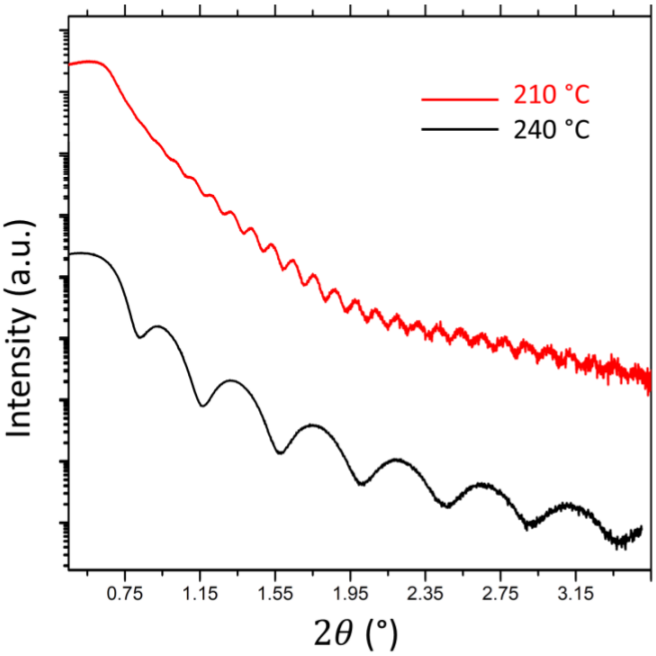

Fig. 5.19. X-ray reflectivity (XRR) measurements of Sb_2Te_3 thin films deposited at 210 °C (red) and 240 °C (black).

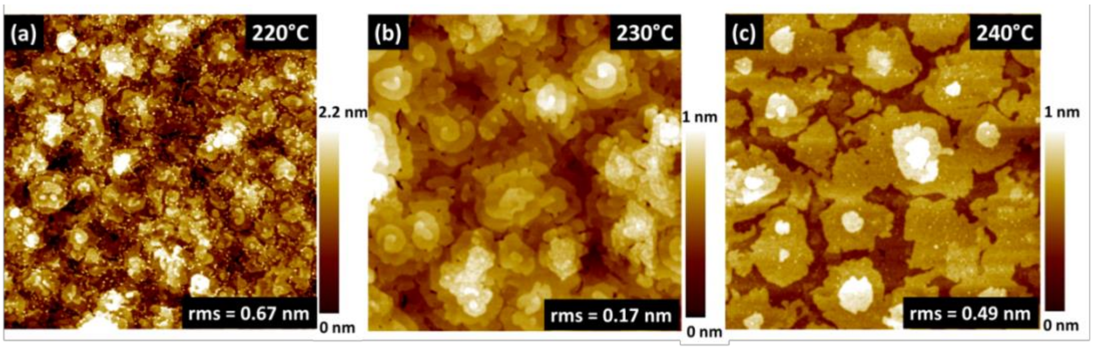

Fig. 5.20. AFM images of the as-deposited thin films. (a), (b), and (c) show the topographies of the films deposited at 220, 230, and 240 °C, respectively. All the figures are presented in $2 \times 2\ \mu m^2$ scale.

The surface topographies of as-deposited films were observed by means of AFM. Fig. 5.20 shows the selected as-deposited films, deposited at 220, 230, and 240 °C, respectively. The AFM measurements confirm that each film typically possesses a smooth surface. The root mean square (RMS) roughness of all layers is less than 1 nm. Fine spiral-like structures with atomically smooth terraces are seen, especially in Fig. 5.20b. This spiral-like structure was also observed on MBE-grown films [185, 186]. For slightly higher deposition temperature (240 °C, Fig. 5.20c), the AFM measurement reveals the presence of atomically smooth terraces and steps, with a step height of 1 nm (1 quintuple layer). The spiral-like structures are almost not visible here. From these results, in connection with RHEED data, it can be assumed that, by means of PLD, epitaxial Sb_2Te_3 thin films typically grow in a two-dimensional growth mode. This layer-by-layer growth mode is desirable for a further outlook, i.e., the fabrication of a chalcogenide superlattice structure by means of PLD.

5.2.3. Film crystallinity

The crystalline structure and texture of Sb_2Te_3 thin films were investigated by measuring symmetrical $2\theta - \omega$ XRD scans. Fig. 5.21 shows $2\theta - \omega$ scans of the films deposited at different T_s between RT and 260 °C. The film deposited at RT, as shown by the black curve, represents only the amorphous structure, since there is no significant intensity peaks. However, the occurrence of small peaks situated at 8° and 17° which correspond to Sb_2Te_3(0003) and (0006) planes, respectively, indicates the presence of the trigonal phase. The next data to be presented in Fig. 5.21 are the films deposited at T_s starting from 170 °C, showing only narrow and intense peaks which are associated to (000*l*) planes according to the calculated XRD spectra [121, 173]. It points out that the films deposited within these temperatures possess a high crystalline quality.

Special attention is on the film deposited at 240 °C. The film exhibits Laue fringes, showing that the film is homogeneous and possesses a high crystalline quality with a smooth surface. The rocking curve measurement of this film shows a narrow rocking curve peak with FWHM of ~0.04°, as shown in Fig. 5.22. Follow that the data are logarithmically plotted. Above a deposition temperature of 260 °C, the process is dominated by surface desorption during the deposition, resulting in a lower deposition rate. From XRD it is found that the Sb_2Te_3 films are epitaxial with out-of-plane orientation of (000l). The epitaxial relationship could be determined to be $Sb_2Te_3(0001)\|Si(111)$. Using results of the XRD studies and the Scherrer relationship, the average grain size was determined to be 55 nm, which is in a good agreement with the lateral grain sizes between 47 nm and 107 nm obtained from cross section TEM images (not shown).

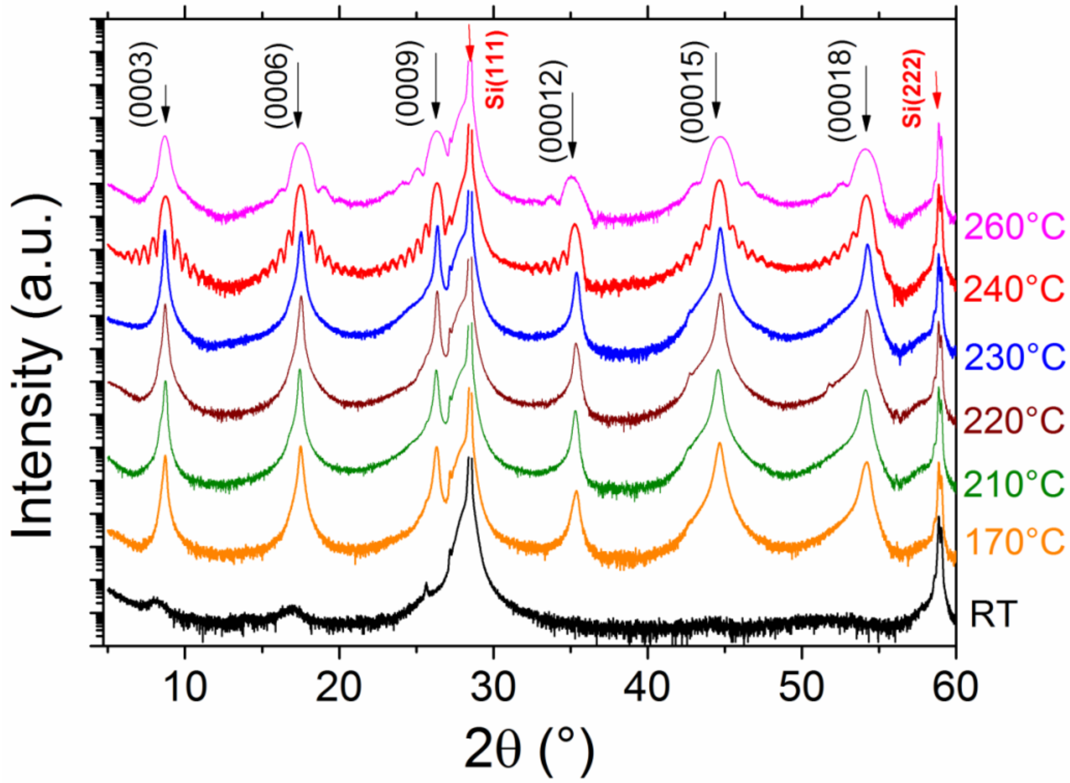

Fig. 5.21. $2\theta - \omega$ XRD scans of Sb_2Te_3 deposited on Si(111) at different substrate temperatures T_s. The black curve belongs to the film deposited at RT, showing mainly amorphous phase. The curves belong to the films deposited at T_s = 170 °C until 260 °C all exhibit only Bragg reflections of trigonal Sb_2Te_3(000l). This shows that the films grow epitaxially in a trigonal crystal structure, according to (000l) out-of-plane orientation. The higher the T_s, the lower deposition rate, but the better crystalline quality.

The crystalline qualities and in-plane epitaxial relation between the film and the substrate are investigated by measuring the in-plane pole figures. These ex-situ measurements are also to confirm the epitaxial window previously determined by *in situ* RHEED measurement. Figs. 5.25a and b present the pole figures of $Sb_2Te_3$$\{1\ 0\ 10\}$ reflections for the films deposited at 130 °C and 220 °C, respectively. The in-plane pole figure of the film deposited at 130 °C shows six pole density maxima. The azimuthal angular distance between two neighboring maxima is 60°. These maxima are accompanied by a ring of low intensity connecting adjacent pole density maxima. The presence of this ring indicates a fiber oriented growth of the polycrystalline film.

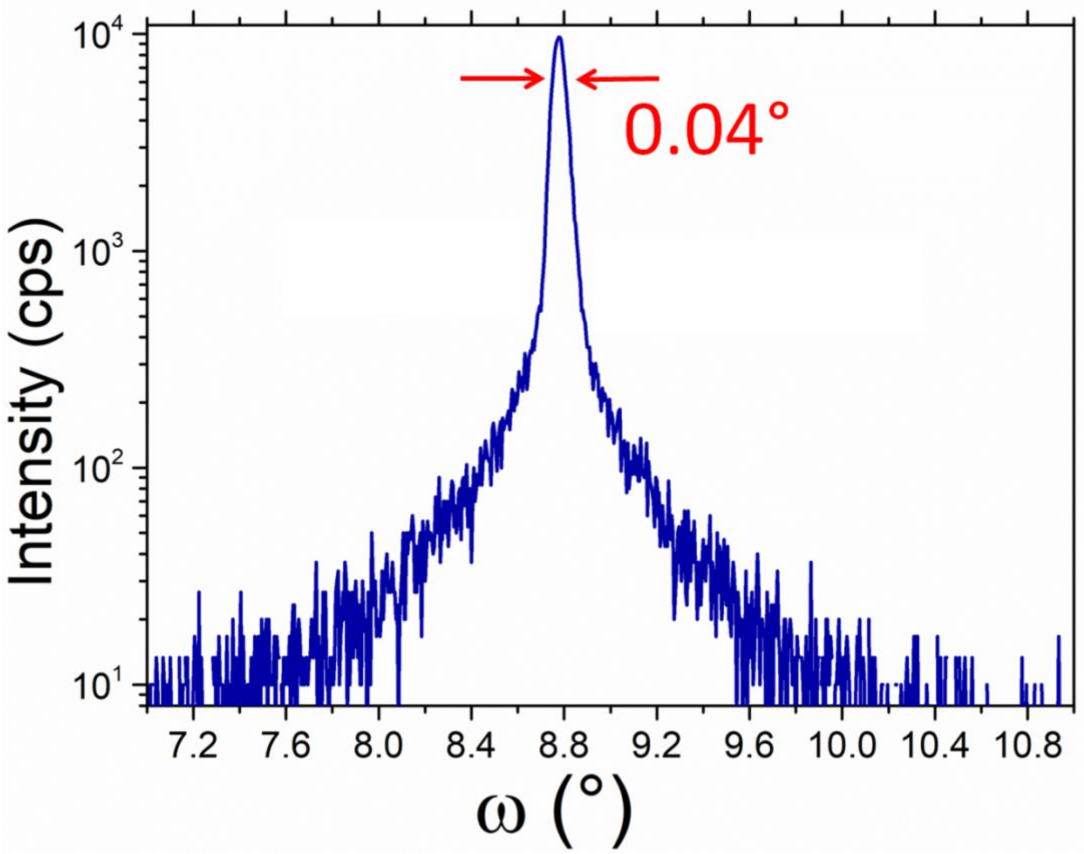

Fig. 5.22. Rocking curve of the Sb_2Te_3(0006) reflection of thin film deposited at 240 °C. The corresponding FWHM of ~0.04° confirms a good mosaicity.

For the film deposited at 220 °C, only those six pole density maxima remain and the ring intensity is not present anymore, as depicted by Fig. 5.23b. This indicates that the film grows strictly epitaxial on Si. The small widths of the pole density intensity distribution for the polar and azimuth angles point out the high quality of the epitaxial growth. The expected position of the diffraction maxima for Sb_2Te_3 [121, 173] was calculated and presented in a stereographic projection in Fig. 5.23c. From this pole figure, it can be discerned that a high symmetry calculation of the trigonal Sb_2Te_3 crystal results in three peaks representing $Sb_2Te_3\{1\ 0\ 10\}$ reflections. It can be concluded that the presence of six, instead of three, pole density maxima in the experimental data points out the presence of a twin domain. Such twin was also observed in the other epitaxial Te-based PCM, i.e., GST [159, 187]. The intensity maxima in the calculated (Fig. 5.23c) as well as in the measured pole figures (Figs. 5.23a and b) are situated at $\alpha \approx 39°$. The azimuthal full width half maximum (FWHM) of the Sb_2Te_3 peak is around 3.5°. This indicates the presence of domain rotation in a small angle, due to an epitaxial growth of a highly mismatched epilayer. To determine the in-plane epitaxial relationship, a Si{220} azimuthal φ-scan was performed (see Fig. 5.23d). The green curve is the φ-scan of Si{220}, while the magenta curve corresponds to $Sb_2Te_3\{1\ 0\ 10\}$ reflections. The in-plane epitaxial relationship is determined to be $Sb_2Te_3[2\bar{1}\bar{1}0] \| Si[1\bar{1}0]$.

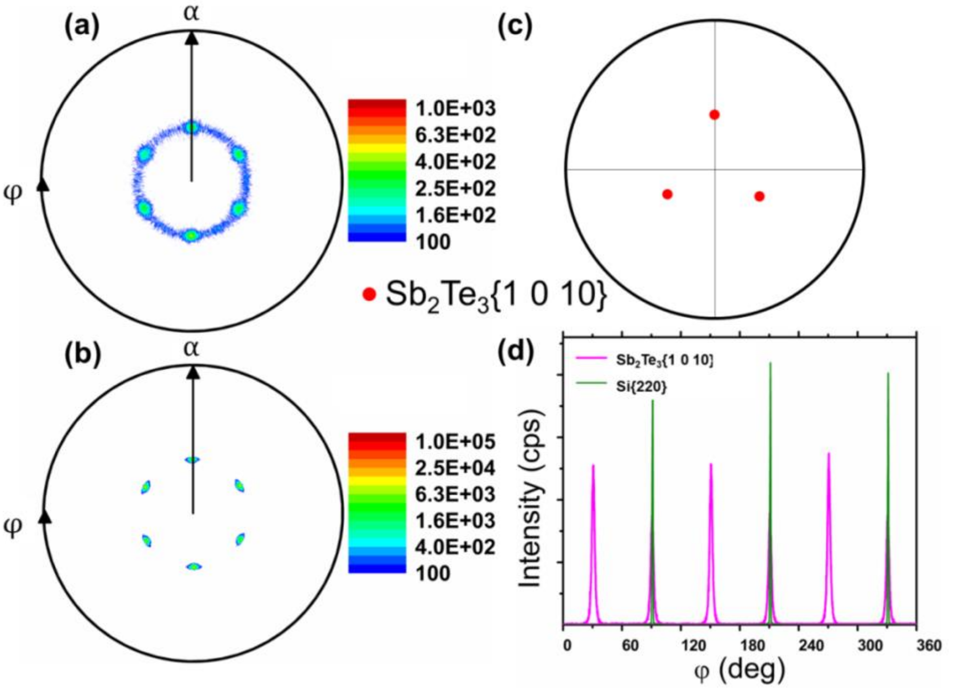

Fig. 5.23. In-plane pole figures of the Sb_2Te_3\{1 0 10\} reflections, for the films deposited at (a) 130 °C and (b) 220 °C. In (c), stereographic projection of model Sb_2Te_3\{1 0 10\} is presented. Thin film in (a) shows six (three times two) pole density maxima accompanied by intensity ring, while in (b), the intensity ring disappeared, while six pole density intensities are much more intense. (d) shows azimuthal scan of Sb_2Te_3\{1 0 10\} and Si\{220\} of the sample in (b).

5.2.4. Microstructure

Fig. 5.24 shows structure images of the Sb_2Te_3 thin film obtained by transmission electron microscopy. Fig. 5.24a presents a wide scale ABF-STEM image of the film deposited at 240 °C. The 17-18 quintuple layers are observed, corresponding to a film thickness of around 18 nm, in agreement to the x-ray reflectivity measurement (not shown here). The presence of defects (twin boundaries) is also revealed, which is in agreement to the in-plane pole figures, as presented in Fig. 5.23. One example of this twin boundary is pointed out by the green arrow at the left-hand side of Fig. 5.24a. Additionally, some mounds are characterized on the thin film surface, as pointed out by the purple arrow in Fig. 5.24a. These mounds have maximum heights of around a single unit of a Sb_2Te_3 building block (1 nm), which is consistent with the AFM images. From this it can be concluded that the Sb_2Te_3 film is typically grown on Si(111) by PLD two-dimensionally by a stacking of Sb-Te quintuple layers.

High resolution scanning transmission electron microscopy (HRSTEM), see Fig. 5.24b, was used to directly observe the microstructure and the atomic order in the Sb_2Te_3 thin films and their interfaces. A single atomic layer of Sb/Te at the

Sb_2Te_3-Si(111) interface can be clearly observed, as indicated by the orange arrow on the left-hand side of Fig. 5.24b. This points out that the Sb_2Te_3 growth is initiated by a Sb/Te surface passivation layer on the Si substrate. Due to almost a similar atomic number and electron scattering cross sections of Sb and Te, the passivation layer is assumed to be a mixture of Sb and Te atomic species. The results of atom probe tomography performed on Sb_2Te_3 and Bi_2Te_3 multilayers grown on Si also showed an intermixing of Sb and Te at the interface [185, 186]. The Sb/Te surface passivation layer was also observed in layered GST grown on Si by PLD [187]. The formation of a surface termination layer is well known to overcome a large lattice mismatch between the substrate and the thin film in VdW epitaxy [122] and was observed for different materials. Through that mechanism, hence, VdW epitaxy is achieved rather than lattice-matched (strained) epitaxy, resulting in a fully relaxed film lattice, even on a highly mismatched substrate. A similar effect was also reported for the deposited Sb_2Te_3 film [188-190], in which Sb or Bi adsorption or deposition on Si is necessary prior to the thin film deposition. However, in the case of the epitaxy of the layered material Sb_2Te_3 by PLD, the termination of the dangling bonds at the Si surface is naturally accomplished within Sb_2Te_3 deposition without any pre-treatment (Si surface reconstruction followed Sb/Te-dangling bond termination) of the substrate. The explanation is that the pulsed laser ablated plasma contains the mixtures of atomic and ionic species as well as clusters. The formation of Sb/Te termination layer formed by the ambient Sb/Te vapor is energetically favorable in order to avoid a high stress/strain in the lattice of the growing thin film.

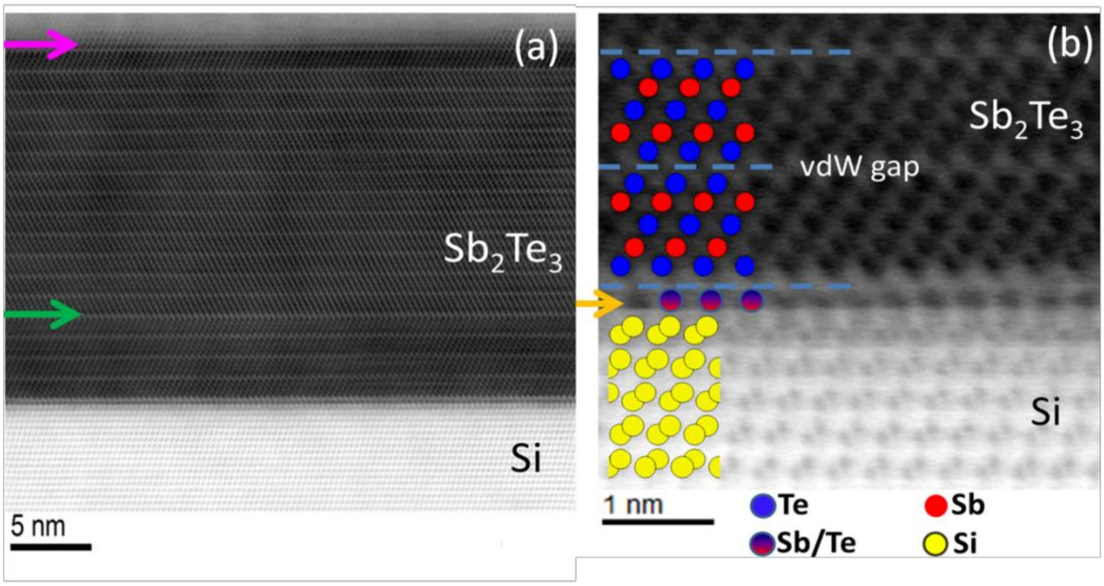

Fig. 5.24. ABF-STEM cross section images of thin Sb_2Te_3 film deposited at 240 °C. (a) shows the HRSTEM image of the same sample in wider scale. The presence of defects (twins) is observed, as marked by the green arrow. The film thickness is around 17-18 units of Sb_2Te_3 building blocks (18 nm). (b) shows a formation of Sb/Te-passivation layer, as marked by the orange arrow, at the Sb_2Te_3-Si(111) interface. The model Sb_2Te_3 and Si crystal (view in Si[$\bar{1}10$] direction) are also presented. The dashed lines mark the quasi vdW gaps.

In Fig. 5.24b, the quintuple layers (2Sb and 3Te), which are the characteristic for the Sb_2Te_3 crystal, are clearly visible. This confirms the stoichiometric preservation in the Sb_2Te_3 thin film epitaxially grown by PLD. Analyzing intensities, the stacking sequence of a single QL is determined to be Te-Sb-Te-Sb-Te-VdW along the c-axis. Each two neighboring quintuple layer building blocks (Te-Te stacking layers) is intercalated by a quasi Van-der-Waals gap. The dashed lines mark out the VdW gaps, which are present on the interface and in the Sb_2Te_3 bulk. The presence of such a 2D crystal structure of Sb_2Te_3 is due to an electron excess possessed by Sb atoms, so that the outermost Te-stacking layers of a building block are passivated [191]. This 2D crystal structure with VdW gaps was also found in other class of materials [192-195]. The corresponding crystal models [121, 173] of Sb_2Te_3 and Si at the interface are also presented. The viewing direction is in Si$[\bar{1}10]$. The Te, Sb, and Si are presented in blue, red, and yellow, respectively. The gradual color represents the mixture of Sb/Te.

5.3. GeTe

The main focus of this section is on the growth of the 3D-bonded GeTe alloy on Si(111). The use of a (111)-oriented substrate is in order to minimize interfacial energy for a growth of (0001)-oriented GeTe. The GeTe crystal has *in-plane* lattice mismatch of ~8.3% with regard to Si(111). In this work, the growth of epitaxial GeTe on Si(111) is firstly investigated. Secondly, the epitaxial Sb_2Te_3 thin layer [123, 196] was deposited on Si(111) as a seeding layer for a growth of epitaxial GeTe. The use of the seeding layer is in order to improve epitaxial growth of GeTe. The lattice parameter *a* of Sb_2Te_3 only differs by around 2.5% to that of GeTe in hexagonal lattice (or around 1% lattice mismatch in rhombohedral settings of unit cell) [101, 107, 121, 127]. Importantly, the 2D bonding characteristic of Sb_2Te_3 implies on a ‘self-constructed’ VdW epitaxy using PLD, which, in an ideal case, annihilates any induction of a lattice strain which could happen due to a large mismatch substrate like Si [123]. Hence, 2D-bonded Sb_2Te_3 is ideal to use as a seeding layer for a growth of 3D-bonded GeTe. This also provides a potential for an improvement especially in engineering of chalcogenide hetero-structures [36, 87, 197], where a greater flexibility in process parameters is prerequisite in order to control the degree of layer-intermixing [88, 95, 198].

In summary, our main objectives here is to demonstrate the possibility of the growth of epitaxial GeTe thin film on highly mismatched Si(111) substrate by PLD, discuss the growth mechanism of GeTe, and improve the epitaxial nature of GeTe by employing VdW-bonded material as a seeding layer. The last part deals with the discussion of the local structure of epitaxial GeTe.

5.3.1. Film growth

The surface properties of the substrate and the grown layer were monitored during and after the growth by means of *in-situ* RHEED analytical system. The films grown at the substrate temperatures, T_s, from RT to 190 °C show only a diffused RHEED intensity patterns (not shown) within the whole deposition processes, indicating that within this range of temperatures the as-grown films are predominantly amorphous.

Interestingly, at T_s = 200 °C and above, the situation is quite different, at which the as-grown films show the distinct RHEED patterns with no diffused intensity, indicating that the as-grown films are crystalline. The comprehensive overview of the growth scenario during the deposition is presented in Fig. 5.25a-f, showing typical RHEED patterns of the epitaxial films deposited on Si(111) at temperatures from 210 °C and above. Fig. 5.25a-f show the important stages during the deposition of the epitaxial film at T_s = 230 °C. In Fig. 5.25a, the RHEED pattern of the cleaned (111)-oriented Si substrate is presented. The streaky patterns with Kikuchi lines can be discerned, indicating a smooth surface topography of the surface with a high crystallinity, which is desirable for a growth of an epitaxial thin film. It also shows that a surface oxidation has been successfully removed by the wet-cleaning process. Soon after deposition started, the diffused RHEED intensity was observed at early stage of GeTe growth, as seen in Fig. 5.25b. Fig. 5.25b shows the RHEED image taken at 1.5 min from deposition onset, corresponding to a GeTe thickness of ~1.5 nm. This diffuse intensity is observed until around 90 s from deposition onset (a thickness of ~2.2 nm or 2 GeTe hexagonal unit cells or 6 GeTe bilayers). From this time point, the streaky RHEED intensity starts to gradually arise. Up to this extent, it can be concluded that the growth of epitaxial GeTe is initialized by a formation of an apparently amorphous ultra-thin GeTe layer. A crystalline phase is subsequently induced when a certain thickness is reached. The formation of the amorphous layer has also been investigated previously [136] which might be explained due to an impairment in a formation of the normal GeTe distorted structure characterized by a bonding hierarchy within the crystal.

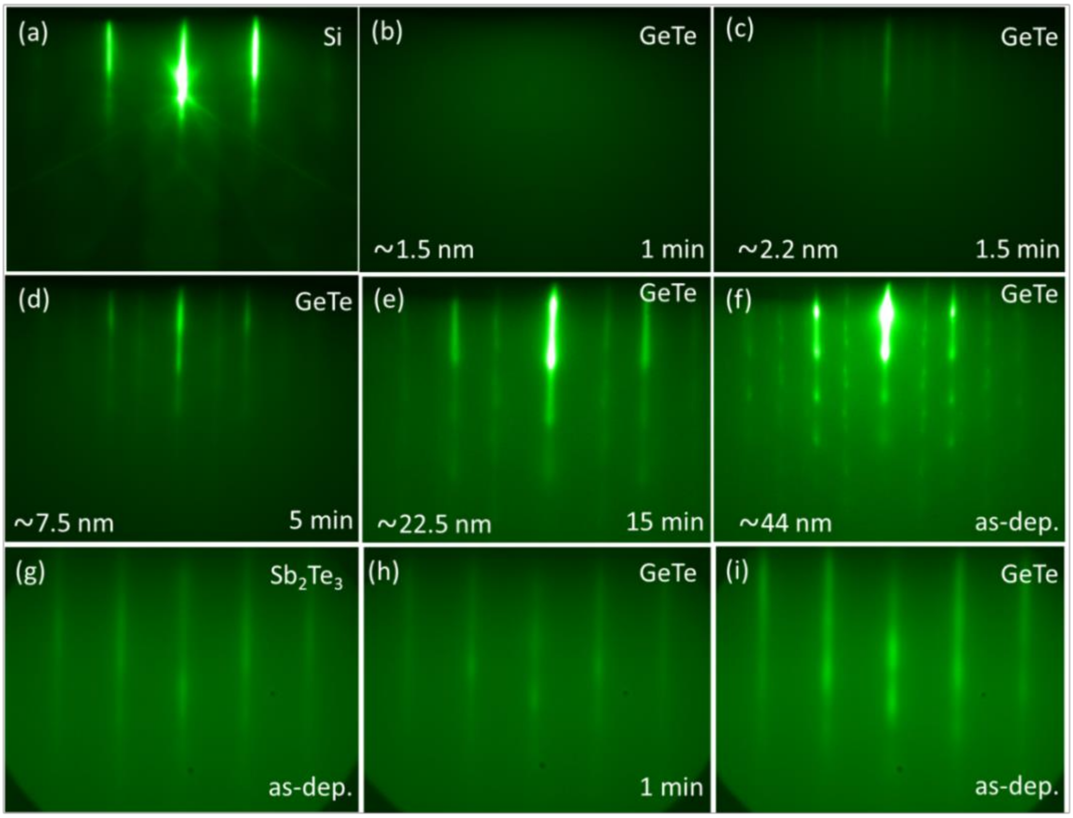

Fig. 5.25. Real-time RHEED patterns during deposition of GeTe at 230 °C on Si(111). (a) shows streaky pattern of unreconstructed Si(111) surface. In (b) is RHEED image taken at 60 sec (~1.5 nm) after deposition started. The streaky GeTe RHEED patterns (c) start to emanate at 1.5 min, associated to ~2.2 nm thickness (6 GeTe bilayers), showing a smooth surface topography. (e) and (f), showing RHEED patterns of the grown layer after 15 min and as-grown film, respectively. RHEED patterns of (g) as-grown ultra-thin Sb_2Te_3, (h) GeTe layer after 60 sec and (i) as-grown GeTe film deposited on Sb_2Te_3/Si(111) at 210 °C all show striped intensities, indicating smooth surface topographies.

As long as the deposition continued, this streaky intensity becomes more intense, while the diffused intensity gradually disappears until completely is gone after around 5 min (~7.5 nm). The streaky pattern indicates that a smooth surface morphology of the growing layer within this deposition time duration. The streaky pattern is kept constant, until around 15 min (~22 nm), on which the point-like (transmittance-like) intensity gradually becomes more intense, indicating an occurrence of surface roughening, i.e. the growth mode turns to be three-dimensional. This point-like pattern coexisted by streaky intensity, is constant until the deposition was completed. The point-like patterns indicate the large (3D) islands while the remaining streaky intensity shows that the large islands are flat (it will be confirmed and discussed later in Fig. 5.27). This concludes that epitaxial GeTe film grows in 2D mode in the beginning of the growth, which tends to turn to be 3D mode with the growing film thickness. To be more concise, it can be concluded that pulsed laser deposited epitaxial GeTe thin film grows on Si(111) in the mix between 2D and 3D modes.

The second set of samples is the GeTe films deposited on Sb_2Te_3-seeding layer on Si(111). Fig. 5.25g shows the RHEED pattern of as-deposited thin Sb_2Te_3 layer. The typical elongated stripes of RHEED pattern were characterized during and at the end of the Sb_2Te_3 deposition, indicating the 2D growth mode of ultra-thin Sb_2Te_3. On the onset of GeTe deposition, as seen in Fig. 5.25h, the direct transformation from a streaky RHEED pattern of Sb_2Te_3 to a streaky RHEED pattern of GeTe was observed, without diffused RHEED intensity in transition stage as observed in GeTe on Si(111). This striped pattern is conserved until the end of deposition, as shown in Fig. 5.25i, indicating a smooth surface topography of the as-grown film. To this extent, it might be concluded that, in contrast to the films deposited on Si(111), for the GeTe films on Sb_2Te_3 buffer layer the epitaxial GeTe films was directly formed from the beginning of deposition and the film is grown in the Frank-Van der Merwe (2D) growth mode.

The deposition rates of the films are determined by performing XRR as well as STEM measurements. The increasing substrate temperatures are accompanied by the decrease of deposition rates. The deposited amorphous films have deposition rate of around 4 nm/min possessing the thicknesses of 135 nm, while the thicknesses of the epitaxial films deposited at 210 °C, 260 °C and 270 °C are 48 nm (1.6 nm/min), 23 nm (0.7 nm/min) and 15 nm (0.5 nm/min), respectively. Above 270 °C, almost no thin film was deposited due to desorption of Ge and Te atomic species. This severe desorption at high temperature (typically around 300 °C) was also observed for epitaxial GST film on Si by PLD accompanied by a shift in chemical compositions of the GST alloy [123, 159, 187].

5.3.2. Film crystallinity

The crystalline structure of the films was firstly investigated by measuring symmetrical $2\theta - \omega$ XRD diffractograms. All the films deposited from RT until 190 °C show no Bragg reflections except those of Si substrate lattice planes (not shown). This notifies that the as-grown films are amorphous, which also confirm the observation using RHEED.

Also, in accordance with observations using RHEED, at temperature of 200 °C and above, the situations are different. Fig. 5.26 presents XRD based measurements of crystalline films. Fig. 5.26a shows 2θ XRD pattern of the GeTe films deposited on Si(111) at T_s = 200, 210, and 260 °C in red, green and orange colors, respectively. All the experimental data are plotted in logarithmic scale. As seen in Fig. 5.26a, at 200 °C and above the films show mainly two intense peaks, i.e. situated at around $2\theta = 25.05°$ and 51.52°, which are associated to the calculated XRD profiles of (0003) and (0006) planes reflections of trigonal structure [127] (or (111) and (222) reflections, respectively, in rhombohedral unit cell) [101, 130]. As only two (000*l*) peaks as marked by the vertical dashed lines are present, it can be concluded that the GeTe is grown with (000*l*) *out-of-plane* orientation on Si(111).

The GeTe diffraction peaks, especially those in higher 2θ, i.e. (0006) reflection, show also intensity shoulder at slightly higher 2θ with regards to the expected peaks, indicating a presence of reflections of oblique planes of rhombohedral unit cell. In a previous report this feature has been also shown [199]. At higher deposition temperatures above 250 °C, the double peak is more obvious, which gives impression that each of the two reflections are typically split into two peaks, as represented by the film deposited at 260 °C. A possible explanation is a co-existence of the polymorphic high temperature rock-salt structure. It means that the distortion (along [111] of rhombohedral primitive cell), partly vanishes, in which $\alpha = 58.36°$ shifts towards 60° for an ideal rock-salt structure. This small shift of α corresponds to a shift of 2θ Bragg peak around 0.4°. It is assumed that the *c*-planes are always *out-of-plane* oriented. It was also known that, opposite to Ge-Sb-Te alloys like $Ge_2Sb_2Te_5$ [187], GeTe does not follow Oswald's step rule [200], meaning that GeTe normally crystallizes in normal phase of trigonal structure at RT, which transforms into the cubic phase at higher temperature. Another possibility is based on the assumption that the Peierls distortion [83] does not actually vanish, but only randomized, instead [134]. It means that the double peak (and shoulder) is a manifestation of randomized lattice distortion in {111} direction, seen in rhombohedral setting.

The ω-scan measurements were also performed to assess the *out-of-plane* tilting distribution of the crystallites with regard to substrate surface. The measurements were carried out at the example of GeTe(0003) plane (not shown). The film deposited at 210 °C and above possess typical rocking curve-full width half maximum (FWHM) of around 0.08°, indicating well-ordered *out-of-plane* (0001) planes with a small mosaicity.

A set of GeTe films were also grown on Sb_2Te_3-seeding layer on Si(111) at T_s = 145, 150, 210 and 230 °C. In Fig. 5.26a, 2θ-scan of Sb_2Te_3-buffered GeTe film deposited at 150 °C is presented in blue. For a sake of assisting in data interpretation, the measured Bragg reflection of Sb_2Te_3 is also presented (black) [123]. The two reflections belong to (0003) and (0006) trigonal structure of GeTe can be discerned, accompanied by the set of c-planes Bragg reflections of seeding layer Sb_2Te_3. Since the temperature is significantly lower than commonly found epitaxial window of GeTe on Si(111), e.g, around 220-270 °C [138], it clearly demonstrates that by the use of Sb_2Te_3-seeding layer, the epitaxial window can be substantially extended towards lower temperature regimes and hence the film's crystallinity is improved.

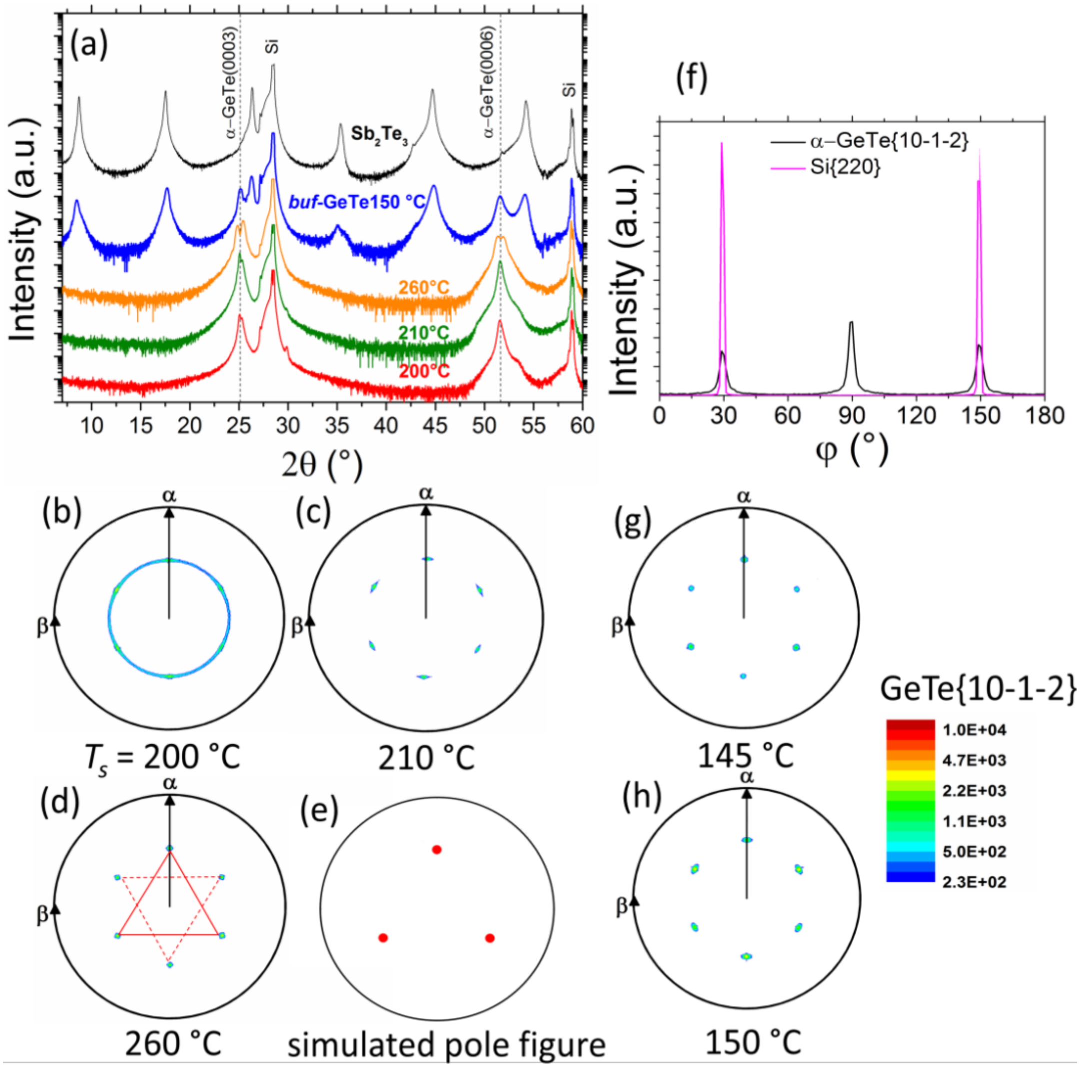

Fig. 5.26. The XRD measurements of GeTe thin films: (a) 2θ-diffractograms of GeTe films deposited on Si(111). The (0001)-oriented trigonal phase is characterized. The peak splitting is typically observed in films deposited at high temperature of 250 °C and above, which might show the co-existence of high-temperature rock-salt polymorph. The blue and black curves show the GeTe film grown on Sb_2Te_3/Si(111) and a Sb_2Te_3 film [123], respectively. *In-plane* pole figures of GeTe$\{10\bar{1}\bar{2}\}$ planes of the films grown at (b) 200 °C, (c) 210 °C, (d) 260 °C, and (e) the simulated stereographic projection [127, 173]. α and β correspond to a polar and azimuthal angle, respectively. In (f), the rocking curves of GeTe$\{10\bar{1}\bar{2}\}$ (black) and Si{220} (magenta) are shown. (g) and (h) show the in-plane pole figures of GeTe films deposited on Sb_2Te_3/Si(111) at 145 °C and 150 °C, respectively.

5.3.3. Texture Analysis

For a texture analysis and a determination of the epitaxial window, the *in-plane* pole figures measurements were performed. Fig. 5.26b, c and d show the measured pole figures of GeTe$\{10\overline{1}\overline{2}\}$ planes for the selected films deposited from 200 °C, 210 °C and 260 °C, respectively, where the experimental data are plotted in logarithmic scale. The pole figures of the film deposited at 200 °C shows a predominant ring intensity (Fig. 5.26b), showing the textured polycrystalline phase of the film. The situation is different for the films deposited at 210 °C and above, as represented by Fig. 5.26c and d (210 and 260 °C, respectively). All pole figures in Fig. 5.26c and d of the films show the six, i.e. two times three, pole density maxima only, where the ring intensity is not present. It assesses that the films deposited at 210 °C and above are grown epitaxial. Each pole density maximum are situated at $\alpha \approx 55.3°$ corresponding to the GeTe$\{10\overline{1}\overline{2}\}$ reflections, in agreement with the calculated stereographic projection of $\{10\overline{1}\overline{2}\}$ planes as presented in Fig. 5.26e [127, 173]. The presence of six, instead of three, pole density maxima, indicates the presence of the twinned crystallites. To guide the eye, a set of pole density maxima referring to a specific oriented domain is marked by red triangle in Fig. 5.26d, while the three other maxima referring to the corresponding twinned domain are marked by dashed triangle. This twinning is commonly found in chalcogenide alloys [123, 178, 187, 201]. Taking a closer look at both pole figures (Fig. 5.26c and d), it can be discerned that the pole density maxima are getting somewhat narrower especially in azimuthal direction for 260 °C film. This shows that the increase of deposition temperature within epitaxial window leads to an improvement in crystal texturing.

An improvement in the epitaxial nature is shown in GeTe films grown on Sb_2Te_3-seed layer on Si(111) substrate. The pole figures of the GeTe films grown on Sb_2Te_3-seed layer at 145 °C and 150 °C show exclusively six pole density maxima (see Fig. 5.26g and h), each of which is separated to each other by azimuthal angle of 60°. There is no ring intensity present between the maxima showing that the film is grown in epitaxial fashion. The deposition of GeTe at temperature lower at 140 °C, the films are mostly characterized by high ring intensities showing polycrystalline film phase accompanied by random intensities contributed by amorphous phase. This results show that, by the employing the Sb_2Te_3-seed layer, the activation energy for crystallization is lowered down, resulting in an extended epitaxial window especially towards lower temperatures up to 145 °C. The improvements on device and material characteristics due to the influences of material interfaces has been shown [202, 203]. The use of Sb_2Te_3 as a template for GeTe was also shown to lower down the activation energy for crystallization of amorphous GeTe by annealing, i.e. up to 2.6 eV, equivalent to 90 °C lower than normal crystallization temperature [184, 204].

In order to determine the *in-plane* epitaxial relationship of the GeTe layer to the substrate, an pole figure XRD measurement of Si{220} was performed. Fig. 5.26f shows Bragg peaks of Si{220} (magenta) and GeTe$\{10\overline{1}\overline{2}\}$ (black) measured as a function of rotational angle φ around the substrate (111) axis. From this figure, one can determine the in-plane epitaxial relations of GeTe(0001) to Si(111) can be determined to be GeTe$[11\bar{2}0] \parallel$ Si$[\bar{1}10]$. This shows that pulsed laser deposited GeTe films on unreconstructed-Si are exclusively epitaxial and do not show a domain rotation around the expected pole density maxima, as commonly observed in MBE-grown on Si substrate [138]. In PLD epitaxial GeTe, only single sharp peak observed every 60° azimuthal rotations, which confirms the quality of the PLD films. This also shows a straightforward method to deposit epitaxial alloy using PLD. Furthermore, it could be also determined the epitaxial relations of the films deposited on the seeding layer Sb_2Te_3 on Si to be GeTe$[11\bar{2}0] \parallel Sb_2Te_3[11\bar{2}0] \parallel$ Si$[\bar{1}10]$.

5.3.4. Morphology and topography

The evolution of topography for each film deposited at different process conditions was observed by means of *ex-situ* AFM. The film deposited at RT shows a smooth surface, with root mean square (RMS) roughness of 0.22 nm (not shown). Fig. 5.27a and b respectively show the AFM image of the GeTe film deposited on Si(111) at 210 °C and its corresponding topographic line profile drawn along the film surface (blue line in Fig. 5.27b). It can be discerned that the film deposited on Si typically contains triangularly formed grains with diameters ranging between 50 and 300 nm. The triangles point out two opposite directions indicating the presence of twinned crystallites. However, some randomly orientated triangles can also be found, which indicates the presence of small fraction of domain twists of the film deposited at 210 °C. This also confirms the pole figure measurement in Fig. 5.26c.

In the line profile (Fig. 5.27b), it is seen that the triangular grains are separated to each other by valleys with depths of up to approximately 30 nm. However, these large grains have smooth surfaces. This explains the point-like RHEED patterns coexisted by the streaky intensities as seen in as-deposited film in Fig. 5.25f. To be more specific, the point-like RHEED pattern (Fig. 5.25f) comes from a three-dimensional (rough) surface, while the coexisting striped intensity originates from smooth grain surfaces. The measured RMS roughness is ~5 nm. The typical RMS values of the epitaxial films deposited on Si(111) is between 3 and 5 nm. As revealed previously, the film grows in the 2D and 3D growth modes.

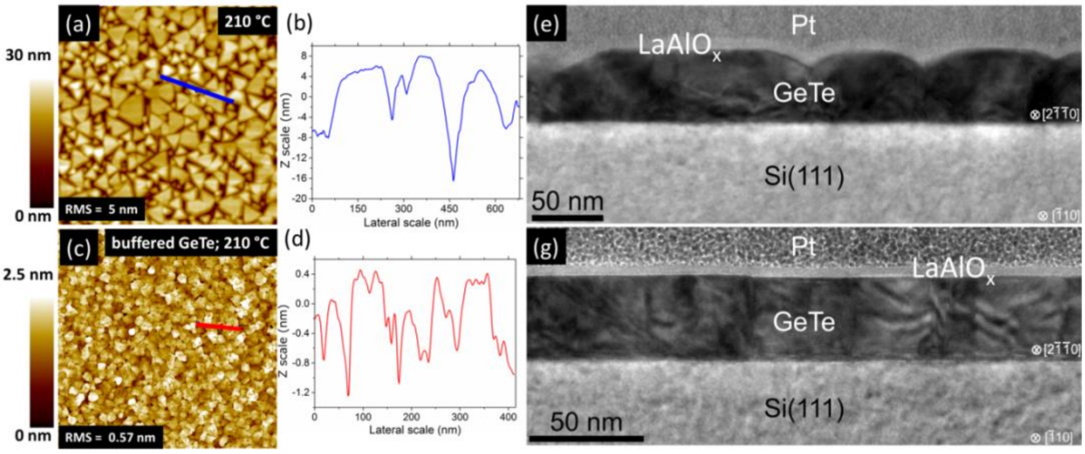

Fig. 5.27. AFM images ($2 \times 2\ \mu m^2$) of the GeTe film deposited at (a) 210 °C on cleaned Si(111) and (b) its corresponding topographical line profile. (c) and (d) show the GeTe films deposited on Sb_2Te_3-seeding layer on Si(111). Low magnification cross-sectional TEM images of (e) GeTe on Si(111), and (g) GeTe on Sb_2Te_3/Si(111), both deposited at 210 °C. In (e), the wave-like contrast indicates the strained GeTe lattice. Comparison between both images, (e) and (g), concludes the different surface topography between the two films. (e) shows a mound-like surface, meanwhile (g) shows significantly smoother surface. A closer inspection into the GeTe surface in (g) reveals monolayer steps, indicating a layer-by-layer growth.

Another set of samples is the GeTe films grown on Sb_2Te_3 seeding layer on Si(111). This buffered films show a better surface quality than those deposited on Si(111). Fig. 5.27c and d show the AFM images of the films deposited Sb_2Te_3 seeding layer on Si at 210 °C and its corresponding line profile marked by the red line on Fig. 5.27c. The smooth surface topography with RMS of less than 1 nm is typically characterized for the films deposited on Sb_2Te_3-seeding layer. In Fig. 5.27d, a surface topography with maximum heights of 1 nm can be observed, which is an approximate of a single GeTe unit cell of ~1.07 nm [101, 107]. By comparing Fig. 5.27a and c, it can be concluded that the improvement of the surface quality can be obtained by employing a thin 2D grown Sb_2Te_3 as a seeding layer. This result also reveals that by the use of Sb_2Te_3 seeding layer, the films are grown in 2D mode, implying a significantly smoother surface of as-deposited film.

To assess the observations of surface topography by AFM, the microstructure images of the films obtained by HRTEM are presented, as seen in Fig. 5.27e, f and g. Fig. 5.27e shows the cross-sectional micrograph for the film deposited at 210 °C on Si(111). A morphology with 3D grains separated by large valleys is visible. These grains possess smooth surfaces, as also observed by AFM.

The observed 2D/3D growth mode might be due to a presence of strain on the interface. The presence of the strains on the interface, in some extents, might be also related to the occurrence of diffused RHEED pattern on the onset of GeTe growth, as seen in Fig. 5.25b. This unconventional growth onset scenario was also observed in

MBE-grown film [137], and can be explained to be related to the instability of GeTe lattice which is prone to a lattice distortion [84, 135]. The diffused pattern on the onset of the growth was ascribed to a disturbance for the formation of an ordered Peierls distortion within this ultra-thin layer due to an influence of interfaces [136], in this case—a lattice-match epitaxy, i.e. the epitaxial growth which is largely influenced by the difference of lattice parameters between substrate and film. The absence of resonant bonding implies on the absence of long-range order (not necessarily short-range order). Hence this ultra-thin layer is characterized as amorphous, which brings about a diffused RHEED pattern. However, as the layer thickens, the self-formation of resonant bonding is achieved, rendering the whole growing layer crystalline [137].

One can see that the growth scenario of GeTe is contrasting to that of 2D chalcogenide Sb_2Te_3, grown by PLD [123]. For the growth of Sb_2Te_3 a formation of a single Sb/Te layer is self-accomplished in the beginning of the Sb_2Te_3 growth on order to passivate Si dangling bonds, and hence a van der Waals epitaxy is achieved and smooth surface is always observed during the layer growth. In such van der Waals epitaxy, the difference in lattice parameter between substrate and film is not important any longer and the lattice is totally relaxed even though the difference is large [123]. However, in the growth of $Ge_2Sb_2Te_5$ with mixed phases (see Chap. 5.1.2), i.e. metastable type I (random vacancy) and type II (ordered vacancy), and stable phases, a partly diffused RHEED intensity was also observed using PLD [187], see Subsection 5.1.2. By excluding the possibility of occurring oxide layer on Si [187], to this point, a simple correspondence may be built by linking the bonding nature of the chalcogenide film to its growth nature, i.e. the formation of this thin amorphous alloy only occur due to a 3D bonding nature of chalcogenide, such as GeTe and metastable GST, where a bonding hierarchy plays a role in a lattice-matching epitaxy [84, 135-137].

Fig. 5.27g shows the film deposited on Sb_2Te_3-seed layer/Si(111) substrate. It can be clearly assessed that the roughness is significantly decreased compared to that of the film deposited on Si(111), confirming the observation using AFM in Fig. 5.27c. The closer inspection of the film topography reveals monolayer step terraces on the surface, which indicates the 2D growth of the film. The Sb_2Te_3 layer grows on Si by Van-der-Waals epitaxy through a self-passivation process of Si dangling bonds, occurring during deposition [123], resulting in a totally relaxed lattice even in films with thickness of some monolayers. This result again demonstrates that in this case Sb_2Te_3, as a seeding layer can improve the surface condition of 3D bonded GeTe films.

5.3.5. Microstructure

The structure of the grown film was investigated by STEM. Fig. 5.28a shows HRSTEM image of GeTe thin film grown on Sb_2Te_3/Si(111) substrate. The two parallel white dashed lines mark the Sb_2Te_3 seeding layer thickness which is around

4 nm. The film is capped by amorphous $LaAlO_x$. The three squared regions marked by b, c, and d refer to different areas within the film. The corresponding structural information of the areas obtained by fast Fourier transform (FFT) analyses are shown in Fig. 5.28b, c and d, respectively. The grains of GeTe show two distinct type of diffraction contrast. The grains with uniform contrast (areas b and d in Fig. 5.28a) are the neighboring grains with lamellar fringes contrast (area c in Fig. 5.28a). FFT analyses from the respective areas of the Fig.5.28a were used for further structural analysis. The FFT pattern in Figs. 5.28b and d can be assigned to single grain of GeTe whereas the FFT in Fig. 5.28c shows extra reflections, e.g. in one-third and two-thirds of the (00.3) GeTe reflection. The single grain is rotated by 180° around c-axis with respect to each other, thus, forming two twinned {10.0} crystallites, while the extra reflections in Fig.5.30c are due to a superposition of the twinned grains. Figs. 5.28e represents HRTEM image of GeTe grain with lamellar fringe contrast. The fringes in Fig. 5.28e are spaced by 1.07 nm, which corresponds to the distance between four Te layers in [0001] direction. Additional investigations by HAADF-HRTSEM revealed the local stacking of Te within of areas which have shown lamellar fringes in HRTEM. The intensity of Te columns in the right part of the image is uniform whereas the intensity of Te columns in the left part of the micrograph is non-uniform. Te columns spaced by 1.07 nm appeared with higher intensity. Owing to *Z*-contrast imaging, the columns with lower intensity are, thus, due to lower occupation at these sites.

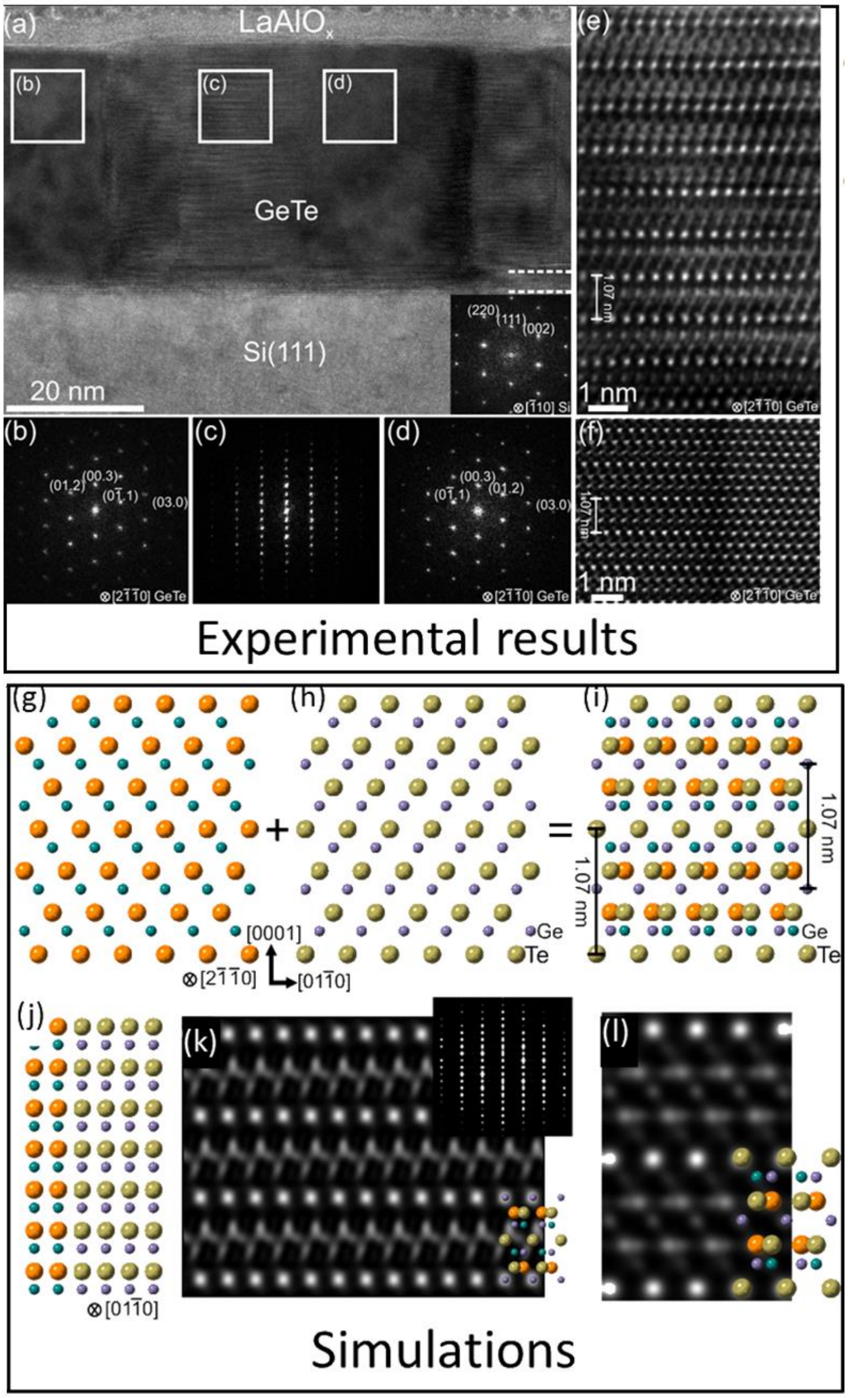

Fig. 5.28. TEM image of the GeTe film deposited on Sb_2Te_3/Si(111) is shown in (a). The two parallel dashed lines adjacent to Si mark out the buffer layer. The amorphous layer above GeTe is capping $LaAlO_x$ layer. In (a), some different squared regions marked by b, c and d letters denote the different domains corresponding to different Fast Fourier Transform (FFT) reflections (diffractograms) shown by (b), (c) and (d), respectively. (b) and (d) confirm the presence of domain {100} twin, while the boundary region in (c) show a more complicated pattern interpreted as an overlap of both crystallites of (b) and (d). (e) and (f) are HRTEM and HAADF-HRSTEM images, respectively, show *c*-plane stacking in epitaxial GeTe. (f) well.

5. 4. Summary

At final, the growths of epitaxial thin films of three different alloys, i.e. $Ge_2Sb_2Te_5$, Sb_2Te_3 and GeTe, on Si(111) substrates using PLD were discussed. The summary is divided into three different parts, namely deposition of GST, Sb_2Te_3 and GeTe.

GST

The epitaxial $Ge_2Sb_2Te_5$ thin films were successfully deposited on Si(111). The deposition rates decrease with increasing substrate temperature T_s, indicating a strong desorption taking place during the deposition process which is also accompanied by shifting of the out-of-plane Bragg peaks towards the GST124 phase reflection position for higher T_s above 250 °C. The out-of-plane rocking curve of each film consists of two single-centered contributions, i.e. a narrow peak which possesses a constant FWHM for all samples, around 0.06°, and a broad peak of which the FWHM decreases with increasing substrate temperature from around 2.5° for films deposited at 170 °C to 0.06° at 300 °C. The AFM measurements show triangular shapes of the layer topography features. Polycrystalline films with a preferred GST(0001) orientation form for the films deposited at substrate temperatures of up to 170 °C, whereas epitaxial films formed in the substrate temperature window from 200 °C to 300 °C. By varying the laser frequency, it was demonstrated that epitaxial GST films can be grown by PLD with a deposition rate as large as 42 nm/ min.

The slight reduction of substrate-target distance from ~7.5 cm to ~6 cm implies on significant different properties, e.g. the formation of coexisting cubic and trigonal GST225 phases in the thin films and the alteration of in-plane epitaxial relationship. Using the reduced substrate-target distance, epitaxial GST225 thin films with heterogeneous vacancy structures were grown on Si(111) substrates at the moderate substrate temperature of 220 °C. Annealing of the GST225 thin films at 220 °C directly after deposition resulted in the transformation of the cubic GST225 phase into a purely trigonal phase. The chemical compositions and local stacking sequences of the epitaxial GST225 films after annealing correspond to t-GST255. However, the formation of t-GST124 and t-GST326 building blocks was also observed. These blocks are necessary for the maintenance of overall system chemical composition. The loss of Ge was identified after annealing of the film for longer time (7 h), which was associated with the formation of mainly t-GST124 and t-GST225 building blocks. The thin film growth is initialized by a Sb/Te surface passivation layer, which was also stable even after heating for 7 h.

The co-existence of distinct crystal structures of cubic GST225 phase was revealed by advanced transmission electron microscopy. The crystal structure of the c-GST225 phase I is described by a distorted rocksalt-like structure with randomly distributed vacancies, whereas the crystal structure of the c-GST225 phase II consists of rock-salt-type building blocks with alternating Te and GeSb layers. The blocks are separated from each other by intrinsic VLs. Contrary to the t-GST225 structure, there is no shift between the blocks in c-GST225 phase II. The c-GST225 phase II is considered as a transient structure during transformation from crystalline-to-amorphous phase and during phase transition from cubic-to-trigonal phase. In addition, the fabrication of GST225 crystalline structures with various disorders might beneficial for further application in multi-level fast nonvolatile data storage.

Sb_2Te_3

The stoichiometric epitaxial Sb_2Te_3 thin films have been also successfully grown on wet chemically cleaned Si(111) substrates by PLD. Epitaxial growth is achieved for the films deposited at the temperature range between 140 °C and 280 °C. The best Sb_2Te_3 thin film was produced at $T_s = 240$ °C. Smooth film topographies with a maximum roughness of 1 QL (1 nm) are typically observed for as-deposited Sb_2Te_3 thin films. The Sb_2Te_3 thin films were grown on Si determined to follow a layer-by-layer growth mode, by a stacking of Sb-Te quintuple layers. The film possesses a trigonal crystal structure with (0001) out of plane orientation. The growth of Sb_2Te_3 thin films is initiated by the self-organized formation of a Sb/Te single-atomic passivation layer on the Si surface. The crystalline Sb_2Te_3 structure is built of quintuple layer building blocks, in which quasi VdW-bonding intercalates every two building blocks.

GeTe

Epitaxial GeTe thin films were also grown on highly-mismatched Si(111) substrates by means of PLD. The epitaxial window is determined to be 210-270 °C. The *in-situ* investigation using RHEED system reveals that the growth of the GeTe film on Si(111) was initialized by the formation of an ultra-thin amorphous layer. Especially in the end of deposition process, the films were predominantly grown in the mix of 2D and 3D growth modes. The epitaxial GeTe films were grown in trigonal structure, with the epitaxial relations are of GeTe(0001)||Si(111) and GeTe$[11\bar{2}0]$||Si$[\bar{1}10]$. By employing a 2D bonded Sb_2Te_3 as a seeding layer on Si(111), the epitaxial window of GeTe can be extended especially towards the lower temperature regime, up to 145 °C. Additionally, the surface topography can be significantly improved with typical RMS of less than 1 nm, which may indicate that the films are grown in 2D growth mode on the buffered (Sb_2Te_3/Si(111)) substrate. The twinned domains are found in the epitaxial GeTe films. The investigation on the local atomic arrangement reveals the presence of overlapping twinned domains in the region of twin boundary, which we believe to be the characteristic of the alloy. This work demonstrates the possibility of improving epitaxial thin films of 3D bonded materials by employing a 2D bonded material as a seeding layer. Not to be limited to chalcogenides, this work may also demonstrate a prospective way to grow other material with 3D bonding characteristic with better surface topography.

Chapter VI
Chalcogenide superlattice structure

As mentioned, the interfacial phase change material (iPCM) which is based on chalcogenide superlattice (SL) structure has been demonstrated to show the improved switching properties [36] rendering the structure a strong contender for a non-volatile data storage device. With the preliminary knowledge of the growth of epitaxial chalcogenide films (i.e. GST225, Sb_2Te_3 and GeTe) using PLD as a basis, the depositions of SL structures have been successfully done. In this chapter, fabrications and characterizations of these GeTe-Sb_2Te_3 based SLs are discussed.

6.1. The growth of GeTe-Sb_2Te_3 superlattices

As explained in the experimental section (see Section 4.1), each GeTe-Sb_2Te_3 SL structure was fabricated by seven-times alternating depositions of Sb_2Te_3 and GeTe on Si(111) resulting in a SL structure with nominal seven GeTe-Sb_2Te_3 stacking units. As demonstrated in the deposition of epitaxial chalcogenide films, RHEED system was proved to be efficient to employ for an *in-situ* monitoring of the surface conditions, i.e. the smoothness and crystallinity of the substrate surface and of each grown layer. The RHEED patterns were recorded just before, during and after the depositions. Fig. 6.1 shows the recorded RHEED patterns. As seen in Fig. 6.1a, the Si(111) substrate exhibits the typical streaky RHEED pattern denoting a smooth and highly crystalline Si surface needed for the growth of a SL structure. This surface state is a result of the wet-chemical cleaning process.

For all of the SL structures, a Sb_2Te_3 layer is firstly deposited at 240 °C (see Section 4.1 for more details about the SL structure deposition experiment). The reason for this is that such a thin Sb_2Te_3 layer would take the role of a seeding layer for the growth of the above-deposited layers. This is due to the fact that the growth mechanism of Sb_2Te_3 on Si(111) by PLD is characterized by the formation of of a thin film via Van-der-Waals epitaxy resulting in a totally relaxed film lattice, see Section 5.3. The deposition temperature of 240 °C is considered the optimum temperature at which the high quality epitaxial film with excellent crystalline properties is obtained (see Section 5.2). Thus, the deposition of the first Sb_2Te_3 thin layer (from now the so-called Sb_2Te_3 seeding layer) at 240 °C can provide a good platform for the deposition of the next higher-order layers.

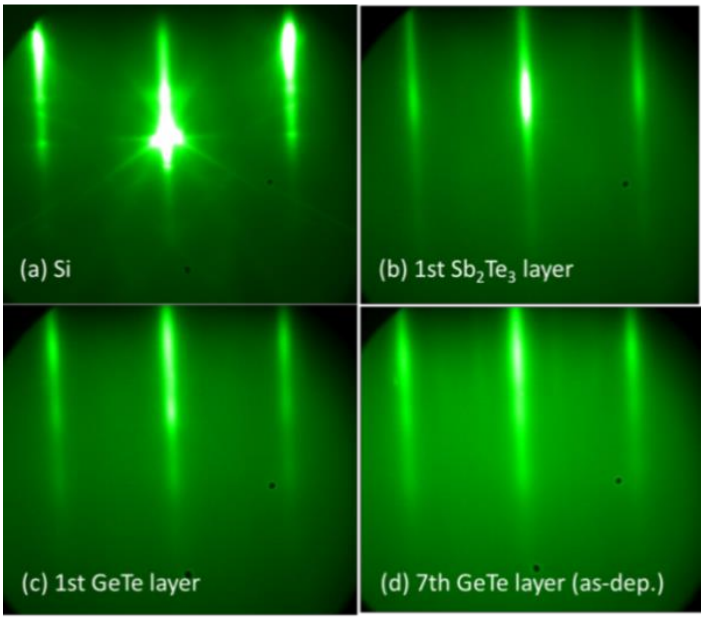

Fig. 6.1. RHEED patterns recorded before, during and after the growth of the exemplary GeTe-Sb_2Te_3 superlattice deposited at low substrate temperature of 140 °C. The RHEED patterns of (a) Si substrate, (b) the first (seeding) Sb_2Te_3 layer, and (c) the first and (d) the final (7th) GeTe layers, respectively, are shown. All the streaky patterns denote that each layer possesses a high surface crystallinity and it grows in two-dimensional growth mode even at a low temperature of 140°C.

Soon after the deposition of the Sb_2Te_3 seeding layer started, the RHEED pattern of the Si substrate gradually disappeared and was replaced by the RHEED pattern of the grown seeding Sb_2Te_3 layer, as seen in Fig. 6b, showing the typical RHEED pattern of the as-deposited Sb_2Te_3 seeding layer. This streaky RHEED patterns show that the Sb_2Te_3 layer grew in a two-dimensional growth mode, characterized by a smooth surface and high surface crystallinity.

The deposition of the next layers, i.e. the 1st GeTe, 2nd Sb_2Te_3, 2nd GeTe layers, etc. (for simplicity from now on called the high-order layers), took place at a certain substrate temperature, T_s, which was varied for each SL from 100 °C to 220 °C, see Section 4.1. For the first SL specimen, the high-order layers were deposited at 100 °C. The RHEED pattern of these layers show mainly diffused intensity distribution (not shown), indicating that the deposited high-order layers are predominantly amorphous. In contrast, starting at T_s = 120 °C the streaky RHEED patterns are observed for all high-order layers, denoting that at temperatures of 120 °C and above crystalline layers can be grown. Fig. 6.1c and d show the typical streaky RHEED patterns of the grown 1st GeTe and 7th GeTe layers, respectively, of the exemplary SL, in which the high-order layers were deposited at a low temperature of 140 °C. All the RHEED intensities show the streaky patterns revealing the high crystallinity and the smoothness of the layer surface during and after the growth. This result also characterizes the growth of all the deposited Sb_2Te_3 and GeTe layers to be in two-dimensional growth mode.

To summarize, crystalline GeTe and Sb_2Te_3 layers of the SL structure can be grown at substrate temperatures of 120 °C and above. The growth is characterized by a two-dimensional growth mode.

6.2. Crystallinity and topography

$2\theta - \omega$ XRD measurements were done to assess the structural properties of the as-deposited SLs. Fig. 6.2 shows $2\theta - \omega$ XRD scans of the SLs deposited at various substrate temperatures, from 120 °C to 220 °C. To assist the data interpretation, the dash-dot-lines are drawn in red, green and black colors, representing the expected Bragg reflections of the c-planes of trigonal Sb_2Te_3, low-temperature GeTe structure and trigonal GST225, respectively [100, 121, 127].

The first $2\theta - \omega$ pattern presented in Fig. 6.2 is that from the relatively thick GeTe/Sb_2Te_3/Si(111) film (see Subsection 4.1.1), presented in red color. The thicknesses of the GeTe and Sb_2Te_3 layers are ~15 and ~25 nm, respectively. These data are presented in order to give a first assistance for the Bragg reflection interpretation of the SL structures. As seen, all the Sb_2Te_3 and GeTe Bragg peaks can be discerned. This might also be because the layers are relatively thick, so that the potentially-occurring Sb_2Te_3-GeTe intermixing volume in the interface region is only a small part of the whole investigated volume and can be negligible in terms of diffraction sampling.

The SLs deposited at low substrate temperatures (T_s = 120 °C up to 160 °C; presented by green, navy blue, dark yellow and magenta colors, respectively) show Bragg peaks situated at almost identical 2θ positions. The peaks situated close to the expected (000*l*) Sb_2Te_3 reflections can be discerned. The peaks corresponding to (000*l*) GeTe reflections are occasionally discerned, e.g. at $2\theta = 25.8°$ for the film deposited at 145 °C, but not as intensive as those of Sb_2Te_3. This indicates that the GeTe and Sb_2Te_3 layers deposited at those low temperatures are in some extent still stably present (both layers not being totally intermixed with each other). This makes sense since the deposition temperatures are lower than those typically used for epitaxial growth of GeTe-Sb_2Te_3 SL structures, i.e. ≥ 220 °C, where intermixing naturally occurs during the growth [88, 95, 191, 206].

At higher temperatures, i.e. ≥ 160 °C, the situation is slightly different. At 190 °C (navy blue), the peak intensities of the Sb_2Te_3(000*l*) reflections, e.g. at $2\theta = 8.71°$ and $64.22°$ corresponding to the (0003) and (00021) reflections, respectively, are lower than those of SLs deposited at low temperatures. At even higher temperatures, i.e. 210 °C (brown) and 220 °C (black), several other peaks emerge. Those peaks fit closer to the expected t-GST225(000*l*) reflections. This result might denote the occurrence of possible intermixing layers between Sb_2Te_3 and GeTe during the deposition, resulting in nominal GST layers (building blocks). To summarize, this result might indicate that a more severe intermixing of GeTe layers and Sb_2Te_3 possibly occurs at the depositions of SL at higher temperatures.

The texture analysis was performed by measuring the pole figures of the SLs. Fig. 6.3 presents the corresponding pole figures of the exemplary SL specimen deposited at low temperature T_s = 140 °C. The figure shows the $Sb_2Te_3\{1\ 0\ \bar{1}\ 10\}$ (Fig. 6.3a) and the $GeTe\{10\overline{12}\}$ (Fig. 6.3b) pole figures measured at the corresponding Bragg angles of 38.45° and 29.88°, respectively. In Fig. 6.3a the pole density maxima are located at a polar angle $\alpha \approx 39°$ corresponding to $Sb_2Te_3\{1\ 0\ \bar{1}\ 10\}$ planes, while those in Fig. 6.3b are located at $\alpha \approx 58.4°$ confirming the reflections of $GeTe\{10\overline{12}\}$ planes. The measured pole density maxima in both Fig. 6.3a and b are arranged in six-fold rotation symmetry which shows the occurring of domain twinning, as typically observed in the epitaxial chalcogenide films. The presence of exclusively six pole density maxima (e.g. no ring-like intensity contributions intensities in between each two pole density maxima) in the pole figures also denotes that exclusively epitaxial SL structure grew although the deposition was at the significantly low temperature (140 °C) compared to the typical temperatures for depositing chalcogenide SLs [88, 95, 191, 206]. This result also confirms the RHEED data (see Section 6.1).

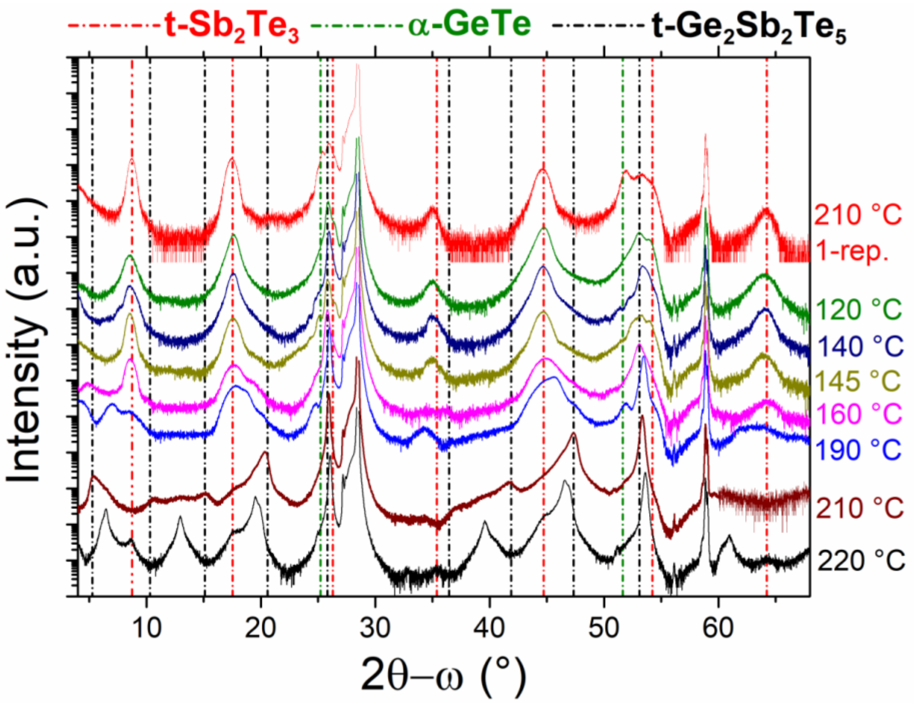

Fig. 6.2.The $2\theta - \omega$ XRD scans of GeTe-Sb_2Te_3 superlattice films, deposited at different substrate temperatures, as presented in different online colors. The red curve is the $2\theta - \omega$ XRD scan of the GeTe/Sb_2Te_3/Si(111) film.

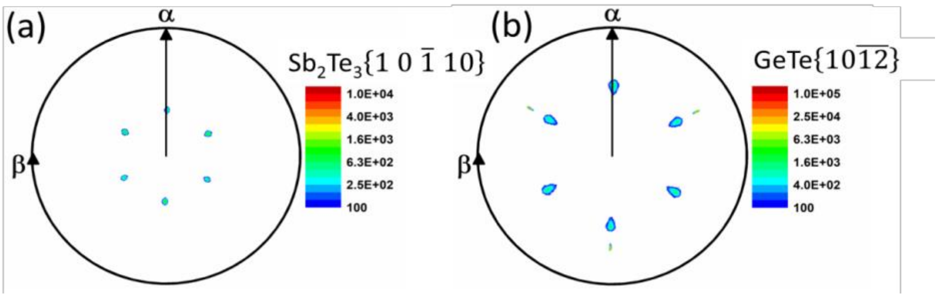

Fig. 6.3. $Sb_2Te_3\{1\,0\,\bar{1}\,10\}$ and $GeTe\{10\overline{12}\}$ pole figures of the SL structure, showing that it grew exclusively epitaxial at the low deposition temperature of 140 °C.

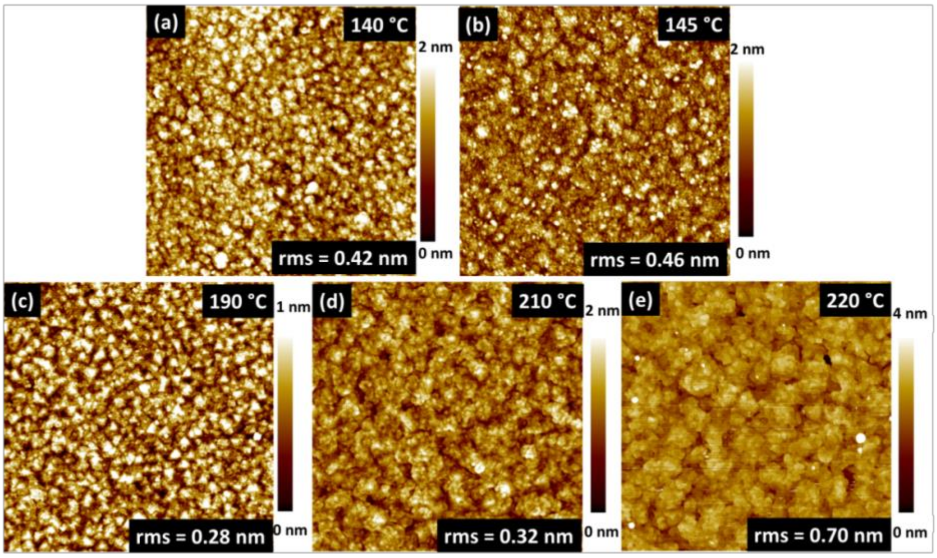

Fig. 6.4. AFM images of GeTe-Sb_2Te_3 SL structures deposited at different substrate temperatures, respectively. All the films are characterized by typical root mean square (RMS) values less than 1 nm, denoting a very smooth topography.

It can be concluded, also from the RHEED experiments, that the epitaxial window of GeTe-Sb_2Te_3 superlattice begins at temperatures as low as 120 °C, i.e. below which the thermal energy is too low for a nucleation to occur and hence the predominantly amorphous phase results. This result is also rather surprising as the typical epitaxial GeTe-Sb_2Te_3 SL, as mentioned previously, is usually grown at temperature of 220 °C or higher [88, 95, 191, 206].

The film topography of each SL was observed by means of AFM. Fig. 6.3 shows the measured AFM images of the SLs deposited from 140 to 220 °C. All the SL films exhibit rather unordered patterns topographically. However, in some occassions, e.g. in the case of the SL deposited at 190 °C (Fig. 6.4c), small tringular grains can be discerned. These triangularly shaped topographical patterns are however hardly observed on the other SLs deposited at other temperatures. Nonetheless, as presented, all the SLs show a relatively smooth topography, i.e. with root mean square (RMS) values are less than 1 nm. These results are in agreement with the streaky RHEED patterns of all the SL film sepecimens and they confirm the two-dimensional growth mode of GeTe-Sb_2Te_3 SL on Si(111).

6.3. Microstructure of GeTe-Sb_2Te_3 superlattice

It was already observed, e.g. by $2\theta - \omega$ XRD measurements, that the GeTe-Sb_2Te_3 layer intermixing more possibly occurs during the depositions of SLs especially at higher temperature region (above 160 °C). The observations of the local microstructures using advanced STEM is of importance to assess the physical stacking layers and the possible layer intermixing. In this section, the STEM investigations of SLs deposited at 140 °C and 145 °C are discussed. The two particular SLs attract more interests since they are epitaxially grown at temperatures which are significantly lower than the typical SL deposition temperatures [88, 95, 191, 206].

Fig. 6.5 shows a low-magnification HAADF-STEM image of the SL deposited at 140 °C. The microstructure of the SL deposited at 145 °C is commensurate with that of 140 °C. The mostly dark bottom region corresponds to Si(111) substrate since Si possesses a significantly lower Z number than that of Ge, Sb or Te (see subsection 4.2.4). The regions above the Si(111) substrate consists of the SL structure. The brighter and darker regions correspond to the Sb-rich and Ge-rich layers, respectively. From the image, the general trend can be clearly seen that the layer thickness is reduced across the SL. This inhomogeneity in the layer thickness is rather unexpected since each layer was deposited at the identical process parameters. This is probably due to an unavoidable contamination of the laser window when the depositions carried on.

More detailed information on the atomic ordering and a possible chemical intermixing can be explored by means of HAADF-STEM in high resolution. Fig. 6.6 presents an exemplary HAADF-STEM image of the selected regions in the SL, i.e. a region closer to the Si surface (Fig. 6.6a) and that closer to the SL surface (Fig. 6.6b). Each marking number at the right-hand side of each Fig. 6.6a and b denotes the number of Te-anion rows the corresponding building block is constructed of. It can be discerned that the SL consists of a stacking of Sb_2Te_3 (3-Te rows, see Section 5.2) and $Ge_{(x+y)}Sb_{(2-y)}Te_z$ ($z \geq 5$, see Subsection 5.1.2) building blocks intercalated by van der Waals gap. The SL region closer to the Si surface (Fig. 6.6a) contains $Ge_{(x+y)}Sb_{(2-y)}Te_z$ units with $z = 7, 8, 10$. Above 23 ± 3 nm (Fig. 6.6b), trigonal GST units are predominantly found with 5- or 6-Te rows, corresponding to GST225 and GST326, respectively. This might denote a stronger intermixing occurring at the outer region closer to the surface of the SL.

As also observed in Fig. 6.5, the layer interfaces in the SL are not totally sharp. This could also be due to a presence of bilayer stacking faults (BSF) present in the SLs, as typically also present in GST films [88, 178, 191]. One of the occurring BSFs is marked by a dash-lined rectangle in Fig. 6.6b.

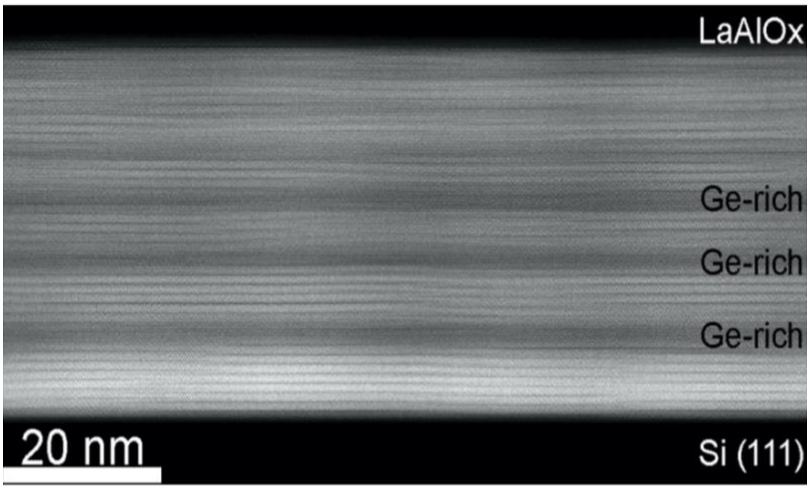

Fig. 6.5. Low-magnification HAADF-STEM image of a GeTe-Sb_2Te_3 SL deposited at 140 °C. The bright and dark regions denote Sb-rich and Ge-rich regions, respectively. The dark regions below and above the SL are the Si(111) substrate and the $LaAlO_x$ capping layer, respectively.

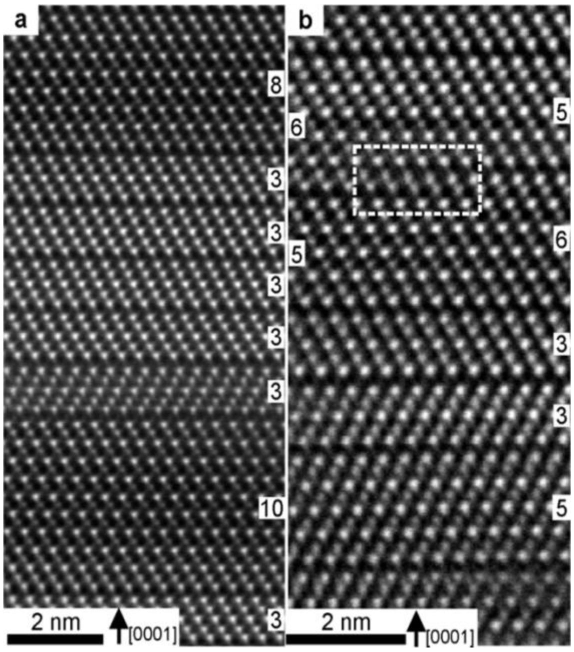

Fig. 6.6. HAADF-STEM image of (a) the bottom region (closer to the Si surface) and (b) adjacent upper region (closer to the SL surface). The structure is constructed of Sb_2Te_3 (3-Te rows) and $Ge_{(x+y)}Sb_{(2-y)}Te_z$ (≥ 5-Te rows) building blocks intercalated by quasi Van-der-Waals gaps. The dash-lined rectangle in (b) shows the presence of a bilayer stacking fault.

6.4. Summary

Depositions of GeTe-Sb_2Te_3 superlattice structures have been successfully done by means of PLD. By monitoring the growth of each layer of the SL and by observing the topographies of the as-deposited SL, it is revealed that the growth of Sb_2Te_3 and GeTe layers takes place in two-dimensional growth modes, which is prerequisite for the growth of a high quality SL. The lower margin of the epitaxial window is observed to be as low as 120 °C which is strikingly lower than the temperatures typically used for a growth of a chalcogenide superlattice structure (i.e. $T_s \geq 220$ °C). For deposition at higher deposition temperatures, GeTe-Sb_2Te_3 layer intermixing is more probable to occur than for that at lower temperatures. An even closer inspections of the nanostructures within the SL deposited at low temperature 140 °C revealed an inhomogeneity of individual layer thickness across the SL, wherein the layers tend to get thinner approaching the SL surface. A closer inspection on local atomic structure reveals that the SL is constructed of $Ge_{(x+y)}Sb_{(2-y)}Te_z$ and Sb_2Te_3 units, intercalated by Van der Waals gaps. For $Ge_{(x+y)}Sb_{(2-y)}Te_z$ building blocks, z varies across the SL, ranging from 5 to 10. $Ge_{(x+y)}Sb_{(2-y)}Te_z$ with $z \geq 7$ are characterized Ge-rich, in which pure GeTe layers are found in the bulk of the building blocks. This result also demonstrates the higher flexibility of PLD for obtaining chalcogenide SL structures with a controlled chemical intermixing.

Chapter VII
Summary and Outlook

4.1. Summary

Chalcogenide alloys within the binary line of GeTe-Sb_2Te_3 have been intensively investigated and employed as phase change materials for data memory media. A fabrication of thin chalcogenide films with a more ordered crystalline structure is necessitated in order to provide a platform for a deeper investigation on switching mechanism underlying the phase change phenomena. Moreover, the concept of chalcogenide superlattice (SL) structure is today of great interest as was shown to have improved switching characteristics. In this work, the growths of epitaxial $Ge_2Sb_2Te_3$ (GST225), GeTe and Sb_2Te_3 thin films as well as GeTe-Sb_2Te_3 superlattice structure on highly-mismatched Si(111) substrate have been successfully done by means of pulsed laser deposition (PLD). PLD proved for its versatility and flexibility in application and, at the same time, its simplicity in implementation which enables one to produce the high-quality epitaxial films as well as SLs. Thus, this work is divided into four parts, i.e. the fabrications of epitaxial chalcogenide films (GST225, Sb_2Te_3 and GeTe) and depositions of GeTe-Sb_2Te_3 SL structure.

1. All the alloys (GST225, Sb_2Te_3 and GeTe) were grown with in c-plane, i.e. (111) or (000*l*), out-of-plane orientation on Si(111).
2. Epitaxial GST225 films were grown on Si(111) in 2D-growth mode. Strongly (0001)-oriented polycrystalline films result from the deposition at substrate temperatures, T_s, of 170 °C, whereas the epitaxial window ranges from 200 °C to 300 °C. The increase of T_s leads to the improved crystalline quality with the expense of the decrease of deposition rate due to desorption. Epitaxial GST225 films can be grown with the deposition rate as high as 42 nm/min. The slight reduction of substrate-target distance from ~7.5 cm to ~6 cm implies on remarkable changes in film properties, e.g. a significant improvement in crystalline quality, the formation of a single alloy containing various structural phases, and the alteration of the in-plane epitaxial relationship. Also, by using the reduced distance at moderate T_s of 220 °C, the epitaxial GST225 thin films with heterogeneous vacancy structures (coexisting cubic phases. i.e. metastable rocksalt structure with random vacancy and metastable phase with ordered vacancies, and trigonal phase) can be produced. This provides a platform for phase transformation studies by thermal annealing (at 220 °C) which showed a phase transformation towards a pure trigonal phase. By a long-duration annealing process (7 h), a thin film with micron-sized GST225 grains can be realized, accompanied by the formation of building blocks with inhomogeneous numbers of Te-stackings.

3. The growths of epitaxial Sb_2Te_3 thin films in trigonal phase were achieved at T_s ranging between 140 and 280 °C. The optimum T_s in terms of deposition rate and film quality was determined to be at 240 °C. The film was also grown in 2D-growth mode, resulting in a smooth topography with roughness less than 1 nm (1 quintuple Sb_2Te_3 layer). The epitaxial growth of Sb_2Te_3 thin films is initiated by the self-organized formation of a Sb/Te single-atomic passivation layer on the Si surface forming so-called Van-der Waals (VdW) epitaxy, allowing that the grown lattice to be totally relaxed.
4. GeTe is considered as a 3D-bonded material. This might lead to a rather complex growth mode observed. It was revealed that the growth of GeTe was initialized by the formation of an ultra-thin amorphous layer. In general, and especially in the end of deposition process, the films were predominantly grown in the mix of 2D and 3D growth modes. By employing a 2D-bonded Sb_2Te_3 as a seeding layer on Si(111), the epitaxial window of GeTe can be extended especially towards the lower temperature regime, up to 145 °C. Additionally, the surface topography can be significantly improved with typical RMS of less than 1 nm, indicating that the films are grown in 2D growth mode on the buffered (i.e. Sb_2Te_3/Si(111)) substrate.
5. The depositions of GeTe-Sb_2Te_3 superlattices (SLs) have also been successfully done by PLD. By the use the first Sb_2Te_3 layer as a seeding layer, each layer of the SLs, i.e. Sb_2Te_3 and GeTe layer, was grown in 2D growth mode. The epitaxial SLs can be grown starting at T_s = 140 °C. The epitaxial window is strikingly lower than that previously were reported, i.e. (i.e. $T_s \geq$ 220 °C). Studies on local structure of 140 °C-deposited SL showed that the SL consists of Ge-rich $Ge_{(x+y)}Sb_{(2-y)}Te_z$ and Sb_2Te_3 units intercalated by vdW gaps with the inhomogeneity of layer thickness across the SL.

4.2. Outlook

Based on the existing issues in the present thesis and the current issues related to the applications in phase change data memory device, some outlooks can be drawn, which are presented as follows:

1. As mentioned, the change of target-substrate distance alters the resulting films properties. Thus, a thorough investigation on the influence of the change of target-substrate distance on the properties of epitaxial chalcogenide films is necessitated in order to map a complete picture of the influence of all the PLD parameters.
2. The PLD parameters for a deposition of purely-rocksalt phase of GST is also of interests since from the conventional point of view, the switching occurs between amorphous and rocksalt phases.
3. The quest for optimum PLD parameters for the growth of epitaxial SL structures of chalcogenide phase change materials is still present. This is based on the fact that the recent finding on the deposition of the superlattice

showed that there is an inhomogeneity of layer thicknesses in chalcogenide superlattice structure. The first preferable SL composition would be $(GeTe)_2$-$(Sb_2Te_3)_1$ with constant thickness of each layer, which is equivalent to nominal $Ge_2Sb_2Te_5$ thin film.

4. As stated previously, the layer intermixing naturally occurs during the growth of GeTe-Sb_2Te_3 SL structures. To overcome with the problem, the van der Waals based layer can be used as one component of a chalcogenide superlattice. Here, GST225 is the best option since, in its stable phase, it features van der Waals-type layered structure, the same feature with that of layered Sb_2Te_3, and in its low-energy metastable, it features vacancy layers. In conclusion, depositions of Sb_2Te_3-$Ge_2Sb_2Te_5$ SL structure are of interest.
5. The issue on layer intermixing in the GeTe-Sb_2Te_3 superlattice leads to an outlook for a deposition of off-stoichiometric material with an excess of Te atoms, such as $GeTe_2$, as one unit of SL, hence resulting $GeTe_2$-Sb_2Te_3 SL structures. By PLD, the outlook is feasible to realize since a stoichiometric transfer of the alloy target, instead of elemental effusion cell, can be achieved. It could be expected to provide a better control on chemical intermixing on the SL.
6. An investigation on the optical and electrical switching properties of pulsed laser deposited epitaxial chalcogenide films and the compositionally-equivalent SL structures is needed in order to explore the improvements of the pulsed laser deposited SLs.

Bibliography

1. Ostwald, W., *Studien über die Bildung und Umwandlung fester Körper.* Zeitschrift für physikalische Chemie, 1897. **22**(1): p. 289-330.
2. Kolobov, A.V., et al., *Vacancy-mediated three-center four-electron bonds in GeTe-Sb 2 Te 3 phase-change memory alloys.* Physical Review B, 2013. **87**(16): p. 165206.
3. Moore, G.E., *Cramming more components onto integrated circuits, Reprinted from Electronics, volume 38, number 8, April 19, 1965, pp. 114 ff.* IEEE Solid-State Circuits Society Newsletter, 2006. **20**(3): p. 33-35.
4. Chen, T.-c. *Challenges for silicon technology scaling in the Nanoscale Era*. in *ESSCIRC, 2009. ESSCIRC'09. Proceedings of*. 2009. IEEE.
5. Meena, J.S., et al., *Overview of emerging nonvolatile memory technologies.* Nanoscale research letters, 2014. **9**(1): p. 526.
6. Sarwat, S.G., *Materials science and engineering of phase change random access memory.* Materials Science and Technology, 2017. **33**(16): p. 1890-1906.
7. Lange, F.R.L., B.J. Kooi, and M. Wuttig, *Chalcogenide superlattices: growth, structure and applications*. 2016, Fachgruppe Physik.
8. Burr, G.W., et al., *Overview of candidate device technologies for storage-class memory.* IBM Journal of Research and Development, 2008. **52**(4.5): p. 449-464.
9. Wong, H.-S.P., et al., *Phase change memory.* Proceedings of the IEEE, 2010. **98**(12): p. 2201-2227.
10. Meijer, G., *Who wins the nonvolatile memory race?* Science, 2008. **319**(5870): p. 1625-1626.
11. Freitas, R.F. and W.W. Wilcke, *Storage-class memory: The next storage system technology.* IBM Journal of Research and Development, 2008. **52**(4.5): p. 439-447.
12. Ielmini, D. and A.L. Lacaita, *Phase change materials in non-volatile storage.* Materials Today, 2011. **14**(12): p. 600-607.
13. Hosseini, P., *Phase-Change and Carbon Based Materials for Advanced Memory and Computing Devices.* 2013.
14. Lee, S. and K. Kim, *Current development status and future challenges of ferroelectric random access memory technologies.* Japanese journal of applied physics, 2006. **45**(4S): p. 3189.
15. Slaughter, J., et al., *Fundamentals of MRAM technology.* Journal of superconductivity, 2002. **15**(1): p. 19-25.
16. Ielmini, D., *Resistive switching memories based on metal oxides: mechanisms, reliability and scaling.* Semiconductor Science and Technology, 2016. **31**(6): p. 063002.
17. Wuttig, M., *Phase-change materials: Towards a universal memory?* Nature materials, 2005. **4**(4): p. 265-266.
18. Raghavan, N., et al. *Stochastic variability of vacancy filament configuration in ultra-thin dielectric RRAM and its impact on OFF-state reliability*. in *Electron Devices Meeting (IEDM), 2013 IEEE International*. 2013. IEEE.
19. Morton, J.J., et al., *Solid-state quantum memory using the 31P nuclear spin.* Nature, 2008. **455**(7216): p. 1085-1088.
20. Rueckes, T., et al., *Carbon nanotube-based nonvolatile random access memory for molecular computing.* science, 2000. **289**(5476): p. 94-97.

21. Mojumder, N.N., et al., *Magnonic spin-transfer torque MRAM with low power, high speed, and error-free switching.* IEEE Transactions on Magnetics, 2012. **48**(6): p. 2016-2024.
22. Akiyama, T., et al., *Rewritable dual-layer phase-change optical disk utilizing a blue-violet laser.* Japanese Journal of Applied Physics, 2001. **40**(3S): p. 1598.
23. Narumi, K., et al., *Rewritable dual-layer phase-change optical disk with a balanced transmittance structure.* Japanese journal of applied physics, 2002. **41**(5R): p. 2925.
24. Ohta, T., et al., *Overview and the future of phase-change optical disk technology.* Japanese Journal of Applied Physics, 2000. **39**(2S): p. 770.
25. Yamada, N., et al., *High speed overwritable phase change optical disk material.* Japanese Journal of Applied Physics, 1987. **26**(S4): p. 61.
26. Tominaga, J., T. Nakano, and N. Atoda, *An approach for recording and readout beyond the diffraction limit with an Sb thin film.* Applied Physics Letters, 1998. **73**(15): p. 2078-2080.
27. Yamada, N., et al., *100 GB rewritable triple-layer optical disk having Ge-Sb-Te films.* Proc. E* PCOS, 2009. **2009**: p. 23-28.
28. Wuttig, M. and N. Yamada, *Phase-change materials for rewriteable data storage.* Nature materials, 2007. **6**(11): p. 824-832.
29. Hudgens, S. and B. Johnson, *Overview of phase-change chalcogenide nonvolatile memory technology.* MRS bulletin, 2004. **29**(11): p. 829-832.
30. Raoux, S., et al., *Phase-change random access memory: A scalable technology.* IBM Journal of Research and Development, 2008. **52**(4.5): p. 465-479.
31. Bruns, G., et al., *Nanosecond switching in GeTe phase change memory cells.* Applied Physics Letters, 2009. **95**(4): p. 043108.
32. Hosseini, P., et al., *Accumulation-based computing using phase-change memories with FET access devices.* IEEE Electron Device Letters, 2015. **36**(9): p. 975-977.
33. Loke, D., et al., *Ultrafast phase-change logic device driven by melting processes.* Proceedings of the National Academy of Sciences, 2014. **111**(37): p. 13272-13277.
34. Wright, C.D., P. Hosseini, and J.A.V. Diosdado, *Beyond von-Neumann Computing with Nanoscale Phase-Change Memory Devices.* Advanced Functional Materials, 2013. **23**(18): p. 2248-2254.
35. Shayduk, R. and W. Braun, *Epitaxial films for Ge–Sb–Te phase change memory.* Journal of Crystal Growth, 2009. **311**(7): p. 2215-2219.
36. Simpson, R., et al., *Interfacial phase-change memory.* Nature Nanotechnology, 2011. **6**(8): p. 501-505.
37. Ovshinsky, S.R., *Reversible electrical switching phenomena in disordered structures.* Physical Review Letters, 1968. **21**(20): p. 1450.
38. Adler, D., H.K. Henisch, and N. Mott, *The mechanism of threshold switching in amorphous alloys.* Reviews of Modern Physics, 1978. **50**(2): p. 209.
39. Buckley, W. and S. Holmberg, *Electrical characteristics and threshold switching in amorphous semiconductors.* Solid-State Electronics, 1975. **18**(2): p. 127IN3129-128IN4147.
40. Hughes, A., P. Holland, and A. Lettington, *Control of holding currents in amorphous threshold switches.* Journal of Non-Crystalline Solids, 1975. **17**(1): p. 89-99.
41. Kastner, M., *Bonding bands, lone-pair bands, and impurity states in chalcogenide semiconductors.* Physical Review Letters, 1972. **28**(6): p. 355.
42. Ovshinsky, S.R. and H. Fritzsche, *Amorphous semiconductors for switching, memory, and imaging applications.* IEEE Transactions on Electron Devices, 1973. **20**(2): p. 91-105.

43. Chen, M., K.A. Rubin, and R. Barton, *Compound materials for reversible, phase-change optical data storage.* Applied physics letters, 1986. **49**(9): p. 502-504.
44. Yamada, N., M. Takao, and M. Takenaga. *Te-Ge-Sn-Au Phase change recording film for optical disk*. in *30th Annual Technical Symposium*. 1987. International Society for Optics and Photonics.
45. Yamada, N., et al., *Rapid-phase transitions of GeTe-Sb2Te3 pseudobinary amorphous thin films for an optical disk memory.* Journal of Applied Physics, 1991. **69**(5): p. 2849-2856.
46. Yamada, N., *Erasable phase-change optical materials.* MRS Bulletin, 1996. **21**(9): p. 48-50.
47. Raoux, S., et al., *Phase change materials and phase change memory.* MRS bulletin, 2014. **39**(8): p. 703-710.
48. Micron Technology, I., *Micron Announces Availability of Phase Change Memory for Mobile Devices, Press Release.* July 12 2012.
49. Samsung Electronics Co., L., *Samsung Ships Industry's First Multi-chip Package with a PRAM Chip for Handsets, Press Release.* April 28 2010.
50. Ohmachi, N., et al., *High-speed recording media for HD DVD rewritable system.* Japanese journal of applied physics, 2006. **45**(2S): p. 1210.
51. Lee, C., T. Chin, and E. Huang, *Optical properties and structure of tellurium–germanium–bismuth–antimony compounds with fast phase-change capability.* Journal of Applied Physics, 2001. **89**(6): p. 3290-3294.
52. Kojima, R. and N. Yamada, *Acceleration of crystallization speed by Sn addition to Ge–Sb–Te phase-change recording material.* Japanese Journal of Applied Physics, 2001. **40**(10R): p. 5930.
53. Kato, T., et al., *The phase change optical disc with the data recording rate of 140 Mbps.* Japanese journal of applied physics, 2002. **41**(3S): p. 1664.
54. Wei, S., et al., *Phase change behavior in titanium-doped Ge 2 Sb 2 Te 5 films.* Applied Physics Letters, 2011. **98**(23): p. 231910.
55. Yao, D., et al., *Investigation on nitrogen-doped Ge 2 Sb 2 Te 5 material for phase-change memory application.* Solid-State Electronics, 2013. **79**: p. 138-141.
56. Dimitrov, D.Z., et al., *Oxygen and nitrogen co-doped GeSbTe thin films for phase-change optical recording.* Japanese journal of applied physics, 2002. **41**(3S): p. 1656.
57. Iwasaki, H., et al., *Completely erasable phase change optical disc II: Application of Ag-In-Sb-Te mixed-phase system for rewritable compact disc compatible with CD-velocity and double CD-velocity.* Japanese journal of applied physics, 1993. **32**(11S): p. 5241.
58. Jedema, F., *Phase-change materials: Designing optical media of the future.* Nature materials, 2007. **6**(2): p. 90-91.
59. Roß, U.H., *Structural investigation of Ge-Sb-Te thin films by aberration-corrected scanning transmission electron microscopy*. 2017, Christian-Albrechts Universität Kiel.
60. Salinga, M., *Phase change materials for non-volatile electronic memories*. 2008, Fachgruppe Physik.
61. Raoux, S., et al., *Direct observation of amorphous to crystalline phase transitions in nanoparticle arrays of phase change materials.* Journal of Applied Physics, 2007. **102**(9): p. 094305.
62. Loke, D., et al., *Breaking the speed limits of phase-change memory.* Science, 2012. **336**(6088): p. 1566-1569.

63. Burr, G.W., et al., *Phase change memory technology.* Journal of Vacuum Science & Technology B, Nanotechnology and Microelectronics: Materials, Processing, Measurement, and Phenomena, 2010. **28**(2): p. 223-262.
64. Chen, Y., et al. *Ultra-thin phase-change bridge memory device using GeSb*. in *Electron Devices Meeting, 2006. IEDM'06. International*. 2006. IEEE.
65. Wang, W., et al., *Fast phase transitions induced by picosecond electrical pulses on phase change memory cells.* Applied Physics Letters, 2008. **93**(4): p. 043121.
66. Raoux, S., *Phase change materials.* Annual Review of Materials Research, 2009. **39**: p. 25-48.
67. Van Pieterson, L., et al., *Phase-change recording materials with a growth-dominated crystallization mechanism: A materials overview.* Journal of Applied Physics, 2005. **97**(8): p. 083520.
68. Horii, H., et al. *A novel cell technology using N-doped GeSbTe films for phase change RAM*. in *VLSI Technology, 2003. Digest of Technical Papers. 2003 Symposium on*. 2003. IEEE.
69. Lai, S. and T. Lowrey. *OUM-A 180 nm nonvolatile memory cell element technology for stand alone and embedded applications*. in *Electron Devices Meeting, 2001. IEDM'01. Technical Digest. International*. 2001. IEEE.
70. Ielmini, D., et al., *Analysis of phase distribution in phase-change nonvolatile memories.* IEEE Electron Device Letters, 2004. **25**(7): p. 507-509.
71. Ielmini, D., et al., *Switching and programming dynamics in phase-change memory cells.* Solid-State Electronics, 2005. **49**(11): p. 1826-1832.
72. Pirovano, A., et al., *Low-field amorphous state resistance and threshold voltage drift in chalcogenide materials.* IEEE Transactions on Electron Devices, 2004. **51**(5): p. 714-719.
73. Lankhorst, M.H., B.W. Ketelaars, and R.A. Wolters, *Low-cost and nanoscale non-volatile memory concept for future silicon chips.* Nature materials, 2005. **4**(4): p. 347-352.
74. Russo, U., et al., *Modeling of programming and read performance in phase-change memories—Part I: Cell optimization and scaling.* IEEE transactions on electron devices, 2008. **55**(2): p. 506-514.
75. Grosse, K.L., et al., *Direct observation of nanometer-scale Joule and Peltier effects in phase change memory devices.* Applied Physics Letters, 2013. **102**(19): p. 193503.
76. Nirschl, T., et al. *Write strategies for 2 and 4-bit multi-level phase-change memory*. in *Electron Devices Meeting, 2007. IEDM 2007. IEEE International*. 2007. IEEE.
77. Gill, M., T. Lowrey, and J. Park. *Ovonic unified memory-a high-performance nonvolatile memory technology for stand-alone memory and embedded applications*. in *Solid-State Circuits Conference, 2002. Digest of Technical Papers. ISSCC. 2002 IEEE International*. 2002. IEEE.
78. Kolobov, A.V., et al., *Understanding the phase-change mechanism of rewritable optical media.* Nature materials, 2004. **3**(10): p. 703-708.
79. Akola, J., et al., *Experimentally constrained density-functional calculations of the amorphous structure of the prototypical phase-change material Ge 2 Sb 2 Te 5.* Physical Review B, 2009. **80**(2): p. 020201.
80. Krbal, M., et al., *Intrinsic complexity of the melt-quenched amorphous Ge 2 Sb 2 Te 5 memory alloy.* Physical Review B, 2011. **83**(5): p. 054203.
81. Huang, B. and J. Robertson, *Bonding origin of optical contrast in phase-change memory materials.* Physical Review B, 2010. **81**(8): p. 081204.

82. Shportko, K., et al., *Resonant bonding in crystalline phase-change materials.* Nature materials, 2008. **7**(8): p. 653-658.
83. Gaspard, J.-P., et al., *Peierls instabilities in covalent structures I. Electronic structure, cohesion and the Z= 8–N rule.* Philosophical Magazine B, 1998. **77**(3): p. 727-744.
84. Kolobov, A., et al., *Distortion-triggered loss of long-range order in solids with bonding energy hierarchy.* Nature chemistry, 2011. **3**(4): p. 311-316.
85. Siegrist, T., et al., *Disorder-induced localization in crystalline phase-change materials.* Nature materials, 2011. **10**(3).
86. Nam, S.-W., et al., *Electrical wind force–driven and dislocation-templated amorphization in phase-change nanowires.* Science, 2012. **336**(6088): p. 1561-1566.
87. Chong, T., et al., *Phase change random access memory cell with superlattice-like structure.* Applied physics letters, 2006. **88**(12): p. 122114.
88. Momand, J., et al., *Interface formation of two-and three-dimensionally bonded materials in the case of GeTe–Sb 2 Te 3 superlattices.* Nanoscale, 2015. **7**(45): p. 19136-19143.
89. Chong, T., et al., *Crystalline amorphous semiconductor superlattice.* Physical review letters, 2008. **100**(13): p. 136101.
90. Tominaga, J., et al., *Ferroelectric Order Control of the Dirac-Semimetal Phase in GeTe-Sb2Te3 Superlattices.* Advanced Materials Interfaces, 2014. **1**(1).
91. Tominaga, J., et al., *Giant multiferroic effects in topological GeTe-Sb2Te3 superlattices.* Science and technology of advanced materials, 2015. **16**(1): p. 014402.
92. Ohyanagi, T., et al., *GeTe sequences in superlattice phase change memories and their electrical characteristics.* Applied Physics Letters, 2014. **104**(25): p. 252106.
93. Kooi, B. and J.T.M. De Hosson, *Electron diffraction and high-resolution transmission electron microscopy of the high temperature crystal structures of Ge x Sb 2 Te 3+ x (x= 1, 2, 3) phase change material.* Journal of applied physics, 2002. **92**(7): p. 3584-3590.
94. Yu, X. and J. Robertson, *Modeling of switching mechanism in GeSbTe chalcogenide superlattices.* Scientific reports, 2015. **5**.
95. Wang, R., et al., *Intermixing during epitaxial growth of van der Waals bonded nominal GeTe/Sb2Te3 superlattices.* Crystal Growth & Design, 2016. **16**(7): p. 3596-3601.
96. Tominaga, J., et al., *Role of Ge switch in phase transition: Approach using atomically controlled GeTe/Sb2Te3 superlattice.* Japanese Journal of Applied Physics, 2008. **47**(7S1): p. 5763.
97. Thelander, E., et al., *Epitaxial growth of Ge-Sb-Te films on KCl by high deposition rate pulsed laser deposition.* Journal of Applied Physics, 2014. **115**(21): p. 213504.
98. Thelander, E., et al., *Low temperature epitaxy of Ge-Sb-Te films on BaF2 (111) by pulsed laser deposition.* Applied Physics Letters, 2014. **105**(22): p. 221908.
99. Perumal, K., *Epitaxial growth of Ge-Sb-Te based phase change materials*. 2013, Humboldt-Universität zu Berlin, Mathematisch-Naturwissenschaftliche Fakultät I.
100. Matsunaga, T., N. Yamada, and Y. Kubota, *Structures of stable and metastable Ge2Sb2Te5, an intermetallic compound in GeTe–Sb2Te3 pseudobinary systems.* Acta Crystallographica Section B: Structural Science, 2004. **60**(6): p. 685-691.
101. Nonaka, T., et al., *Crystal structure of GeTe and Ge 2 Sb 2 Te 5 meta-stable phase.* Thin Solid Films, 2000. **370**(1): p. 258-261.

102. Yamada, N. and T. Matsunaga, *Structure of laser-crystallized Ge 2 Sb 2+ x Te 5 sputtered thin films for use in optical memory.* Journal of Applied Physics, 2000. **88**(12): p. 7020-7028.
103. Kojima, R., et al., *Nitrogen doping effect on phase change optical disks.* Japanese journal of applied physics, 1998. **37**(4S): p. 2098.
104. Friedrich, I., et al., *Structural transformations of Ge 2 Sb 2 Te 5 films studied by electrical resistance measurements.* Journal of Applied Physics, 2000. **87**(9): p. 4130-4134.
105. Kolobov, A.V., et al., *Why phase-change media are fast and stable: a new approach to an old problem.* Japanese journal of applied physics, 2005. **44**(5S): p. 3345.
106. Park, Y., et al., *Crystal structure and atomic arrangement of the metastable Ge 2 Sb 2 Te 5 thin films deposited on SiO 2⁄ Si substrates by sputtering method.* Journal of applied physics, 2005. **97**(9): p. 093506.
107. Da Silva, J.L., A. Walsh, and H. Lee, *Insights into the structure of the stable and metastable (GeTe) m (Sb 2 Te 3) n compounds.* Physical Review B, 2008. **78**(22): p. 224111.
108. Eom, J.-H., et al., *Global and local structures of the Ge-Sb-Te ternary alloy system for a phase-change memory device.* Physical Review B, 2006. **73**(21): p. 214202.
109. Sun, Z., J. Zhou, and R. Ahuja, *Structure of phase change materials for data storage.* Physical Review Letters, 2006. **96**(5): p. 055507.
110. Kooi, B., W. Groot, and J.T.M. De Hosson, *In situ transmission electron microscopy study of the crystallization of Ge 2 Sb 2 Te 5.* Journal of Applied Physics, 2004. **95**(3): p. 924-932.
111. Morales-Sanchez, E., et al., *Structural, electric and kinetic parameters of ternary alloys of GeSbTe.* Thin Solid Films, 2005. **471**(1-2): p. 243-247.
112. Lotnyk, A., et al., *Real-space imaging of atomic arrangement and vacancy layers ordering in laser crystallised Ge2Sb2Te5 phase change thin films.* Acta Materialia, 2016. **105**: p. 1-8.
113. Zhang, B., et al., *Vacancy structures and melting behavior in rock-salt GeSbTe.* Scientific reports, 2016. **6**: p. 25453.
114. Urban, P., et al., *Temperature dependent resonant X-ray diffraction of single-crystalline Ge 2 Sb 2 Te 5.* CrystEngComm, 2013. **15**(24): p. 4823-4829.
115. Lotnyk, A., et al., *Local atomic arrangements and lattice distortions in layered Ge-Sb-Te crystal structures.* Scientific reports, 2016. **6**: p. 26724.
116. Bragaglia, V., et al., *Metal-insulator transition driven by vacancy ordering in GeSbTe phase change materials.* Scientific reports, 2016. **6**: p. 23843.
117. Kolobov, A.V. and J. Tominaga, *Chalcogenides: Metastability and Phase Change Phenomena*. Vol. 164. 2012: Springer Science & Business Media.
118. Wuttig, M., et al., *The role of vacancies and local distortions in the design of new phase-change materials.* Nature materials, 2007. **6**(2): p. 122-128.
119. Venkatasubramanian, R., et al., *Thin-film thermoelectric devices with high room-temperature figures of merit.* Nature, 2001. **413**(6856): p. 597.
120. Baily, S. and D. Emin, *Transport properties of amorphous antimony telluride.* Physical Review B, 2006. **73**(16): p. 165211.
121. Anderson, T.L. and H.B. Krause, *Refinement of the Sb2Te3 and Sb2Te2Se structures and their relationship to nonstoichiometric Sb2Te3− ySey compounds.* Acta Crystallographica Section B: Structural Crystallography and Crystal Chemistry, 1974. **30**(5): p. 1307-1310.

122. Koma, A., *Van der Waals epitaxy—a new epitaxial growth method for a highly lattice-mismatched system.* Thin Solid Films, 1992. **216**(1): p. 72-76.
123. Hilmi, I., et al., *Research Update: Van-der-Waals epitaxy of layered chalcogenide Sb2Te3 thin films grown by pulsed laser deposition.* APL Materials, 2017. **5**(5): p. 050701.
124. Geim, A.K. and I.V. Grigorieva, *Van der Waals heterostructures.* Nature, 2013. **499**(7459): p. 419-425.
125. Zhang, W., et al., *Role of vacancies in metal–insulator transitions of crystalline phase-change materials.* Nature materials, 2012. **11**(11): p. 952.
126. Zhao, J., et al., *Pressure-induced disordered substitution alloy in Sb2Te3.* Inorganic chemistry, 2011. **50**(22): p. 11291-11293.
127. Bauer Pereira, P., et al., *Lattice dynamics and structure of GeTe, SnTe and PbTe.* physica status solidi (b), 2013. **250**(7): p. 1300-1307.
128. Shelimova, L., et al., *Crystal Structure, Phase Transitions, and Mechanical Properties of GeTe-Based Solid Solutions in the GeTe-PbTe-MTe Systems (M= Mn, Sc, La).* Inorganic Materials, 1993. **29**(11): p. 1291-1298.
129. Chattopadhyay, T. and J. Boucherle, *Neutron diffraction study on the structural phase transition in GeTe.* Journal of Physics C: Solid State Physics, 1987. **20**(10): p. 1431.
130. Matsunaga, T., et al., *Single structure widely distributed in a GeTe− Sb2Te3 pseudobinary system: a rock salt structure is retained by intrinsically containing an enormous number of vacancies within its crystal.* Inorganic chemistry, 2006. **45**(5): p. 2235-2241.
131. Bahl, S. and K. Chopra, *Amorphous versus crystalline GeTe films. III. Electrical properties and band structure.* Journal of Applied Physics, 1970. **41**(5): p. 2196-2212.
132. Rabe, K. and J. Joannopoulos, *Theory of the structural phase transition of GeTe.* Physical Review B, 1987. **36**(12): p. 6631.
133. Steigmeier, E. and G. Harbeke, *Soft phonon mode and ferroelectricity in GeTe.* Solid State Communications, 1970. **8**(16): p. 1275-1279.
134. Fons, P., et al., *Phase transition in crystalline GeTe: Pitfalls of averaging effects.* Physical Review B, 2010. **82**(15): p. 155209.
135. Waldecker, L., et al., *Time-domain separation of optical properties from structural transitions in resonantly bonded materials.* Nature materials, 2015. **14**(10): p. 991-995.
136. Wang, R., et al., *Ordered Peierls distortion prevented at growth onset of GeTe ultra-thin films.* Scientific reports, 2016. **6**: p. 32895.
137. Wang, R., et al., *Formation of resonant bonding during growth of ultrathin GeTe films.* NPG Asia Materials, 2017. **9**(6): p. e396.
138. Giussani, A., et al., *On the epitaxy of germanium telluride thin films on silicon substrates.* physica status solidi (b), 2012. **249**(10): p. 1939-1944.
139. Matsunaga, T., et al., *Structural characteristics of GeTe-rich GeTe–Sb 2 Te 3 pseudobinary metastable crystals.* Journal of Applied Physics, 2008. **103**(9): p. 093511.
140. Ashfold, M.N., et al., *Pulsed laser ablation and deposition of thin films.* Chemical Society Reviews, 2004. **33**(1): p. 23-31.
141. Eason, R., *Pulsed laser deposition of thin films: applications-led growth of functional materials*. 2007: John Wiley & Sons.
142. Braun, W., et al., *Epitaxy of Ge–Sb–Te phase-change memory alloys.* Applied Physics Letters, 2009. **94**(4): p. 041902.

143. Chrisey, D.B. and G.K. Hubler, *Pulsed laser deposition of thin films.* 1994.

144. Jackson, T. and S. Palmer, *Oxide superconductor and magnetic metal thin film deposition by pulsed laser ablation: a review.* Journal of Physics D: Applied Physics, 1994. **27**(8): p. 1581.

145. Shkurmanov, A., et al., *Low-Temperature PLD-Growth of Ultrathin ZnO Nanowires by Using Zn x Al 1− x O and Zn x Ga 1− x O Seed Layers.* Nanoscale research letters, 2017. **12**(1): p. 134.

146. Brodoceanu, D., et al., *Pulsed laser deposition of oxide thin films*, in *Plasma Production By Laser Ablation*. 2004, World Scientific. p. 41-46.

147. Ohnishi, T., H. Koinuma, and M. Lippmaa, *Pulsed laser deposition of oxide thin films.* Applied surface science, 2006. **252**(7): p. 2466-2471.

148. Wu, X., et al., *Epitaxial ordering of oxide superconductor thin films on (100) SrTiO3 prepared by pulsed laser evaporation.* Applied physics letters, 1987. **51**(11): p. 861-863.

149. Lorenz, M., et al., *Two-dimensional Frank–van-der-Merwe growth of functional oxide and nitride thin film superlattices by pulsed laser deposition.* Journal of Materials Research, 2017. **32**(21): p. 3936-3946.

150. Lu, Y., et al., *Ion-assisted pulsed laser deposition of aluminum nitride thin films.* Journal of applied physics, 2000. **87**(3): p. 1540-1542.

151. Doll, G., et al., *Growth and characterization of epitaxial cubic boron nitride films on silicon.* Physical Review B, 1991. **43**(8): p. 6816.

152. Nelea, V., et al., *Pulsed laser deposition of hydroxyapatite thin films on Ti-5Al-2.5 Fe substrates with and without buffer layers.* Applied Surface Science, 2000. **168**(1-4): p. 127-131.

153. Cotell, C.M., et al., *Pulsed laser deposition of hydroxylapatite thin films on Ti-6Al-4V.* Journal of Applied Biomaterials, 1992. **3**(2): p. 87-93.

154. Hansen, S. and T. Robitaille, *Formation of polymer films by pulsed laser evaporation.* Applied physics letters, 1988. **52**(1): p. 81-83.

155. Donley, M., et al., *Deposition and properties of MoS2 thin films grown by pulsed laser evaporation.* Surface and Coatings Technology, 1988. **36**(1-2): p. 329-340.

156. Cheung, J., et al., *HgTe and CdTe epitaxial layers and HgTe–CdTe superlattices grown by laser molecular beam epitaxy.* Journal of Vacuum Science & Technology A: Vacuum, Surfaces, and Films, 1986. **4**(4): p. 2086-2090.

157. Tsafack, T., et al., *Electronic, optical and thermal properties of the hexagonal and rocksalt-like Ge2Sb2Te5 chalcogenide from first-principle calculations.* Journal of Applied Physics, 2011. **110**(6): p. 063716.

158. Kim, M. and H. Kim, *Preparation and observation of an artifact-free Ge 2 Sb 2 Te 5 TEM specimen by the small angle cleavage technique.* Materials characterization, 2006. **56**(3): p. 245-249.

159. Hilmi, I., et al., *Epitaxial Ge 2 Sb 2 Te 5 films on Si (111) prepared by pulsed laser deposition.* Thin Solid Films, 2016. **619**: p. 81-85.

160. Houška, J., et al., *Laser desorption time-of-flight mass spectrometry of atomic switch memory Ge2Sb2Te5 bulk materials and its thin films.* Rapid Communications in Mass Spectrometry, 2014. **28**(7): p. 699-704.

161. KERN, F., *Cleaning solutions based on hydrogen peroxide for use in silicon semiconducto technology.* RCARev., 1970. **31**: p. 187.

162. Cullity, B.D., *Elements of X-ray Diffraction.* 2001.

163. Nagao, K. and E. Kagami, *X-ray thin film measurement techniques VII. Pole figure measurement.* The Rigaku Journal, 2011. **27**(2): p. 6-14.

164. Kobayashi, S. and K. Inaba, *X-ray thin-film measurement techniques.* mass spectroscopy equipped with a skimmer-type interface, 2012: p. 8.
165. Thelander, E., *Epitaxial Ge-Sb-Te Thin Films by Pulsed Laser Deposition*. 2014.
166. RayFleX.
167. O'Connor, D.J., B.A. Sexton, and R.S. Smart, *Surface analysis methods in materials science*. Vol. 23. 2013: Springer Science & Business Media.
168. Braun, W., *Applied RHEED: reflection high-energy electron diffraction during crystal growth*. Vol. 154. 1999: Springer Science & Business Media.
169. Egerton, R.F., *Physical principles of electron microscopy*. 2005: Springer.
170. Lotnyk, A., et al., *Focused high-and low-energy ion milling for TEM specimen preparation.* Microelectronics reliability, 2015. **55**(9): p. 2119-2125.
171. Stadelmann, P., *EMS-a software package for electron diffraction analysis and HREM image simulation in materials science.* Ultramicroscopy, 1987. **21**(2): p. 131-145.
172. Barthel, J., *Dr. Probe-STEM simulation software*.
173. A., C.C.D.S., *CaRIne Crystallography Divergent S. A.*
174. Zhong, Q., et al., *Fractured polymer/silica fiber surface studied by tapping mode atomic force microscopy.* Surface Science Letters, 1993. **290**(1-2): p. L688-L692.
175. Eaton, P. and P. West, *Atomic force microscopy*. 2010: Oxford University Press.
176. Bragaglia, V., et al., *Structural change upon annealing of amorphous GeSbTe grown on Si (111).* Journal of Applied Physics, 2014. **116**(5): p. 054913.
177. Freund, L.B. and S. Suresh, *Thin film materials: stress, defect formation and surface evolution*. 2004: Cambridge University Press.
178. Ross, U., et al., *Microstructure evolution in pulsed laser deposited epitaxial Ge-Sb-Te chalcogenide thin films.* Journal of Alloys and Compounds, 2016. **676**: p. 582-590.
179. Grey, F. and J. Bohr, *A symmetry principle for epitaxial rotation.* EPL (Europhysics Letters), 1992. **18**(8): p. 717.
180. Narayan, J. and B. Larson, *Domain epitaxy: A unified paradigm for thin film growth.* Journal of Applied Physics, 2003. **93**(1): p. 278-285.
181. Ross, U., et al., *Direct imaging of crystal structure and defects in metastable Ge2Sb2Te5 by quantitative aberration-corrected scanning transmission electron microscopy.* Applied Physics Letters, 2014. **104**(12): p. 121904.
182. Zhang, B., et al., *Element-resolved atomic structure imaging of rocksalt Ge2Sb2Te5 phase-change material.* Applied Physics Letters, 2016. **108**(19): p. 191902.
183. Dirisaglik, F., et al., *High speed, high temperature electrical characterization of phase change materials: metastable phases, crystallization dynamics, and resistance drift.* Nanoscale, 2015. **7**(40): p. 16625-16630.
184. Zhou, X., et al., *Phase-Change Memory Materials by Design: A Strain Engineering Approach.* Advanced Materials, 2016. **28**(15): p. 3007-3016.
185. Lanius, M., et al., *Topography and structure of ultrathin topological insulator Sb2Te3 films on Si (111) grown by means of molecular beam epitaxy.* Journal of Crystal Growth, 2016. **453**: p. 158-162.
186. Lanius, M., et al., *P–N junctions in ultrathin topological insulator Sb2Te3/Bi2Te3 heterostructures grown by molecular beam epitaxy.* Crystal Growth & Design, 2016. **16**(4): p. 2057-2061.
187. Hilmi, I., et al., *Epitaxial formation of cubic and trigonal Ge-Sb-Te thin films with heterogeneous vacancy structures.* Materials & Design, 2017. **115**: p. 138-146.

188. Andrieu, S., *Sb adsorption on Si< 111> analyzed by ellipsometry and reflection high-energy electron diffraction: Consequences for Sb doping in Si molecular-beam epitaxy.* Journal of applied physics, 1991. **69**(3): p. 1366-1370.
189. Boschker, J.E., et al., *Surface reconstruction-induced coincidence lattice formation between two-dimensionally bonded materials and a three-dimensionally bonded substrate.* Nano letters, 2014. **14**(6): p. 3534-3538.
190. Zhang, G., et al., *Quintuple-layer epitaxy of thin films of topological insulator Bi 2 Se 3.* Applied Physics Letters, 2009. **95**(5): p. 053114.
191. Momand, J., et al., *Atomic stacking and van-der-Waals bonding in GeTe–Sb 2 Te 3 superlattices.* Journal of Materials Research, 2016. **31**(20): p. 3115-3124.
192. Feng, P. and M. Sajjad, *Few-atomic-layer boron nitride sheets syntheses and applications for semiconductor diodes.* Materials Letters, 2012. **89**: p. 206-208.
193. Mahjouri-Samani, M., et al., *Pulsed Laser Deposition of Photoresponsive Two-Dimensional GaSe Nanosheet Networks.* Advanced Functional Materials, 2014. **24**(40): p. 6365-6371.
194. Serna, M.I., et al., *Large-area deposition of MoS2 by pulsed laser deposition with in situ thickness control.* ACS nano, 2016. **10**(6): p. 6054-6061.
195. Yang, Z. and J. Hao, *Progress in pulsed laser deposited two-dimensional layered materials for device applications.* Journal of Materials Chemistry C, 2016. **4**(38): p. 8859-8878.
196. Wang, G., et al., *Atomically smooth ultrathin films of topological insulator Sb 2 Te 3.* Nano Research, 2010. **3**(12): p. 874-880.
197. Bang, D., et al., *Mirror-symmetric magneto-optical kerr rotation using visible light in [(GeTe) 2 (Sb2Te3) 1] n topological superlattices.* Scientific reports, 2014. **4**.
198. Lotnyk, A., et al., *Van der Waals interfacial bonding and intermixing in GeTe-Sb2Te3-based superlattices.* Nano Research, 2017: p. 1-11.
199. Wang, R., et al., *Toward truly single crystalline GeTe films: The relevance of the substrate surface.* The Journal of Physical Chemistry C, 2014. **118**(51): p. 29724-29730.
200. Ostwald, W., *Studies on the Formation and Change of Solid Matter.* Z. Phys. Chem., 1897. **22**: p. 289-302.
201. Boschker, J.E. and R. Calarco, *Growth of crystalline phase change materials by physical deposition methods.* Advances in Physics: X, 2017. **2**(3): p. 675-694.
202. Zhou, G.-F. and B.A. Jacobs, *High performance media for phase change optical recording.* Japanese journal of applied physics, 1999. **38**(3S): p. 1625.
203. Saito, Y., et al., *Self-organized van der Waals epitaxy of layered chalcogenide structures.* physica status solidi (b), 2015. **252**(10): p. 2151-2158.
204. Simpson, R., et al., *Enhanced crystallization of GeTe from an Sb2Te3 template.* Applied Physics Letters, 2012. **100**(2): p. 021911.
205. Hrkac, V., et al., *Superposition twinning supported by texture in ZnO nanospikes.* Journal of Applied Crystallography, 2013. **46**(2): p. 396-403.
206. Casarin, B., et al., *Revisiting the local structure in Ge-Sb-Te based chalcogenide superlattices.* Scientific reports, 2016. **6**: p. 22353.
207. Kalikka, J., et al., *Strain-engineered diffusive atomic switching in two-dimensional crystals*, Nature communications 7, 2016: 11983.

List of Publications

Peer reviewed papers

1. Lotnyk, A.; Dankwort, T., Hilmi, I., Kienle, L., Rauschenbach, B., *Atomic-scale observation of defects motion in van der Waals layered chalcogenide based materials,* under review in Acta Materialia
2. Hilmi, I., Lotnyk. A., Gerlach, J., Schumacher, P., Rauschenbach, B., *Influence of substrate dimensionality on the growth mode of epitaxial 3D-bonded GeTe thin films: From 3D to 2D growth,* under review in Materials & design.
3. Behrens, M., Lotnyk, A., Gerlach, J. W., Hilmi, I., Abel, T., Lorenz, P., & Rauschenbach, B. Ultrafast interfacial transformation from 2D-to 3D-bonded structures in layered Ge–Sb–Te thin films and heterostructures. Nanoscale, *10*(48), 2018, p22946-22953.
4. Lotnyk, A., Ross, U., Dankwort, T., Hilmi, I., Kienle, L., Rauschenbach, B., *Atomic structure and dynamic reconfiguration of layered defects in van der Waals layered Ge-Sb-Te based materials*. Acta Materialia; 141, 2017, 92-96, DOI: 10.1016/j.actamat.2017.09.012.
5. Lotnyk, A., Hilmi, I., Ross, U., Rauschenbach, B., *Van der Waals interfacial bonding and intermixing in GeTe-Sb_2Te_3-based superlattices*. Nano Research 08/2017, DOI:10.1007/s12274-017-1785-y
6. Hilmi, I., Lotnyk. A., Gerlach, J., Schumacher, P., Rauschenbach, B., *Research Update: Van-der-Waals epitaxy of layered chalcogenide Sb_2Te_3 thin films grown by pulsed laser deposition*. APL Materials, 05/2017; 5(5):050701., DOI:10.1063/1.4983403
7. Hilmi, I., Lotnyk. A., Gerlach, J., Schumacher, P., Rauschenbach, B., *Epitaxial formation of cubic and trigonal Ge-Sb-Te thin films with heterogeneous vacancy structures*. Materials & design, 02/2017; 115:138-146., DOI:10.1016/j.matdes.2016.11.003
8. Hilmi, I., Thelander, E., Gerlach, J., Rauschenbach, B., *Epitaxial $Ge_2Sb_2Te_5$ Films on Si(111) prepared by Pulsed Laser Deposition*. Thin Solid Films 10/2016; 619., DOI:10.1016/j.tsf.2016.10.028

Conference Proceedings

1. Lotnyk, A., Ross, U., Hilmi, I., et al., *Formation and direct imaging of heterogeneous vacancy structures in cubic $Ge_2Sb_2Te_5$ crystal lattices*, Paper Nr. 4.5, European Phase Change and Ovonic Symposium, Cambridge, UK, 04.-06.09. (2016) 86-87.

Conference Contributions

- Hilmi, I. et al., poster, *Two-dimensional growth of three-dimensionally bonded GeTe,* German Physical Society (DPG) Spring Meeting, Berlin, Germany, Spring 2018.
- Hilmi, I., invited talk, *Fabrication of epitaxial chalcogenide thin films by pulsed laser deposition for application in non-volatile data memory,* Energy

Materials and Nanotechnology (EMN) Meeting on Epitaxy, Barcelona, Spain, Autumn 2017.

- Hilmi, I., et al., poster, *Pulsed laser deposition of epitaxial layered chalcogenide* Sb_2Te_3 *thin films on Si(111)*, DPG Spring Meeting, Dresden, Germany, Spring 2017.
- Hilmi, I., et al., poster, *Epitaxial growth of GeTe phase change alloy on Si(111) substrate by pulsed laser deposition*, DPG Spring Meeting, Dresden, Germany, Spring 2017.
- Hilmi, I., et al., talk, *Phase transformation in epitaxial GST thin films grown on Si(111) by pulsed laser deposition*, DPG Spring Meeting, Regensburg, Germany, Spring 2016.
- Hilmi, I., et al., poster, *Influence of the pulsed laser deposition parameters on the properties of epitaxial GST films on Si(111),* 19th International Summer School on Vacuum, Electron, and Ion Technologies (VEIT), Sozopol, Bulgaria, Autumn 2015.
- Hilmi, I., et al., poster presentation, *Epitaxial* $Ge_2Sb_2Te_5$ *thin films on Si(111) Substrate by pulsed laser deposition*, DPG Spring Meeting, Berlin, Germany, Spring 2015.

Acknowledgement

Firstly, I would like to greatly acknowledge the DAAD for the fellowship for my doctoral program in Germany. Secondly, my sincere gratitude is to Prof. Bernd Rauschenbach as my principal PhD advisor to assist me with DAAD scholarship application and has opened the opportunity for me to be a member of IOM Leipzig and further explore the world of solid states physics. The financial support given during the last year in IOM is also gratefully acknowledged; Thanks also to Prof. S. Mayr for all of the inputs and discussions especially during internal PhD student meetings. The recommendation for the prolongation of the scholarship is also greatly acknowledged; Dr. Jürgen Gerlach for all of his guidance during my thesis work and for introducing me to 'crystallography world', thanks for all your times to answer my (dumb) questions, to read all the publications, and to help with so many other things; Dr. Andriy Lotnyk for many fruitful discussions especially in TEM analysis and to show me how to write a better publication.

I would like to acknowledge all my former and current colleagues in IOM: Dr. E. Thelander who introduced me to the fancy PLD, Dr. X. Sun, Dr. U. Ross, Christoph G., Michael M., Uta K., Thomas L., Annemarie F., and to others I cannot mention one-by-one. Many thanks are to Philipp S., *er ist ein Freund von mir in Leipzig, der Hochdeutsch spricht*, for all the AFM measurements. Together with Andrey K. who have brought a fun atmosphere in the office. All other colleagues in IOM: Mr. Hirsch for SEM and EDX works, Toni Liebeskind who persistently helped me with so much substrate preparations, Mrs. A. Mill for her assistance and to show me how a delicate thin-lamellae preparation being performed. Dr. Zimmer, Dr. Bundesmann and Dr. Decker are also acknowledged for the introductions of Raman, Ellipsometry, and FTIR measurements, respectively. Much thanks also to my colleagues in Dept. of Physics: Abdurashid Mavlonov, Stefan Hohenberger, Alexander Shkurmanov, Vitaly Zviagin, etc.

I would like to thanks to all my DAAD friends especially to mas Dr. Eko Prasetyo and Dr. Fajar Hendarman for sharing the moments in start those first months in Germany. *Ich bedanke mich auch bei den Lehrern und Freunden bei InterDaf Universiät Leipzig*. Thanks to all my friends in Leipzig; mas Nandi, pak Hendra and '*geng ngopi Lukas'* especially to mas Gatot and Trismono who always brought 'ke-jawa-an' atmosphere. Thanks also to all the badminton friends.

I dedicate this work especially to my mother and (alm.) my father, they are my life inspirations. My big family, especially my brothers, who always supports me no matter what. Million thanks especially to my beloved wife, Zenith Purisha, who always encouraged me since very beginning, to explore the world together, for her tremendous patience and everything she has done to me. If not because of her this work would never be done.

Alhamdulillah
Isom Hilmi

Selbstständigkeitserklärung

Hiermit versichere ich, dass die vorliegende Arbeit ohne unzulässige Hilfe und ohne Benutzung anderer als der angegebenen Hilfsmittel angefertigt, und dass die aus fremden Quellen direkt oder indirekt übernommenen Gedanken in der Arbeit als solche kenntlich gemacht wurden.

Ich versichere, dass alle Personen, von denen ich bei der Auswahl und Auswertung des Materials sowie bei der Herstellung des Manuskripts Unterstützungsleistungen erhalten habe, in der Danksagung der vorliegenden Arbeit aufgeführt sind.

Ich versichere, dass außer den in der Danksagung genannten, weitere Personen bei der geistigen Herstellung der vorliegenden Arbeit nicht beteiligt waren, und insbesondere von mir oder in meinem Auftrag weder unmittelbar noch mittelbar geldwerte Leistungen für Arbeiten erhalten haben, die im Zusammnhang mit dem Inhalt der vorliegenden Dissertation stehen.

Außerdem versichere ich, keinen Promotionsberater in Anspruch genommen zu haben. Ich versichere weiterhin, dass die vorliegende Arbeit weder im Inland noch im Ausland in gleicher oder in ähnlicher Form einer anderen Prüfungsbehörde zum Zwecke einer Promotion oder eines anderen Prüfungsverfahrens vorgelegt und in ihrer Gesamtheit noch nicht veröffentlicht wurde.

Ich versichere außerdem, dass keine früheren erfolglosen Promotionsversuche stattgefunden haben.

Leipzig, 03 July 2018

Isom Hilmi